Synthesis and Characterization of Nanostructured Thin Films for Microsystems

Kaushik Das

Doctor of Philosophy

Department of Mechanical Engineering

McGill University

Montreal,Quebec

April, 2012

A thesis submitted to McGill University in partial fulfillment of the requirements of the degree of Doctor of Philosophy

DEDICATION

Dedicated to those who refuse to give up.

ACKNOWLEDGEMENTS

I would like to express my sincere gratitude to my supervisors, Professor Srikar Vengallatore and Professor Pascal Hubert for their support and guidance during the last four years of my doctoral studies.

I would like to thank Professor Richard Chromik (Department of Mining and Materials Engineering, McGill University) for allowing me to use the Hysitron Ubi nanoindenter. Thanks to Professor Thomas Szkopek (Department of Electrical and Computer Engineering, and Department of Physics, McGill University) for discussions on electron beam lithography.

I would also like to thank Professor Cheol Park (Department of Mechanical and Aerospace Engineering, University of Virginia, Charlottesville,VA, USA) for fabricating polymer nanocomposite films. Thanks to Professor Jean-Luc Meunier and Dr. Carole Emilie Baddour (Department of Chemical Engineering, McGill University) for preparing carbon nanotube felt composites.

I would also like to acknowledge Dr. Matthieu Nannini, Mr. Jun Li, and Mr. Donald Walter Berry of McGill Nanotools Microfab for their technical support, training and consultation on matters related to micro- and nanofabrication. Thanks to Dr. David Liu of Facility of Electron Microscopy Research for his assistance in transmission electron microscopy of thin films and nanowires.

I would like to specially thank my colleagues, Dr. Guruprasad Sosale, Mrs. Rosemary Le Faive, Dr. Behnam Ashrafi, Dr. Meysam Rahmat and Dr. Dorothée Almecija for

their collaboration on various projects. In addition thanks to all past and present members of FDA015 for making my life as a graduate student memorable.

Last but not the least, I would like to thank my family, and especially my mother for the continuous encouragement and support through all my endeavours.

ABSTRACT

Integration of nanomaterials (in the form of quantum dots, nanotubes, nanowires, nanocrystalline thin films, and nanocomposite films) with micromachined devices has the potential to enable the development of microelectromechanical systems (MEMS) with enhanced functionality and improved performance. However, many difficult scientific and engineering challenges must be solved before this potential is fully realized in practice. Addressing some of these challenges is the overarching goal of this thesis.

The first major challenge is to develop versatile methods for synthesizing nanomaterials and integrating them with micromachined structures and devices. A careful survey of the literature revealed a critical lack of techniques for integrating nanomaterials directly on fragile micromachined structures. This gap was filled by developing an approach that combines spray-coating of electron beam resist, direct-write electron beam lithography, physical vapour deposition of thin films, and lift-off processes. Polymeric and metallic structures in the form of arrays of holes, arrays of lines, and concentric circles were patterned directly on various micromachined structures including commercial metal-coated silicon microcantilevers used for atomic force microscopy, and commercial plate-mode SiC/AlN microresonators used for sensing. The critical lateral dimensions of the nanostructured materials ranged from 135 nm to 500 nm.

Once the practical difficulties of material synthesis and integration have been addressed, it is necessary to confront the challenges of predicting the behaviour, performance, and reliability of the integrated system. As a step towards that goal, this thesis established process-structure-property relationships for three different nanomaterials. The first study focused on the elastic properties of polymeric films reinforced with carbon nanotubes. Theoretical predictions, based on classical micromechanics, led to expectations of enormous enhancement of the elastic modulus, but these expectations have never been realized in practice. To the contrary, measurements show relatively little improvement after reinforcement. This paradox was explored by studying the properties of polyimide (PI) nanocomposite films reinforced with single-walled carbon nanotubes (SWNT), both computationally (via Eshelby-Mori-Tanaka micromechanics) and experimentally (through nanoindenter-based bending tests of freestanding nanocomposite films). For dilute composites, the elastic modulus increased with increasing nanotube loading from 2.5 GPa for the neat polymer to 3.5 GPa for a nanocomposite containing 0.5 volume% of SWNT. However, with further increase in the nanotube content, the elastic modulus remained essentially constant even for high loadings of 10 volume% of SWNT. Using results from microstructural examination, a link was found between the elastic properties of the nanocomposite and the dispersion, alignment and bundle size of the single-walled carbon nanotubes. The second study focused on energy dissipation by internal friction in nanofabricated structures. Establishing process-structure-dissipation relationships is crucial for the integration of nanomaterials with microresonators used for sensing, signal processing, and vibration energy harvesting. A novel method was developed for measuring

internal friction using a silicon microcantilever platform that is calibrated against thermoelastic damping. The use of this method was demonstrated by obtaining the first calibrated measurements of internal friction in aluminium nanowires with thickness ranging from 50 nm to 100 nm and widths ranging from 110 nm to 396 nm. At room temperature, the internal friction in these nanowires ranged from 0.026 to 0.035 for frequencies between 6.5 kHz and 21 kHz. Combining these measurements with microstructural examination of the grain size of the nanowires provided useful insights into the effects of patterning on dissipation.

The third study explored the relationships between processing parameters and elastic properties for a novel nanocomposite architecture which consists of an interconnected carbon nanotube network that is conformally coated with a thin layer of titanium nitride. The effective modulus of the nanotube network, measured by nanoindentation, was about 4 MPa. This value increased to around 2.5 GPa after coating the network with titanium nitride for 60 minutes. The implications of these results for the integration of these nanocomposites with MEMS switches are discussed.

Taken together, the contributions of this thesis - processes for patterning and integration, techniques for measuring material properties, and results for process-structure-property relationships - establish a foundation for the rational integration of nanomaterials with MEMS.

SOMMAIRE

L'intégration des nanomatériaux (dans le forme de points quantum, nanotubes, nanofils, minces films nanocristallins et films nanocomposites) avec des dispositifs micro-fabriqués a le potentiel de permettre le développement de systèmes microélectromécaniques (SMEM) ayant des fonctionnalités et performances accrues. Toutefois, plusieurs défis scientifiques et d'ingénierie doivent être surmontés avant que ce potentiel puisse être pleinement exploité en pratique. Cette thèse a comme objectif de résoudre certains de ces défis.

Le premier défi majeur est de développer des méthodes versatiles pour synthétiser des nanomatériaux et les intégrer aux dispositifs et structures micro-fabriquées. Une revue attentive de la littérature a révélé un manque critique de techniques pour intégrer les nanomatériaux directement aux structures micro-fabriquées fragiles. Ce manque a été comblé en développant une approche qui combine le revêtement par atomisation de résine, la lithographie à écriture-directe par faisceau d'électrons, le dépôt de films minces (pulvérisation et évaporation) et des procédés de soulèvement. Des structures polymériques et métalliques de différentes formes (trous, lignes et cercles concentriques) ont été fabriquées directement sur plusieurs structures micro-fabriquées incluant des micro-poutres de silicium commercialement disponibles et utilisées pour la microscopie à force atomique ainsi que des micro-résonateurs commerciaux de type "plate-mode SiC/AlN" utilisés à des fins de détection. Les dimensions critiques latérales des matériaux nanostructurés varient de 135 nm à 500 nm.

Une fois que les difficultés pratiques de synthèse et d'intégration des matériaux ont été maîtrisées, il a été nécessaire de comprendre et prédire le comportement, la performance et la fiabilité du système intégré. Cette thèse a établi des relations fabrication-structure-propriétés pour trois différents nanomatériaux. La première étude s'est concentrée sur les propriétés élastiques de films polymériques renforcés de nanotubes de carbone. Les prédictions théoriques, basées sur la micromécanique classique, ont conduit à des prévisions d'améliorations important du module élastique. Cependant ces attentes n'ont jamais été réalisées en pratique. Au contraire, les mesures expérimentales ont démontré relativement peu d'amélioration. Ce paradoxe a été exploré en étudiant les propriétés de films nanocomposites de polyimide (PI) et renforcés par des nanotubes de carbone à simple paroi (SWNT) par une étude numérique (via la micromécanique Eshelby-Mori-Tanaka) et expérimentale (par des tests de flexion de films nanocomposites non-contraints basés sur la nanoindentation). Pour les composites dilués, le module élastique a augmenté avec la teneur de nanotubes de 2.5 GPa pour le polymère non-modifié à 3.5 GPa pour le nanocomposite avec 0.5% par volume de nanotubes. Cette augmentation a cependant atteint un plateau pour de pourcentage volumique de nanotubes supérieurs à 10%. En utilisant des résultats d'inspections microstructurales, un lien a été établi entre les propriétés élastiques du nanocomposite et la dispersion, l'alignement et la taille des agglomérats de nanotubes de carbone.

La seconde étude s'est concentrée sur la dissipation d'énergie par friction interne dans les structures nano-fabriquées. L'établissement de relations fabrication-structure-dissipation est cruciale à l'intégration des nanomatériaux aux microrésonateurs utilisés

pour la détection, le traitement de signaux et la récolte de l'énergie des vibrations. Une méthode originale a été développée pour mesurer la friction interne en utilisant une plateforme pour des micro-poutres de silicium qui est calibrée en fonction de l'amortissement thermoélastique. L'utilisation de cette méthode a été démontrée en obtenant les premières mesures calibrées de friction interne dans des nanofils d'aluminium ayant des épaisseurs de 50 à 100 nm et des largeurs de 110 nm à 396 nm. À température ambiante, la friction interne de ces nanofils a varié de 0.026 à 0.035 pour des fréquences entre 6.5 kHz et 21 kHz. La combinaison de ces mesures avec une inspection microstructurale de la taille des grains des nanofils a fourni des indices des effets produits par la forme des motifs sur la dissipation.

La troisième étude a exploré les relations entre les paramètres de fabrication et les propriétés élastiques pour une architecture nanocomposite originale consistant d'un réseau de nanotubes de carbone interconnecté recouvert d'une mince couche de nitrure de titane. Un module élastique effectif du réseau de nanotubes de 4 MPa a été mesuré par nanoindentation. Cette valeur a augmentée jusqu'à approximativement 2.5 GPa après le revêtement du réseau par du nitrure de titane pendant 60 minutes. Les implications de ces résultats pour l'intégration de ces nanocomposites avec des commutateurs SMEM sont discutés.

Dans leur ensemble, les contributions de cette thèse - les procédés de fabrication de motifs et d'intégration, les techniques pour mesurer les propriétés des matériaux, et les résultats pour les relations fabrication-structure-propriétés - établissent une fondation pour l'intégration rationnelle des nanomatériaux avec les SMEM.

TABLE OF CONTENTS

KEY TO ABBREVIATIONS

AACVD: aerosol-assisted chemical vapour deposition xii

AFM: atomic force microscope xii

CNT: carbon nanotube xii

CVD: chemical vapour deposition xii

DRIE: deep reactive ion etching xii

EBID: electron beam induced deposition xii

EBL: electron beam lithography xii

FIBCVD: focused ion beam chemical vapour deposition xii

HiPCO-SWNT: single-walled carbon nanotubes produced by high pressure carbon monoxide decomposition process xii

HVP: high vapour pressure xii

IPA: isopropyl alcohol xii

LA-SWNT: single-walled carbon nanotubes produced by laser ablation process xii

LDV: laser Doppler vibrometer xii

LVP: low vapour pressure xii

MEK: methy elthyl ketone xii

MEMS: microelectromechanical systems xii

MIBK: methyl isobutyl ketone xii

MWNT: multi-walled carbon nanotube xii

LIST OF TABLES

LIST OF FIGURES

Figure page

CHAPTER 1
Introduction

Microsystems are miniaturized systems that are manufactured using components that have critical dimensions ranging from tens of nanometers to several micrometers. These systems are characterized by their small size (system volume of about one cubic centimeter), multiple functionalities, high level of integration, and operation in multiple energy domains. In the early stages of the development of microsystems technologies, the focus was dominantly on microelectromechanical systems (MEMS). For this reason, the acronym MEMS is commonly used to refer to all classes of microsystems even if their operation involves thermal, fluidic, optical, magnetic, chemical and biochemical domains. Thus, one can find references to bio-MEMS, power-MEMS, radio-frequency MEMS (or, RF-MEMS), and micro-opto-electromechanical systems (MOEMS) in the literature. In this thesis, MEMS, microsystems, microdevices, and micromachines are used as synonyms.

Examples of commercial MEMS products include gyroscopes, ink-jet nozzles, read/write head positioners in hard drives, digital light projectors (DLPs), microphones, portable spectrometers, gas chromatographs, silicon crystal timers and filters, microfluidics-based lab-on-a-chip applications for blood and body fluid analysis, chemical and biochemical sensors, and portable power sources like microbatteries [1].

Over the past decade, microsystems have become ubiquitous in our everyday lives. Micromachined accelerometers, pressure sensors and gyroscopes are used in

cars and aircrafts, thereby making our lives safer and transport simpler. These devices are also used in smart-phones, console-based game controllers, and hand-held computers to add new dimensions to electronics-based entertainment. Miniaturized sensors in digital cameras and micromirror digital projection systems have enhanced our experience of capturing and viewing digital images and movies. Portable spectrometers and gas chromatographs are increasingly being used by security agencies to detect explosive chemicals at public places. Miniaturized biosensors have found applications in the field of health-monitoring, for example allowing diabetic patients to monitor their blood-glucose level without a visit to the hospital.

The microsystems industry has seen a steady growth of 10–15% per annum over the last five years and was valued at $ 9 billion in 2010–2011. In addition to the sustained demand from automobile, aerospace and healthcare industries, a strong demand from the consumer electronics sector is expected to generate new MEMS products in the coming years. The market for microsystems is well established, and many more devices are making the transition from research laboratories to commercial manufacturing facilities. Among these devices are MEMS-based energy harvesters, microspeakers, microdisplays, microbolometers, optical switches, digital compasses, microfluidic devices for biomedical diagnosis, and drug delivery systems [2].

As these technologies evolve and mature, there is a growing need for developing systematic and rational approaches to improve performance, add new functionalities, and enhance reliability. One promising approach for achieving these goals is

by developing advanced materials and processes for microsystems. The first generation of MEMS used materials and processes which were inherited from the semiconductor microelectronics industry. This choice enabled MEMS engineers to leverage the massively-parallel batch-microfabrication methods developed for microelectronics. Moreover, this approach was advantageous for microelectromechanical systems that required a high level of integration of mechanical components with CMOS electronics. Since then, however, the field of microsystems has expanded to include many more energy domains, a large design space for shapes and structures, and a diverse set of applications. Therefore, a need has risen to move away from the traditional set of materials used in the semiconductor industry, and to develop a large portfolio of materials and processes for microsystems. Recent developments of materials processing techniques for silicon carbide thin films [3], silicon nitride thin films [4], and ultrananocrystalline diamond thin films [5] bear testimony to these efforts in the MEMS industry. Advanced materials currently used in MEMS include lead zirconate titanate (PZT), single crystalline lead magnesium niobate - lead titanate (PMN-PT), gallium nitride (GaN), cadmium sulphide (CdS), zinc sulphide (ZnS), aluminium nitride (AlN), gallium arsenide (GaAs), aluminium gallium arsenide (AlGaAs) thin films, and zinc oxide (ZnO) for piezoelectric MEMS actuators; multilayered TbFe/FeCo films, nanocrystalline TbDyFe films, TbFe films, crystalline $Fe_{50}Co_{50}$ thin films, and amorphous $(Fe_{90}Co_{10})_{78}Si_{12}B_6$ thin films for MEMS devices based on the giant magnetostrictive effect; FeCoBi thin films for MEMS devices based on giant magnetoimpedance; and NiTi and NiTiPd thin films for MEMS actuators based on shape memory effect [6]. In addition, a wide variety of advanced

functional polymers such as polyimide, polyaniline, polypyrrole, polythiophene, and polysiloxane are also being used in various MEMS applications [6]. In this context, there is one class of materials -namely, nanomaterials - that has received relatively little attention for microsystems applications.

1.1 Nanomaterials for microsystems

Nanostructured materials (also known as nanomaterials) are generally defined as materials that contain structural or microstructural features with dimensions less than 100 nm. Nanomaterials can be classified as zero-dimensional (for example, quantum-dots, and nanoparticles), one-dimensional (for example, nanowires, nanotubes, and nanofibers), two-dimensional (for example, ultra-thin films, and membranes) and three-dimensional (for example, nanocrystalline metals and ceramics). Many nanomaterials possess unique physical (mechanical, thermal, electrical, optical and magnetic) and chemical properties that are not observed in their bulk counterparts [7]. Some of these size-dependent changes are beneficial and can be harnessed to improve the performance and functionality of microsystems. In fact, the advantages of integrating nanomaterials with microsystems have been recognized for more than a decade [7]. In addition, there is a natural fit between nanomaterials and microsystems in the sense that the amount of nanomaterial required per device is small. Therefore, the lack of availability of high-quality nanomaterials in large quantities is not a barrier for commercial applications. For example, a single carbon nanotube can make a significant difference to the performance of silicon microcantilevers used in scanning probe microscopy. However, such examples of integration of nanomaterials are currently limited to a relatively small set of studies.

1.2 Objectives and organization of the thesis

The integration of nanomaterials (in the form of quantum-dots, nanotubes, nanowires, nanocrystalline thin films, and nanocomposite films) with micromachined structures and devices has the potential to enable the development of microsystems with enhanced functionality and improved performance. However, many difficult scientific and engineering challenges must be solved before this potential can be realized in practice. The overarching goal of this thesis is to make a useful contribution to this field by identifying and addressing some of these challenges.

The first major challenge is to synthesize nanomaterials and to integrate them with micromachined structures and devices. The small size and geometric complexity of the structural components, and the high level of integration, make it necessary to develop a large set of microfabrication and nanofabrication techniques to enable synthesis and integration. As a first step towards addressing this challenge, chapter 2 provides a critical survey of the literature and describes the different methods which have been developed for integrating nanomaterials with microsystems. The factors for selecting different methods, and the relative advantages and disadvantages of each method, are discussed. This exercise led to the identification of some critical gaps in existing techniques. One such gap is the lack of effective methods for patterning nanostructured materials directly on fragile micromachined structures. Chapter 3 fills this gap by developing an approach that combines spray-coating of electron beam resist, electron beam lithography, physical vapour deposition of thin films, and lift-off processes for patterning nanostructures on micromachined structures and devices.

Once the practical difficulties of material synthesis and integration have been solved, it is necessary to confront the challenge of predicting the behaviour, performance and reliability of the integrated system. Despite considerable progress over the past decade, many important properties of nanomaterials are not well known. Furthermore, many of these properties, and the structure of the nanomaterials, can be strong functions of the methods used for synthesis and integration. Therefore, it is necessary to develop robust process-structure-property relationships to guide the use of nanomaterials for microsystem applications. This is a large and challenging problem that will take decades of systematic effort because there are a large number of properties, and an even larger set of nanomaterials, to explore. This thesis takes a first step towards this goal by studying three different combinations of materials and process-structure-property relationships.

The first study explores a case where theoretical predictions, based on classical micromechanics, led to expectations of enormous improvements in the elastic constants of polymer thin films reinforced with single-walled carbon nanotubes (SWNT), but these expectations have never been realized in practice. To the contrary, measurements typically show relatively little improvement after reinforcement. This paradox is explored in chapter 4 by studying the elastic properties of polyimide (PI) nanocomposite films reinforced with SWNT. These nanocomposite films were synthesized by in-situ polymerization with simultaneous ultrasonic mixing and mechanical stirring, followed by solution-casting. The volume fraction of carbon nanotubes in the polymer matrix was varied from 0–10%. The elastic moduli of the nanocomposite films were characterized using a nanoindenter-based bending test, and were

compared with calculations based on Eshelby-Mori-Tanaka micromechanics. Microstructural examination provided some insights into the discrepancy between the theoretical predictions and experimental results.

The second study explores the case where a nanomaterial can add useful functionality to a microdevice, but also degrade its performance. This situation is commonly encountered in the design of micromechanical resonators for applications in sensing, signal processing, and energy harvesting. These miniaturized resonators require low damping (or, equivalently, a high quality factor, Q) to improve sensitivity and frequency selectivity. For this reason, ceramic materials (such as single-crystal silicon and silicon nitride) are used for making the resonators. Subsequently, these ceramic structures are coated with nanocrystalline metals in the form of thin films or patterned structures to enhance optical reflectivity, electrical conductivity, and surface chemistry. Unfortunately, these new functionalities come at the cost of a disproportionately large increase in damping, which degrades the performance of the microresonators. Recent measurements provide an indication of the magnitude of this problem [8]. At some frequencies, the damping in a silicon microcantilever can increase by one order of magnitude when coated with a thin film of aluminium, even though the aluminium is a hundred times thinner than the silicon.

At present, very little is known about mechanisms of damping in nanomaterials. Systematic measurements of the effects of frequency, size, and microstructure on dissipation are required to formulate process-structure-damping relationships. As the first step in that direction, chapter 5 introduces a technique for measuring damping of nanomaterials. The technique to measure damping is based on a microcantilever

platform that is calibrated against the limits of thermoelastic damping. Chapter 5 describes the design, development, and validation of this platform, and provides the first measurements of internal friction in aluminium nanowires. Finally, internal friction in the aluminium nanowires is compared with that in continuous thin films of aluminium to understand the effects of patterning on dissipation.

The third study explores the case where nanomaterials open up new opportunities for applications by virtue of their novel architectures and properties. However, it is necessary to explore these structures by developing process-structure-property relationships so that designers can appreciate the potential of these materials. This case is explored in chapter 6 by studying the mechanical properties of multi-walled carbon nanotubes grown on stainless steel by a chemical vapour deposition process. The carbon nanotube network is then coated by titanium nitride thin film using cathodic arc deposition. Thus, the final structure is a porous network of multi-walled carbon nanotubes coated with titanium nitride. Standard nanoindentation tests were performed to explore the relationships between the process parameters (bias voltage and deposition time), structure (thickness of the titanium nitride coating), and mechanical properties (contact stiffness and effective modulus). These results are used to evaluate the utility of these nanocomposites for applications in MEMS switches.

Table 1–1 presents a summary of the organization of the thesis.

1.3 Contributions of the thesis

This thesis develops new methods for nanofabrication and integration; new techniques for measuring the mechanical properties of nanomaterials; and new knowledge in the form of process-structure-property relationships that can guide the use of new

Table 1–1: Organisation of the thesis

Nanomaterials	**SWNT-reinforced polymer films** *Ch 4*	**Nanocrystalline aluminium films and nanowires** *Ch 5*	**CNT/TiN nanocomposite** *Ch 6*
Synthesis/Processing	In-situ polymerization under ultrasonication, mechanical stirring, followed by solution-casting of thin film, and drying in a dry-air flowing chamber.	Spray-coating, electron beam lithography, and electron beam evaporation	Thermal chemical vapour deposition to grow carbon nanotube 'felt' on stainless steel, followed by cathodic arc deposition of titanium nitride on the carbon nanotube network.
Characterization	Nanoindenter-based bending test	Microcantilever platform for dynamic characterization	Conventional nanoindentation (Oliver-Pharr method)
Property	Elastic modulus	Internal friction	Effective elastic modulus, contact stiffness
Potential applications	MEMS actuators and resonators	Optical coatings	RF-MEMS switches

classes of nanomaterials for microsystem applications. The original contributions of this thesis are listed below.

- A nanofabrication procedure, involving spray-coating of electron beam resist, electron beam lithography and subsequent metal deposition and lift-off, was developed to pattern polymeric, nanocomposite and metallic nanostructures on fragile micromachined devices. The versatility of this approach was illustrated by patterning polymeric and metallic structures in the form of arrays of holes, concentric circles, and arrays of lines, with critical dimensions ranging from 135 nm to 500 nm, directly on various micromachined structures including commercial metal-coated silicon microcantilevers used for atomic force microscopy, and commercial plate-mode SiC/AlN microresonators used for sensing.
- Process-structure-property relationships were established for polyimide (PI)-matrix nanocomposite films reinforced with single-walled carbon nanotubes (SWNT); the volume fraction of the nanotubes ranged from 0.05–10%. The effects of nanotube loading on the elastic properties of these nanocomposite films were measured using a nanoindenter-based bending test, and evaluated computationally using Eshelby-Mori-Tanaka micromechanics. In addition, the same comparison was made for specimens containing the same volume fraction (0.5 volume%) of SWNT produced by two different processes. Taken together, these studies provided useful insights into the effects of nanotube dispersion and alignment on the elastic properties of the nanocomposite.

- A method for measuring dissipation due to internal friction in nanostructured materials was developed and used to obtain the first measurements of internal friction at room temperature in aluminium nanowires. These results are the first step towards process-structure-dissipation relationships for patterned nanostructures.
- Process-structure-property relationships were established for a porous network consisting of multi-walled carbon nanotubes coated with thin films of titanium nitride. The effects of process parameters on mechanical properties were established using nanoindentation.

CHAPTER 2
Literature survey on processing and integration of nanostructured materials with MEMS

The integration of nanomaterials with microsystems is an active area of current research. There is a vast literature on this topic covering many different aspects of integration. The goals of this chapter are to review this literature by focusing on methods, procedures, and techniques for integration. This knowledge is evaluated and organized in an effort to identify the relative strengths and weakness of different approaches. This organization can also help to identify critical gaps in current techniques.

Several attempts have already been made to organize the literature on integrating materials with microsystems. The textbook by Senturia [9] identified the various issues that must be considered by process engineers. These issues span the spectrum from device geometry to packaging and die separation. In 2009, Alaca [10] reviewed the literature on integrating one-dimensional nanomaterials (nanowires, nanotubes) with microsystems. The work presented in this chapter builds upon these efforts. The next section lists the factors that must be considered while integrating nanomaterials with microsystems, Section 2.2 discusses the different techniques that are available for integration, and Section 2.3 presents a focused discussion of integrating nanocomposite materials with microsystems.

2.1 General considerations for integration

The successful integration of nanomaterials with microsystems requires a careful consideration of numerous factors. The first factor that must be considered is the type of nanomaterial. As noted earlier, nanomaterials can be characterized as zero-dimensional (quantum dots, nanoparticles), one-dimensional (nanowires, nanotubes), and two-dimensional (thin films and membranes). Further, the nanomaterial can exist as a single component (such as a single carbon nanotube) or be integrated as a nanocomposite or in arrays.

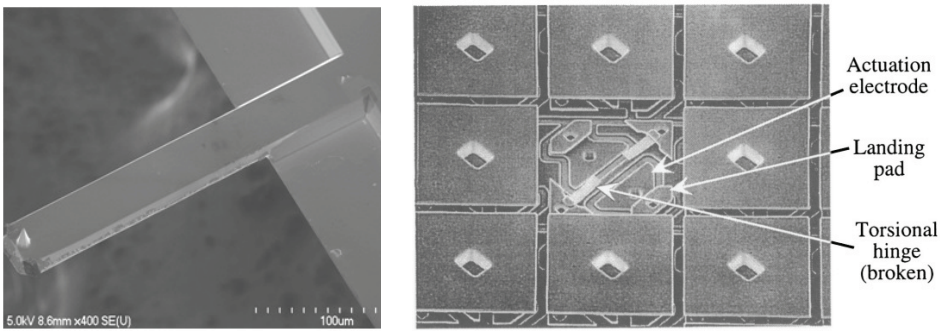

(a) (b)

Figure 2–1: Examples of microdevices: (a) A single-component microcantilever beam, (b) A two-level electrostatically actuated micro-mirror display [9].

The second factor is the detailed architecture and structural design of the microdevice or microsystem. The complexity of the microdevice can range from a simple mechanical component (such as a single microcantilever beam, as shown in figure 2–1(a)) to a large assembly of complicated structures (such as the two-level electrostatically actuated micro-mirror display developed by Texas Instruments, as shown in figure 2–1(b)). Some microsystems (such as micro fuel cells and micro

chemical reactors) do not contain any moving parts, while others are subjected to significant mechanical and thermal stresses during deployment and operation.

The third factor is the level of control required over the location, dispersion, and alignment of the nanomaterial. These details are a function of the specific application under consideration. For some applications, a random distribution of the nanomaterials on the surface of the microdevice may suffice, and bottom-up methods based on self-assembly of nanomaterials are ideal. However, other applications may require a high level of control over the placement, orientation and distribution of the nanomaterial. For such high-end applications, top-down serial processes like electron beam lithography play a crucial role. However, many of these techniques are constrained either by high cost or slow patterning speeds, especially for structures that have critical feature sizes less than 100 nm. Hybrid techniques that combine some features of both top-down and bottom-up methods are also being developed for applications which require an intermediate degree of control over placement, orientation and distribution of nanomaterials.

The fourth factor is chemical, mechanical, and thermal compatibility between the processes used for synthesizing and integrating the nanomaterial and those used for micromachining the other components of the microsystem. This is a challenging issue because the latter can involve dozens of microfabrication steps using several different tools and techniques. These various steps can affect each other leading to unintended and undesirable consequences. Therefore, the issue of compatibility is intimately related to the specific processing steps that are used, and to the manner in which these steps are sequenced. Further, considerations of compatibility also

influence whether the nanomaterial is integrated at the device-level or at the wafer-level.

Consider, for example, the case where a nanomaterial is integrated at the wafer scale early in the process sequence. The nanomaterial will then have to withstand the harsh chemical and thermal conditions that are usually encountered during the microfabrication of the microsystem. These conditions include exposure to corrosive chemicals, gases, and plasma, and to high temperatures that can lead to undesirable coarsening and grain growth in the nanomaterial. If the nanomaterial can indeed be shielded from these harsh environments, then this material can be first synthesized at the wafer level (using techniques such as nanoimprint lithography, dip-pen nanolithography and electron beam patterning), and the micromachined structures can then be created [11].

Alternately, the microdevice can be first processed, and the nanomaterial can be integrated at the device level. In this case, it is not necessary to protect the nanomaterial during the harsh steps of microfabrication. However, the microdevice itself can be mechanically fragile and must be protected from damage during integration. For example, spin coating of photoresist or electron beam resist can damage a micromachined beam or plate. Thus, the processes used for integrating the nanomaterial must be mechanically compatible with the microsystem.

2.2 Techniques for integrating nanomaterials with MEMS

The following sub-sections explore the different methods available for integrating nanomaterials in the form of nanoparticles, nanowires and nanotubes to microsystems. These methods can be categorized based on the manner in which the nanomaterial is synthesized and the approach used for localizing the nanomaterial on the microdevice. The first category consists of methods based on self-assembly. In this approach, the nanomaterial is usually synthesized separately, purified, and brought to the surface of the micromachined device. The subsequent location and alignment of the nanomaterial can be controlled using electric, magnetic, fluidic and chemical forces. The second category consists of methods based on controlled growth wherein the nanomaterial is synthesized directly at the desired location on the microdevice. The third category consists of methods based on nanomanipulation and nanolithography. The former refers to techniques for picking individual nanomaterials (such as a single nanowires or nanoparticle) and placing it at the desired site on the microdevice. The latter refers to the use of electron beams and ion beams for controlling the location, orientation and distribution of nanomaterials on the microdevice. Each of these categories is discussed in detail in the following sub-sections.

2.2.1 Integration by self-assembly

Self-assembly can be defined as spontaneous formation of patterns or structures due to physical and/or chemical interaction of nanomaterials, usually without any human intervention [12, 13]. Examples of self-assembly, especially biological self-assembly, are extremely common and are manifested in complex two-dimensional and three-dimensional structures we find in nature. Nanostructured materials can

be assembled on MEMS device components by applying an external electric or magnetic field, and by microfluidic assembly. Most of these methods of self-assembly require the nanostructured material to be fabricated separately, removed from their fabrication sites, dispersed in a fluid medium and aligned using physical or chemical interactions. Details of these methods are presented in the following sections.

Electrical field-assisted assembly

Nanomaterials in the form of nanoparticles, nanowires and nanotubes can be aligned in a fluidic medium by the application of an electric field. This electrokinetic phenomenon which leads to the motion of anisotropic dielectric nanomaterials under the action of an inhomogeneous electric field is known as dielectrophoresis. Alignment of nanomaterials using dielectrophoresis involves polarization of the nanomaterials. Polarization can be achieved by applying an AC field, with or without a DC bias. When the nanomaterial get polarized, it experiences a force (called the 'dielectrophoretic force') due to the interaction of the induced dipole moment in the nanostructure with the applied non-uniform electric field. This dielectrophoretic force depends on the geometry of the nanomaterial, on the dipole moment (which depends on the dielectric constants of both the nanomaterial and the fluidic medium in which it is dispersed), and on the magnitude of the applied electric field [14]. Alignment of nanomaterials by dielectrophoretic forces requires high electrical field strengths. Besides, higher dieletrophoretic force can be achieved by noting that dielectric force is directly proportional to the difference of the dielectric constants. High dielectric forces can be achieved by using a fluid medium like water (dielectric constant of water is $\sim$80), and ensuring that the gap between the electrodes is small. A

principle commonly used to attract nanomaterials towards electrodes (contact pads) is that of positive dielectrophoresis. Positive dielectrophoresis involves motion of a polarized nanomaterial towards regions of high electric field and happens only when the nanomaterial is more polarisable than the surrounding medium.

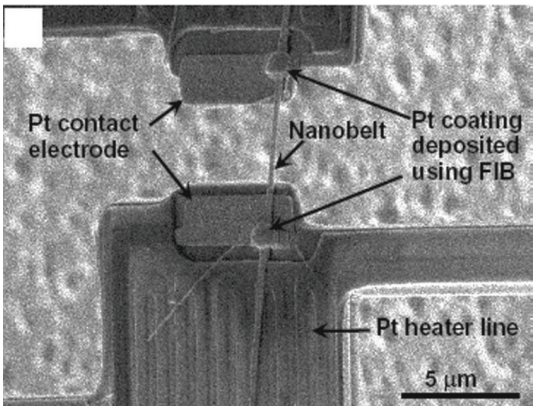

Figure 2–2: Example of electric-field assisted self-assembly: A tin dioxide nanobelt is integrated to a microhotplate platform using dieletrophoresis [15].

Yu *et al.* [15] have reported the integration of tin dioxide nanobelts to microfabricated membranes in a MEMS microheater device to detect a nerve agent stimulant. The nanobelts were assembled to bridge two platinum electrodes, using the principle of electrophoresis. This method involved spinning a solution containing the nanobelts on a wafer containing a large number of densely packed membrane structures. The nanobelts were often adsorbed between the two closely spaced Pt electrodes. In another method, the nanobelts were assembled on the platinum electrodes using the principle of positive dielectrophoresis. This method involved connecting two platinum electrodes in the microdevice to an AC voltage source and adjusting the voltage and frequency of the AC electric field when the solution containing the nanobelts was

dispersed on the wafer surface. The attractive or positive dielectrophoretic force was used to polarize the nanobelts, and align and trap a nanobelt onto the two platinum electrodes, as shown in figure 2–2.

In addition, the principle of electrophoresis has also been applied for aligning nanostructured materials to microdevices. Unlike dielectrophoresis, the net electric electric charge (and not the dipole moment) governs the motion of the nanostructure in a uniform or divergent electric electric field in electrophoresis. The nature of the solvent influences the surface-charge of the nanomaterials and hence plays a crucial role in electrophoresis.

Benkstein *et al.* [16] have integrated nanostructured polyaniline film with a MEMS microhotplate, using the principle of electrophoresis. First a polyaniline colloid was prepared , and this colloid was deposited electrophoretically on the microhotplates using a programmable power supply. To selectively deposit the nanostructured polyaniline film on the microhotplates, the bondings and the wirepads were electrically isolated by an insulating epoxy. Advantages of the electric field assisted assembly include the ability of using this technique both on wafer-scale as well as on fabricated fragile device components.

Magnetic field-assisted assembly

In a fashion similar to the use of electric fields, magnetic fields can also be applied to align nanowires and nanotubes on microdevice components. One advantage of magnetic field assisted lithography over its electrical counterpart is that no specific surface chemistry is necessary. Furthermore, the magnetic forces are independent of the fluidic medium used. However, in order to facilitate assembly by magnetic

forces, a part or whole of the nanowires must be ferromagnetic or must be partially coated with a ferromagnetic material. Moreover, the patterned electrodes on which the nanomaterials are assembled must also be ferromagnetic. Nickel is the most commonly used ferromagnetic material, however other materials like iron, cobalt and their alloys can also be used. When placed in an external magnetic field, these ferromagnetic nanomaterials orient themselves along the direction of the magnetic field, usually forming end-to-end networks and bundles [17,18]. Figure 2–3 shows an example of a nickel/bismuth/nickel nanowire aligned on pre-patterned nickel lines. Another important consideration of magnetic self-assembly is that the concentration of the nanostructures should be lower than a critical value beyond which van der Waal's interactions among the nanostructures become dominant over the magnetic effects.

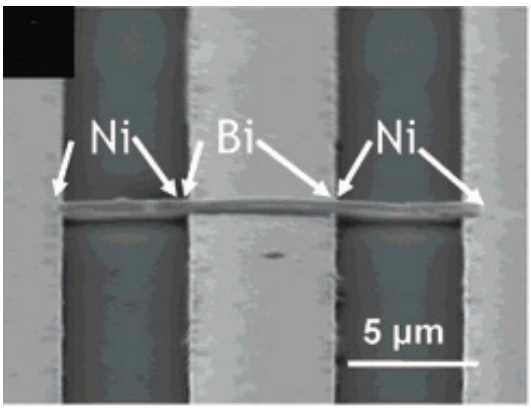

Figure 2–3: Example of magnetic field-assisted assembly: A single Ni/Bi/Ni nanowire is aligned on patterned nickel lines [17].

Microfluidic assembly and other methods

Microfluidic assembly is another wafer-level assembly method employed for aligning nanowires and nanotubes. This method is very similar to non-convetional lithography techniques like micromoulding in capillaries [19]. Microfluidic assembly involves feeding suspensions containing nanowires through microchannels. This leads to alignment of the nanowires along the flow direction or across the channel width, after the carrying fluid has evaporated. This method has been used to align indium phosphide, gallium phosphite and silicon nanowires along the flow direction in polydimethylsiloxane (PDMS) micromachannels, as shown in figure 2–4 [20].

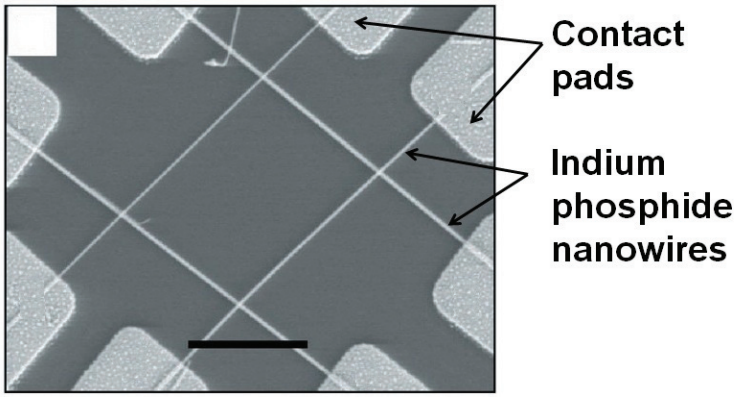

Figure 2–4: Example of microfluidic assembly: Indium phosphide nanowires obtained by a two-step microfluidic assembly process [20]. The scale bar corresponds to 500 nm.

Other methods of using self-assembly to integrate nanomaterials to microdevices can also involve Langmuir-Blodgett technique and selective functionalization. Langmuir-Blodgett technique uses compression of nanomaterials at the liquid-air interface forming an ordered array of nanomaterials, followed by transfer onto the solid

surface. Thus, Langmuir-Blodgett technique has the potential to be used as a wafer-level technique during fabrication of MEMS devices. Selective functionalization uses the knowledge of chemicals which bind specifically to other chemicals. Examples of such specific bonding is common among biomolecules like proteins, DNA and viruses. In this technique nanomaterials are functionalized by such biomolecules. An essential part of this technique is using photolithography or other high-resolution lithography techniques to pattern the wafer surface with the complementary chemical species. Once the functionalized nanomaterials are transferred to the patterned wafer surface, the nanomaterials self-assemble by binding with the complementary chemicals. Reference [10] presents a detailed review of the application of these methods to integration of nanomaterials to microelectronic devices.

In cases where no alignment is required, nanomaterials can be integrated by dispersing the nanomaterial in a volatile solvent and applying it to the microdevice by drop-casting or spin-casting. This leads to a random distribution of nanomaterial on the surface of the MEMS device. Zribi *et al.* have integrated carbon nanotube networks on a microfabricated silicon nitride diaphragm and demonstrated the use of the carbon nanotube film as a carbon dioxide gas sensor [21]. Solutions of well-dispersed single-walled carbon nanotube in a volatile non-aqueous solution was first prepared by ultrasonication. This was followed by drop-casting or spin-casting of the solutions onto the diaphragm. High volatility of the organic solvents led to convenient and fast nanotube deposition. A similar method was also used to deposit zinc oxide nanowires for use as an ethanol sensor [22].

2.2.2 Controlled growth

Controlled growth is one of the most popular methods of integrating nanowires to MEMS devices. By using this method, nanowires and nanotubes can be grown at a desired site of a microdevice component. For growing nanowires a vapour-liquid-solid (VLS) technique, based on a chemical vapour deposition (CVD) process, is utilized. This technique uses metal nanoparticles or nanodroplets as catalyst which absorbs the nanowire or nanotube material supplied in the gas phase forming a supersaturated alloy. The growth of nanowire or nanotube takes place by precipitation of the nanotube or single-crystal nanowire at the interface of the nanodroplet and the substrate. This technique has been used to grow single-crystal nanowires of silicon, germanium, gallium nitride and tin oxide [23]. With proper selection of substrate, the nanowires can be grown in a direction perpendicular to the substrate. Carbon nanotubes can also be grown in a directional fashion using thermal or plasma-assisted VLS techniques [24, 25].

Teh *et al.* have used a plasma-enhanced chemical vapour deposition (PECVD) method to integrate vertically aligned carbon nanotubes on under-etched ∼190 nm thick titanium micromechanical structures, an example of which is shown in figure 2–5 [26]. The PECVD process was carried out at 650 °C using nickel as the catalyst. The chemical vapour consisted of 25% acetylene in ammonia.

Most of the routes for integration of nanomaterials to MEMS devices require global exposure of the device to the processing conditions. This usually makes the process incompatible with traditional microfabrication process. Methods for selectively synthesizing silicon nanowires and carbon nanotubes on the MEMS device

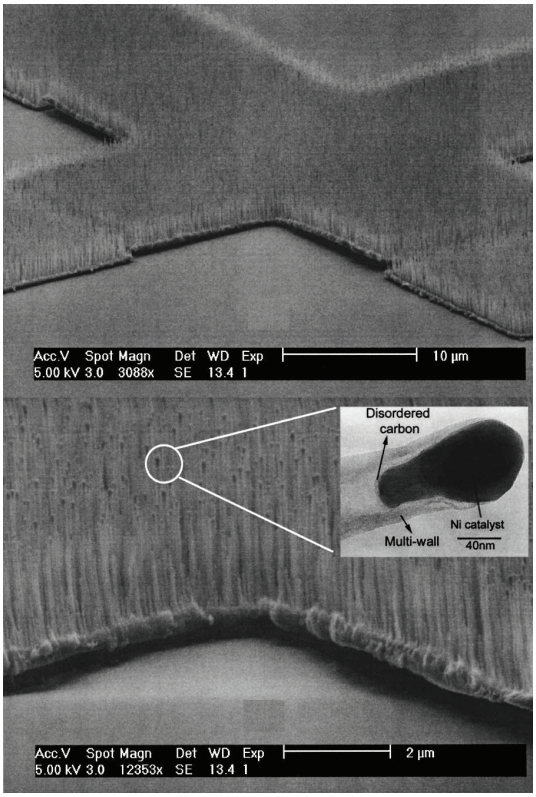

Figure 2–5: Integration of vertically aligned carbon nanotubes with a titanium micromechanical structure [26].

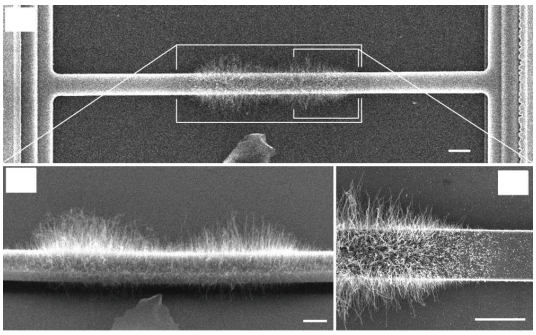

Figure 2–6: Example of integration of silicon nanowires to MEMS structures by selective and controlled growth. All scale bars represent 5 μm [27].

components such as on microbidges, cantilevers and tips of an AFM cantilever at room temperature have been developed [24,27,28]. These methods involve patterning of the tip of the cantilever with an ultra-thin film of catalyst for nanowire nucleation and growth. Local heating of parts of the MEMS device eliminates exposing the entire microdevice to the high temperatures of CNT growth. The microdevices are then exposed to the precursor gases, which react with the catalyst, leading to local and selective nucleation and growth of nanowires and carbon nanotubes. Figure 2–6 shows one example of such local integration of nanomaterials.

2.2.3 Nanomanipulation and nanolithography

The third category of techniques for integrating nanomaterials with MEMS structures are serial processes and comprise of techniques such as nano-manipulation techniques, electron beam lithography, electron beam deposition, focused ion beam milling and focused ion beam deposition. These techniques provide perfect control over the location, orientation and distribution of the nanomaterials at both wafer-level as well as on prefabricated, micromachined fragile structural components. However, being serial processes these techniques are extremely time consuming and have not been used for large-scale manufacturing of microdevices. Till date these techniques have been limited to low-volume and high-end applications as well as for proof-of-concept devices. The remainder of this section discusses the application of these techniques to integration of nanomaterials specifically to MEMS devices.

Nanomanipulation techniques

Nanomanipulation refers to techniques for picking and transferring single nanomaterial like nanowire, nanotube and nanoparticle from the surface they are grown

or deposited to the surface of a device. Common nanomaipulators are themselves MEMS devices and require high degree of precision in terms of their motion control. Examples of nanomanipulators are atomic force microscope cantilevers, optical and mechanical tweezers, as well as nanorobotic manipulation systems [10]. Most of the single or multiple probe nanomanipulators are operated inside an electron microscope and have been crucial components of experiments to investigate properties of nanomaterials. For example, a two-probe nanomanipulator was used to evaluate mechanical property of multi-walled carbon nanotubes [29].

In addition, nanomanipulators are routinely used for fabricating microdevices with integrated nanowires or nanotubes. For example, Meier *et al.* have integrated a single-crystal tin dioxide nanowire to a microfabricated microhotplate and used the nanowire-integrated microdevice as a gas sensor [30]. The nanowires were synthesized separately. Integration with the microhotplate involved electrostatically picking up individual nanowires using a dielectric microfiber, followed by transferring the nanowire to a microhotplate.

One advantage of using a nanomanipulator is that it has the ability to integrate nanomaterials to non-planar surfaces. The work by Carlson *et al.* provides an example of such integration [31]. In this work, a microgripper is used to integrate a carbon nanofibre to the tip of an atomic force microscope cantilever. Figure 2–7 illustrates the different steps of the integration.

Electron beam lithography

Electron beam lithography is one of the oldest and most characterized techniques employed in nanofabrication. This nanofabrication technique has been used

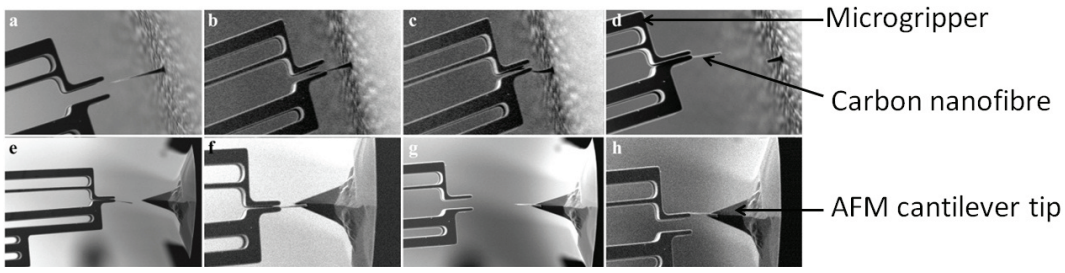

Figure 2–7: Integration of a carbon nanofibre with an atomic force microscope cantilever tip [31].

in combination with lift-off technique to define metallic nanostructures. The metallic nanostructures can be used as masks, and nanomechanical structures can be obtained by further etching steps. These nanostructures form essential components of nanoelectromechanical systems [10, 32]. Examples of such structures include nanobridges of materials such as single-crystal silicon and silicon carbide [32–34]. Nanostructures like nanodots or nanowires fabricated by electron beam lithography can be also used as a template or catalyst to grow nanostructures by a CVD process. For example, Ye *et al.* have integrated carbon nanotube on the tip of an AFM cantilever by first defining nanosized catalyst spots on the entire wafer by electron beam lithography and lift-off, followed by protecting the catalyst spot and micromachining the cantilever structure, and finally growing a carbon nanotube on each cantilever by a controlled growth CVD approach [11].

One major disadvantage of electron beam lithography is lack of an approach to define metallic nanostructures on micromachined structures. Donthu *et al.* have developed a method combining electron beam lithography and sol-gel synthesis method to obtain polycrystalline ceramic nanostructures on free-standing membranes [35–37]. Figure 2–8 shows some examples of integration of nanomaterial by electron beam

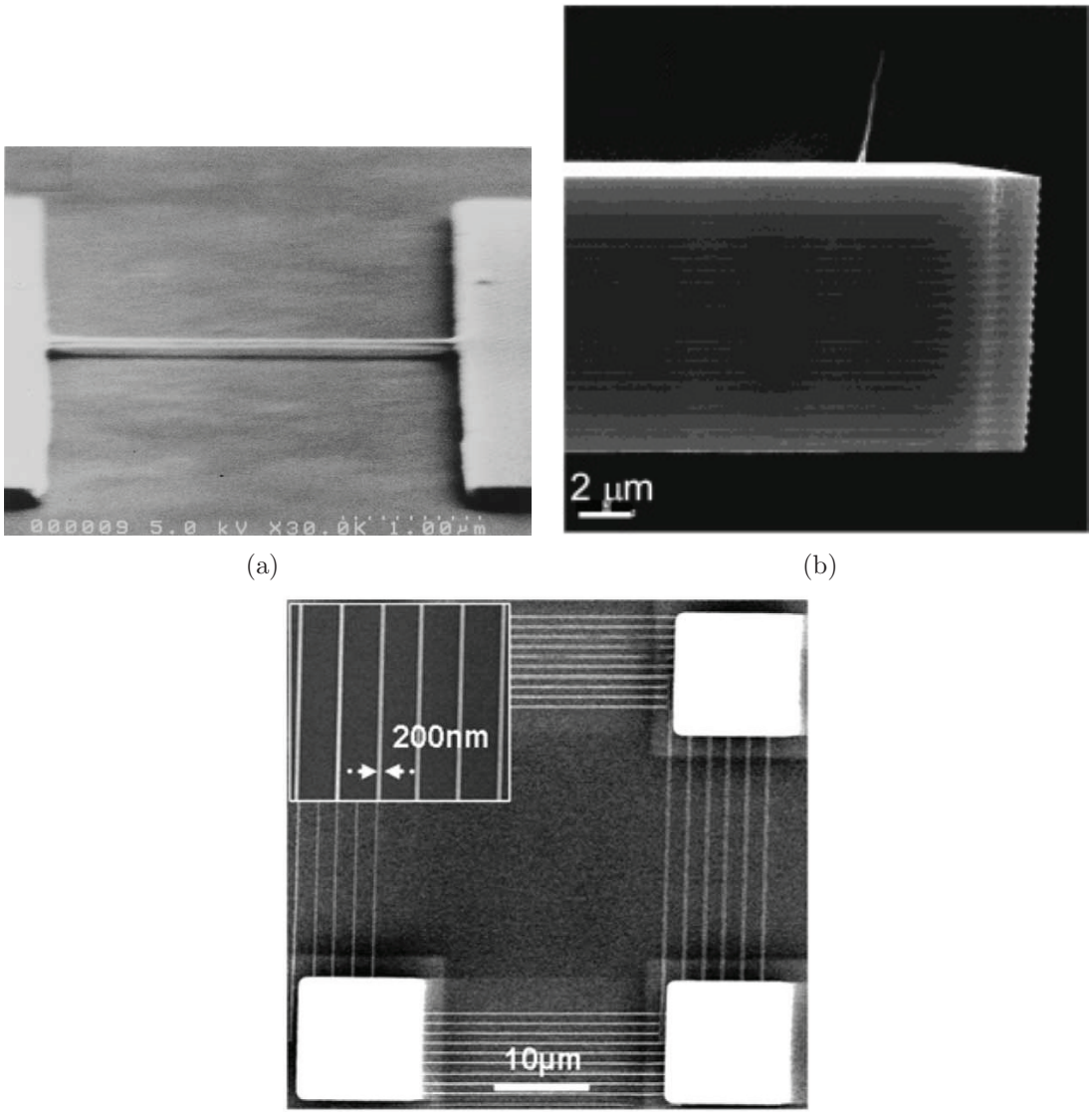

(a) (b)

(c)

Figure 2–8: Examples of nanomaterial integration by electron beam lithography: (a) A silicon nanowire bridge [33], (b) a carbon nanofibre integrated to a silicon microcantilever [11], and (c) zinc oxide nanowires integrated on a MEMS microhotplate [35].

lithography. However, this method, known as soft-EBL is not universally applicable. First, this process is limited only to a handful of ceramic oxides, which are available through a route of sol-gel processing. Second, and most importantly, since it involves spin-coating steps, it cannot be used on devices with non-planar topography. *These issues are addressed in chapter 3 by developing a versatile method for integrating nanomaterials directly on micromachined structures by electron beam lithography.*

Electron and focused ion beam deposition techniques

Electron beam induced deposition is well-suited to grow nanowires as well as make three dimensional structures on both planar and non-planar surfaces. One common application of this technique is to promote adhesion between nanomaterials such as nanowires and nanotubes to a microdevice surface. For example, most MEMS micro/nano-tensile testing stages require electron beam induced deposition on the region outside the gauge length, in order to attach the nanomaterial firmly to the grips and prevent any slipping [38]. Figure 2–9 shows an example of electron beam deposited platinum for improved adhesion of nanomaterial. In addition, electron beam induced deposition has been used to fabricate metallic three dimensional nanostructures, for example atomic force microscope tips [39], four-point probes [40], and octahedral frames [41].

Other techniques like focused ion beam CVD (FIBCVD) with better deposition rates than electron beam induced deposition are used to deposit three dimensional nanostructures [42]. The low penetration depth of the ions used in FIBCVD makes it easier to fabricate complicated three dimensional structures like coils and nanomanipulators, as shown in figure 2–10.

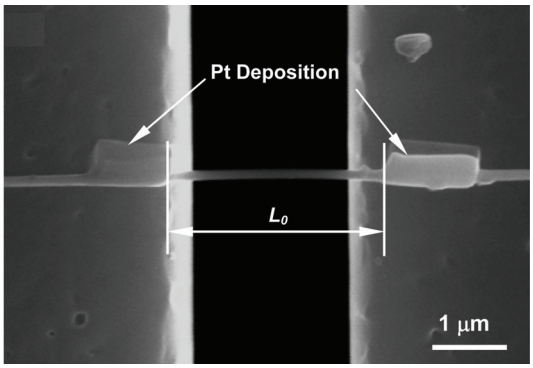

Figure 2–9: A scanning electron microscope image showing electron beam deposited platinum for improved adhesion of zinc oxide nanowire to a tensile testing stage [38].

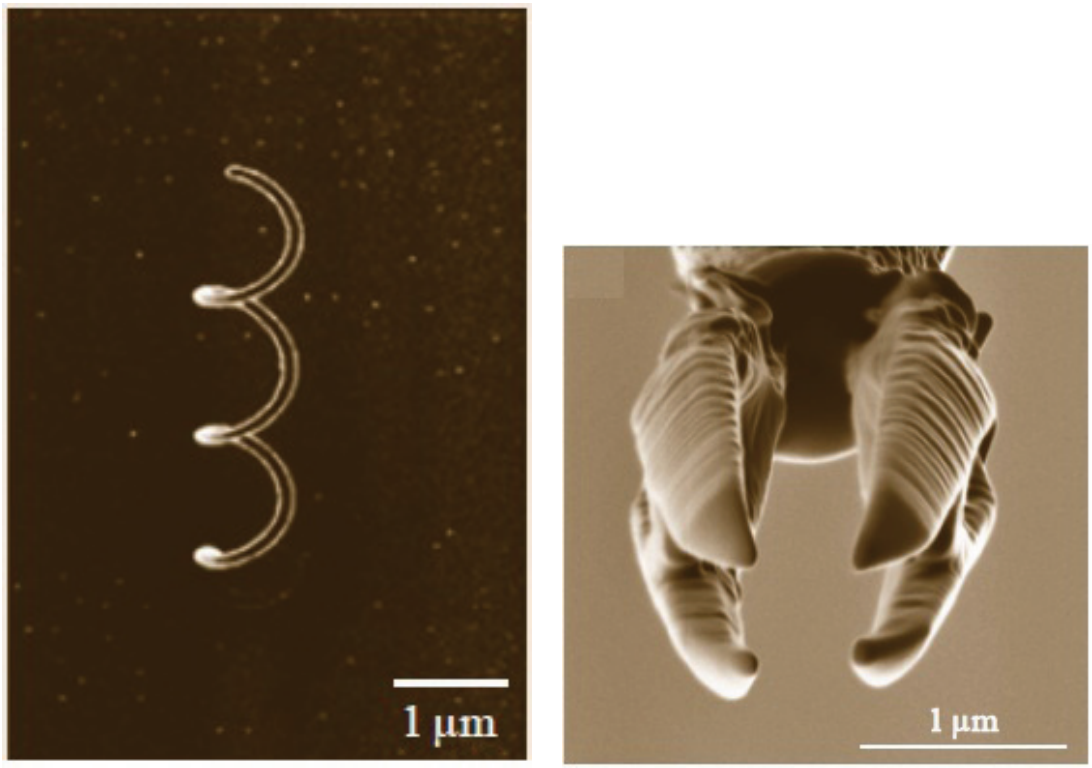

(a) (b)

Figure 2–10: Examples of nanostructures by FIBCVD technique: (a) Microcoil with coil diameter of 0.6 μm, coil pitch of 0.7 μm, and linewidth of 0.08 μm; (b) Top view of a three-dimensional eletrostatic nanomanipulator [42].

Another focused ion beam based technique, namely focused ion beam milling provides a direct way to machine microstructures to form nanostructures and has been used to form monolithic nanostructures not only for MEMS devices [43], but also for fabricating metallic, ceramic and glass samples for nanocompression tests, for transmission electron microscopy, and for inspection of failure of MEMS devices [44–46].

2.3 Integration of nanocomposites with MEMS

This section provides a focused review of recent developments in nanocomposite-based MEMS, emphasizing particularly on materials, fabrication techniques, and applications. The different techniques applied currently to synthesize nanocomposite thin films, involving a wide array of metallic, ceramic and polymer matrices, are described. Finally, several representative examples of integration of nanocomposite components in MEMS devices are discussed.

2.3.1 Physical mixing

The initial research articles on application of nanocomposites in MEMS dealt with developing resists for electron beam lithography (EBL). These electron beam resists with embedded nanoparticles of fullerene and surface-modified silica not only exhibited higher resolution compared to the pristine resist, but also higher etch resistance [47,48]. In both cases, the nanoparticles were incorporated into the polymer resist matrix by a physical mixing approach, i.e. the synthesis of nanoparticles was carried out by wet chemical routes and they were then dispersed into a polymer solution, which was spin-coated to form a film. However, this approach has inherent problems of agglomeration of nanomaterials at high concentrations. In some cases

involving physical mixing, the nanomaterials need to be treated with a surfactant to improve dispersion [49, 50]. Other methods of improving dispersion of nanomaterial in a polymer matrix involve in-situ polymerization of a mixture of nanomaterials and monomers, assisted by ultra-sonic mixing [51, 52].

Another important factor controlling the material properties of nanocomposites is the adhesion between matrix and reinforcement phases. While some studies advocate the use of surface functionalization of nanomaterials to improve material properties of the nanocomposite [53, 54], other studies have shown that surface functionalization of nanomaterials leads to an increase in the number of defects at the interface of nanomaterial and polymer, thus leading to poor mechanical properties [55, 56]. Nanocomposites reinforced with functionalized nanomaterials also exhibit superior dispersion [54].

Renaud *et al.* suggested the idea of improving photoresist properties by nanoparticle reinforcement and used them as MEMS structures [57]. Jiguet *et al.* improved properties of the resist to photolithography by incorporating silver nanoparticles in SU8 photoresist matrix. The nanocomposite exhibited an improved conductivity when reinforced beyond the percolation threshold [58]. However, this increase in conductivity is accompanied by difficulties with lithographically patterning the silver/SU8 composite. As such, transparent substrates and backside exposures were required to sufficiently crosslink the composite at the wafer surface. Jiguet *et al.* also reported the synthesis of silica nanoparticle reinforced SU8 photoresist [59, 60]. The resulting nanocomposite was reported to exhibit higher sensitivity, better adhesion,

and lower thermal stresses compared to the parent photoresist, without any loss in resolution.

The nanocomposite photoresists have also been employed to fabricate MEMS structures like beams, posts and meshes, some examples of which are shown in figures 2–11 and 2–12. One of the primary challenges to fabricate MEMS-based structures using these polymer nanocomposites lies in patterning. Zhang *et al.* have overcome this problem by developing a process, involving holographic lithography based three-beam interference process to tailor the geometry of microstructures, and reactive ion etching to create the nanostructured patterns [61].

Figure 2–11: Optical image of a 5 mm diameter wheel made out of SU8 nanocomposite [60].

Seena *et al.* have fabricated cantilevers using a piezoresistive nanocomposite with carbon black nanoparticles dispersed in a SU8 matrix [63, 64]. The dispersion

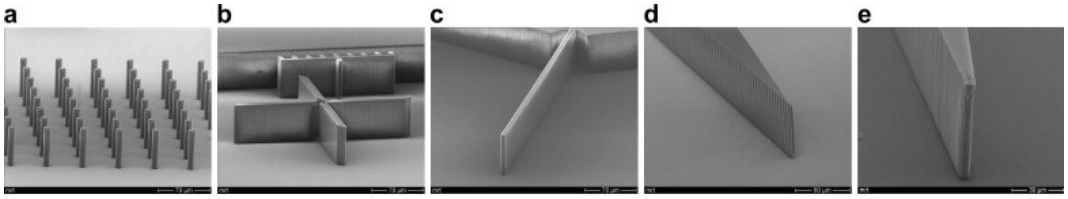

Figure 2–12: Scanning electron microscope images of silica/SU8 nanocomposite MEMS structures (a) 10 μm thick pillars, (b) 10 μm thick cross pattern, (c) 7 μm thick line, (d) 2.5 μm thick tip and (e) 5 μm thick tip [62].

of the nanoparticles was improved by sonication and led to formation of nanocomposites with ∼8–9 % volume fraction of carbon black. The low elastic modulus combined with its piezoresistive properties made it a better candidate for sensing static deflections and has been used as an electronic nose to detect explosive vapour [64]. Figure 2–13 shows an optical micrograph of the nanocomposite cantilevers.

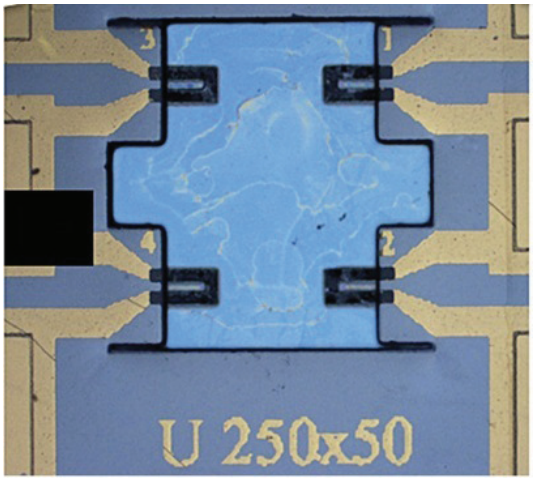

Figure 2–13: Optical image of a set of four carbon black/SU8 nanocomposite microcantilevers. The nanocomposite appears black in the optical image. Each U-shaped microcantilever is 250 μm long, 3 μm thick, and the width of each leg is 50 μm [64].

2.3.2 Vapour deposition

There exist numerous examples of deposition of nanocomposite thin films by sputter deposition techniques, as described in several excellent review articles [65,66]. However, there are a small number of applications of chemical vapour deposition (CVD) to synthesize nanocomposite thin films, since the precursor becomes unstable at the elevated temperatures. Hence, an aerosol assisted chemical vapour deposition (AACVD) method has been developed to deposit metallic nanoparticles in a ceramic matrix [67]. Thin hard nanocomposite coatings of titanium nitride nanoparticles in an amorphous $SiN_{1.3}$ matrix has also been prepared by employing a low temperature CVD process [68].

2.3.3 Directional growth of nanowires and introduction of polymer matrix

Fabrication of unidirectional nanowire or nanotube reinforced composite films is a formidable challenge. One way to achieve this goal is to grow nanotubes or nanowires on a substrate and then deposit the matrix material. Choice of the crystallographic orientation of the substrate and that of the nanowire determines the direction of growth of the nanowire. The choice of the matrix material is constrained by the condition that it should be deposited in such a manner that it fills in a large fraction of the space between the nanowires. This technique has been utilized to fabricate nanocomposites with silicon nanowires in a parylene matrix by Abramson *et al.* [69]. In this work vapour-liquid-solid (VLS) technique has been used for one-dimensional (1-D) growth of single-crystalline vertical silicon nanowires on a Si (111) substrate. The matrix (parylene) was performed by a vapour technique. Deposition

of other polymers like polyimide and polystyrene by spin-coating technique was unsuccessful since their viscosity prevented their penetration in the gaps between the nanowires.

A recent publication has shown a new method to obtain a polymer nanocomposite with horizontally aligned carbon nanotubes. It involves in-situ wetting of a substrate with vertically aligned carbon nanotubes in SU8-epoxy solution, followed by pulling the substrate out of the solution in a directional manner so as to obtain a nanocomposite with horizontally aligned carbon nanotubes [70]. This nanocomposite is hot-baked and densified by compaction to obtain carbon nanotube volume fractions in the range of 40–70%. Aligned polymer nanocomposites can be also be obtained from vertically aligned carbon nanonotubes (VACNTs) grown on silicon wafers by flattening the VACNTs using a roller, and then spin-coating the flattened CNTs with a polymer [71].

2.3.4 Electrochemical deposition

Another method to deposit nanocomposites is by electrochemical deposition from a solution of the metallic salt and nanoparticles. There are two modes of deposition based on whether an external electric current is applied, namely, the electrolytic deposition (or electroplating) and the electroless deposition method. In both cases, the wafer is used as the cathode and the metal ions undergo reduction and form a continuous film on the cathode. In addition to this reaction, nanoparticles with adsorbed ionic species on their surface are transported to the vicinity of the wafer by convection, as is elucidated by Celis *et al.* [72]. On entering the hydrodynamic boundary layer around the wafer, the velocity of these nanoparticles is rapidly

retarded and upon close contact with the wafer, some of the adsorbed metallic ions undergo reduction leading to co-deposition of the nanoparticles in the metallic matrix. This principle has been applied to deposit nickel nanocomposite films with micro- and nano-scale reinforcements [73, 74].

Teh *et al.* fabricated MEMS structures using metal matrix composites [75, 76]. Thin films of nickel with cordierite and diamond nanoparticles were deposited using the electrochemical process, as described earlier. The primary way to get a desired structure using this approach is to pattern a mould, followed by deposition of the metal matrix nanocomposite within the mould and finally releasing the structure by etching away the sacrificial layers. The nanocomposite micro-beam arrays fabricated using this technique was found to have lower residual stresses compared to pristine nickel, as is shown in figure 2–14.

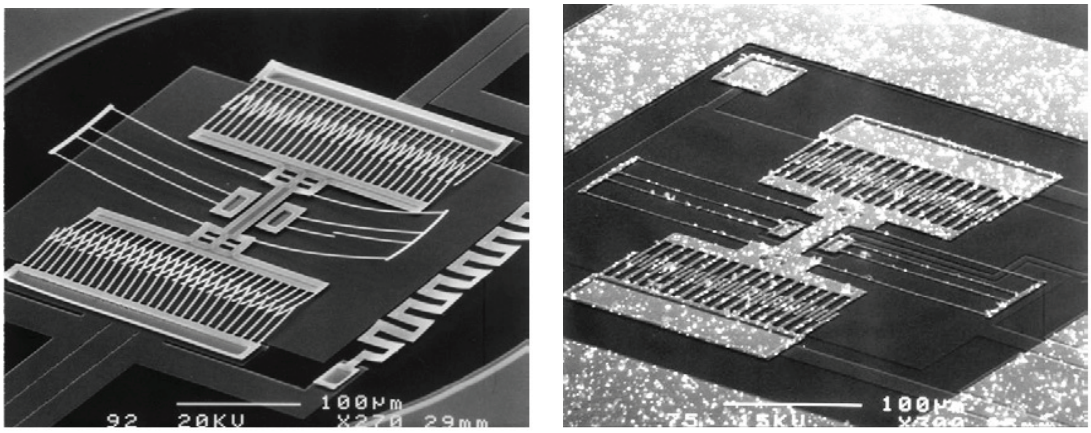

(a) (b)

Figure 2–14: Micromechanical structures fabricated of nickel nanocomposite: (a) A partially released, internally stressed electroless nickel microresonator. (b) A fully released, unannealed, residual stress free, electroless-nickel-cordierite microresonator [76].

Tsai *et al.* fabricated microcantilevers with nickel-diamond nanocomposite using a low temperature stress-free electrolytic deposition process and demonstrated the excellent mechanical strength and power-efficient performance of the microfabricated device [77, 78]. Carbon nanotubes (CNTs) were introduced in phosphorus nickel matrix by Shen *et al.* by an electroless deposition process and this nanocomposite (Ni-P-CNT) was used to fabricate arrays of micro-cantilevers, as shown in figure 2–15 [79, 80].

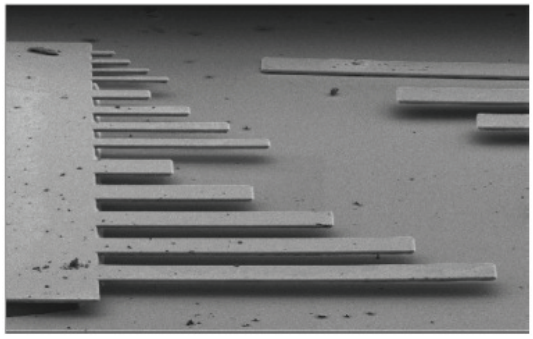

Figure 2–15: Scanning electron microscope (SEM) images of as-fabricated Ni-P-CNT nanocomposite cantilever beam arrays [79]. The thickness of the cantilevers range from 7 μm to 9 μm.

2.3.5 Plasma polymerization-based deposition

A common method employed to make polymer nanocomposites with embedded metallic nanoparticles is plasma polymerization. Plasma polymerization was originally used to deposit thin, continuous, pin-hole free polymer coatings by employing plasma assisted chemical vapour deposition. As the name implies, this method involves polymerization of an ionized gaseous monomer, due to collisions with accelerated electrons in the plasma. Plasma polymerization of organometallic monomers

has been employed to produce nanocomposites with embedded metal and/or metallic oxide nanoparticles. Another way to embed metal nanoparticles is simultaneous plasma polymerization and physical vapour deposition (PVD). The incorporation of metal by PVD mainly involves sputtering or evaporation. Films produced by these methods lead to a very homogeneous distribution of embedded metal particles in the polymer matrix [81].

2.3.6 Sol-gel method

Sol-gel is a popular fabrication method to fabricate porous thin films. This method primarily involves preparation of a colloidal suspension of precursors (sol), gelation of the sol and finally, evaporation of the solvent to obtain the film [82]. The precursors are usually metal alkoxides or their derivatives. The sol-gel solution can easily be cast into complex shape or used to coat substrates. The coating is usually performed during the gelation phase, employing spinning or dipping techniques. Hence, the thickness of the film is a function of the spinning or dipping speeds and the viscosity of the gel-solution. Though predominantly used to make ceramic matrix nanocomposites with metallic [83] or metal oxide [84] nanoparticles, there is an increasing effort to use this technique to produce polymer matrix composites, as is described in reference [85].

In-situ approaches of nanocomposite synthesis have been developed, where metal nanoparticles are generated inside a polymer matrix by solid-state chemical reduction of a metallic precursor present in the polymer thin film [86]. Abargues *et al.* report the synthesis of a nanocomposite electron beam photoresist, in which silver

nanoparticles are embedded in polyvinyl alcohol (PVA) matrix by electron beam exposure of a PVA film containing $AgNO_3$ [87].

2.3.7 Other methods

Other techniques commonly used to deposit nanocomposite thin films include molecular assembly techniques. A combination of Langmuir-Blodgett technique, self-assembly and layer-by-layer deposition techniques can be used to synthesize nanocomposite thin films [88,89]. Jiang *et al.* have fabricated free-standing nanocomposite membranes reinforced with gold nanoparticles, and suspended over micromachined holes by using self-assembled layer-by-layer assembly in conjunction with a sacrificial layer approach. These nanocomposite membranes were found to be suitable for membrane-based acoustic, pressure, chemical, and temperature sensing [89].

2.4 Summary

This chapter presented a review of the literature on integrating nanomaterials with microsystems. Process design and materials integration are challenging because a successful outcome requires careful attention to numerous factors. These factors span the spectrum from local details (for example, whether a specific nanomaterial will adhere to its substrate) to global systems-level interactions (for example, whether the final step of releasing the structure will damage a nanomaterial that was integrated early in the process sequence).

Electron-beam lithography is a well-established technique for patterning nanomaterials. However, there is a gap in the literature when it comes to the use of

electron-beam lithography to integrate nanomaterials directly on micromachined devices. Chapter 3 presents an effort to fill this gap by developing an approach for patterning metallic, polymeric, and nanocomposite structures on micromachined beams and plates. This technique is then used in chapter 5 to measure internal friction in aluminium nanowires.

CHAPTER 3
Integration of nanomaterials with micromachined structures

3.1 Introduction

In chapter 2, the lack of an approach using electron beam lithography to define metallic nanostructures on micromachined MEMS structures was identified. This chapter[1] fills this gap by developing an approach wherein the micromachining steps are completed before integrating the nanomaterial. The advantage of this approach is that the steps used for micromachining are not constrained by thermal or chemical compatibility with the nanomaterial. However, this approach must also confront the difficult challenge of processing the nanomaterial on fragile micromachined structures. Thus, any microfabrication process that generates contact forces will generally damage the micromachined components. For example, dispensing photoresist or electron beam resist by spin coating on freestanding micromachined membranes, plates or beams can cause fracture. To avoid these problems we have developed an approach that combines spray-coating of electron beam resist, physical vapour deposition of thin films, and electron beam lithography. The details of these processes, and the

[1] Parts of this chapter appear in a peer-reviewed article: K. Das, P. Hubert, and S. Vengallatore, "Patterning Nanomaterials on Fragile Micromachined Structures using Electron Beam Lithography", *Materials Research Society Symposium Proceedings*, volume 1299, pp. 61–66, 2011

fabrication of nanostructures on commercial micromachined plates and beams, are described in this chapter.

The remainder of this chapter is organized in the following fashion. Section 3.2 introduces the fundamentals of the spray-coating process and the electron beam lithography process. Section 3.3 considers the integration of polymeric nanostructures on silicon carbide plate resonators. The polymer used in these experiments is an electron beam resist, and these structures were formed using a combination of spray-coating and electron beam lithography. Section 3.4 considers an extension of this method to define metallic nanostructures by using a lift-off technique. This process is illustrated using the example of aluminium nanowires deposited by electron beam evaporation on single-crystal silicon microcantilevers.

3.2 Fundamentals of spray-coating and electron beam lithography

3.2.1 Spray-coating

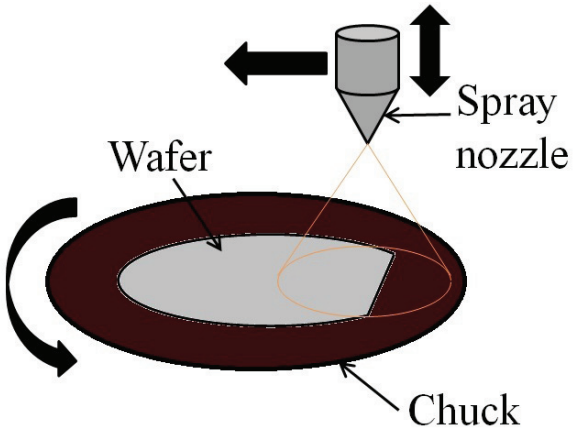

Figure 3–1: Schematic illustration of the spray-coating process.

Spray-coating is a promising technique for coating surfaces having a pre-existing topography with a liquid chemical. It allows conformal coating of non-planar surfaces. The spray-coating device essentially consists of a chuck onto which a wafer is held by vacuum, and an ultrasonic spray-nozzle, which scans over the wafer dispensing a fine mist of the liquid. The wafer-chuck assembly is also rotated at low angular velocities while the spray-nozzle scans the wafer. The height of the spray-nozzle above the wafer can also be programmed to vary as it scans the wafer. A schematic of the spray-coating process is shown in figure 3–1. The spray-nozzle is fed by liquid resist solution (coming from a syringe pump), and a compressed air inlet to facilitate the formation of a fine mist of the resist solution.

The composition and viscosity of the resist solution is one of the most important parameters which controls the thickness, and uniformity of the resist layer. The viscosity of the resist solution should be low enough for the spray-coating system. For example, for the Electronic Visions Group spray-coating system, EVG101, used in this work, the maximum viscosity of the resist solution must be less than 20 cSt. No commercially available photoresist or electron beam resist satisfies this criteria, and hence they must be diluted. Dilution in this context means the addition of an appropriate solvent to reduce the viscosity. A two part solvent is used to reduce the solid content and thin the resist, namely a high vapour pressure (HVP) solvent and a low vapour pressure (LVP) solvent. The HVP solvents are defined as solvents with vapour pressure greater than 70 mm of mercury at room temperature. Examples of HVP solvents are methyl ethyl ketone (MEK), acetone, cyclo methanol, and methyl isobutyl ketone (MIBK). HVP solvent is added to get smaller droplets of the solution

in the mist, since the HVP solvent is expected to evaporate considerably during spraying. The LVP solvents are solvents with vapour pressure less than 20 mm of mercury at room temperature. The LVP solvents are typically the base solvents of the resists. The LVP solvent is expected to stay in the coated film until it is baked, and helps to make the spray-coated film uniform, in terms of its thickness.

An important component of a spray-coating recipe is to use a proper ratio of the HVP solvent to the LVP solvent. Using improper HVP:LVP ratios can lead to imperfections in the coating. The most common and prominent of these imperfections are 'pin-holes' and 'pull-back effects'. Pin-holes appear in the coating when the film is too dry i.e. when the HVP:LVP ratio is higher than that for a good coating. The remedies are to reduce the HVP solvent and/or to increase the LVP solvent. Pull-back effects leading to a wrinkled coating appears when the film is too wet i.e. when the ratio is lower than the ideal value. The remedies in this case are to decrease the LVP amount and/or to increase the HVP amount.

Other parameters which can be controlled in a spray-coating process are the rate at which the volume of the resist solution is dispensed, the scanning speed of the spray-nozzle, the distance of the spray-nozzle from the sample to be coated, the pressure at which the resist solution is sprayed, and the spinning velocity of the chuck and wafer assembly.

Spray-coating of resists is a comparatively new process and can be of great importance in fabrication of intricate three dimensional structures in MEMS devices [90,91]. Spray-coating recipes have been developed for photoresists like AZ4823 [92],

AZ4562 [92], AZ4562-PGMEA [92], AZ4562-MEK [92], and AZ4620 [91]. A recipe for spray-coating of an electron beam resist PMMA A4 has also been developed [93].

3.2.2 Electron beam lithography

Electron beam lithography (EBL) is the process of making patterns with the help of an electron beam. The electron beam, due to its much lower wavelength than that of light, has a much higher resolution. This allows making nanometer-scale patterns, which would have been impossible via conventional photolithography. In general, two schemes have been used in EBL, namely electron projection lithography and direct-write electron beam lithography. Electron projection lithography is analogous to photolithography, and involves projection of a parallel electron beam through a mask on a resist-coated substrate. On the other hand, direct-write electron beam lithography involves using a narrow Gaussian electron beam to write directly on a resist-coated wafer. Unlike the electron projection lithography, the direct-write technique does not require any expensive mask assembly, and has been widely used for patterning masks for photolithography, as well as for making prototype microdevice components since 1960s [94]. Direct-write EBL primarily involves scanning a finely-focused electron beam over the surface of a wafer, and blanking the beam on and off through computer-control. The direct-write EBL system basically consists of an electron-source, a set of condenser lens to focus the beam, a blanker to turn the beam on or off, another set of condenser, deflector and objective lenses for moving the electron beam, and finally a precision-stage for holding and moving the substrate [95]. In direct-write EBL the resist-covered surface of the substrate is exposed one pixel at a time, as the electron beam scans the surface. Exposure of the resist to the

electron beam leads to local chain-scission (for positive resists) or polymer cross-linking (for negative resists) of bonds between the molecules of the resist. Subsequent development leads to removal of the exposed parts of the positive resists and removal of unexposed parts for the negative resists. These patterns formed in the resist can then be used to create nanostructures.

The critical dimension of these nanostructures, namely the linewidth, is related to the spot-size of the beam and to the interaction of the electron beam with the resist/substrate system [95]. The resolution of the EBL is determined by the spot-size of the electron beam. A smaller spot-size is obtained with higher acceleration voltage. When the electron beam hits the resist it undergoes small-angle forward scattering, which leads to broadening of the initial diameter of the electron beam. The forward-scattering can be minimized by using a thin resist. In addition, the electron beam also undergoes back-scattering when it interacts with the substrate. These electrons move back to the resist-layer from the substrate and spread over a much larger volume in the resist, leading to proximity effects, a common patterning issue in EBL.

The most popular technique to create metallic nanostructures using EBL is the lift-off technique. It involves the usual steps of coating the surface with an electron beam sensitive resist, exposure of the resist by rastering a finely-focused electron beam over the resist-coated surface, and development of the resist. This is followed by coating with a thin film of metal using a non-conformal deposition process like electron beam evaporation. Finally the substrate is rinsed with a resist stripper, which dissolves the resist and lifts off the unwanted metallic coating, leaving only

metallic nanostructures in places where the metal came in contact with the substrate. Figure 3–2 shows a schematic of the lift-off process.

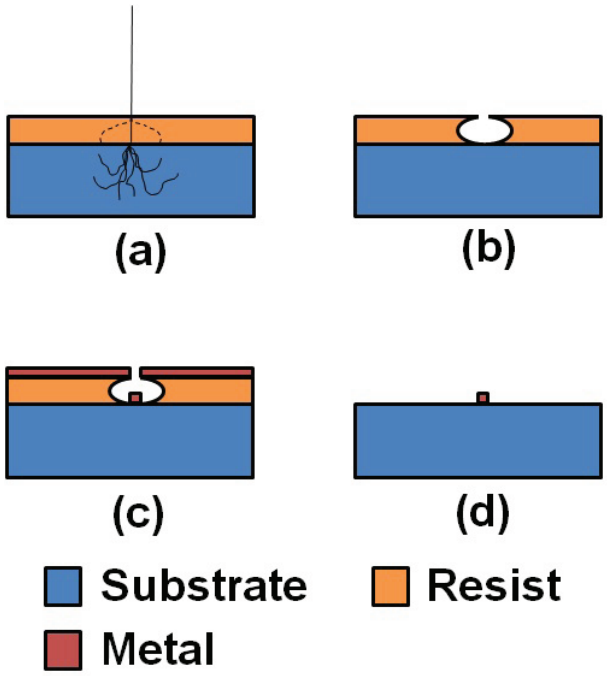

Figure 3–2: Schematic illustration of the EBL lift-off process for a positive resist: (a) Scattering of the focused electron beam in the resist and the substrate, the dashed line showing the boundary of the electron-affected zone; (b) Development of the resist, leading to the removal of the polymer from the affected zone; (c) Deposition of desired material (usually metal) by a non-conformal process like electron beam evaporation; (d) Lift-off of the unwanted materials (polymer and excess metal), leaving the nanostructure on the substrate.

Donthu *et al.* have modified the EBL lift-off process to facilitate fabrication of non-metallic inorganic oxide nanostructures [36]. The modified process involves spin-coating the liquid metal-organic precursor onto substrates with patterned electron beam resist, followed by careful dissolution of the excess material and heat-treatment. This process has been used to make nanostructures of zinc oxide and bismuth ferrite

on various substrates like silicon oxide/silicon, platinum, single crystalline strontium titanate and sapphire [36,37]. This 'soft-EBL' process has also been used to fabricate zinc oxide nanowires on fragile substrates like electron-transparent silicon nitride membranes, as well as on a microhotplate [35].

This concludes the review of the spray-coating and direct-write electron beam lithography processes. The following sections demonstrate the application of these processes to fabricate nanoscale patterns on MEMS devices.

3.3 Patterning on silicon carbide plate resonators

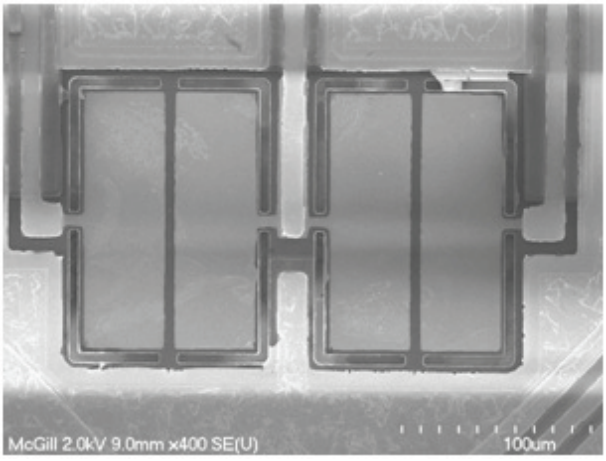

Figure 3–3: Electron micrograph of two plate-mode silicon carbide/aluminium nitride microresonators developed by Boston Microsystems, Inc.. Details of the design and microfabrication of these devices are available in reference [96].

Figure 3–3 shows an electron micrograph of plate-mode microresonators developed by Boston Microsystems, Inc. [96]. As described in reference [96], these structures consist of single-crystal silicon carbide coated with aluminium nitride using molecular-beam epitaxy. Each plate is about 4 μm thick with lateral dimensions of 150 μm$\times$100 μm. These devices are used as resonant sensors, and patterning

nanomaterials on the SiC/AlN plates is of interest for increasing the sensitivity and selectivity of these devices. To this end, the plates were first spray-coated with an electron beam resist (950k PMMA A2, Microchem, Inc.) using EVG101 spray-coater (EVGroup). This resist, which consists of 2 wt% polymethyl methacrylate (PMMA) in anisole, was further diluted with methyl isobutyl ketone (MIBK) so as to reduce the viscosity of the resist and make it amenable for spray-coating. The diluted resist solution contained MIBK and anisole in weight ratio of 3:1. The dispense rate, the nozzle pressure, and the ultrasonic power were maintained at 5 μl/sec, 1000 mbar and 1.4 W, respectively. The spray-coating parameters were optimized for a 4 inch wafer, with the spray-coating being performed from edge-to-edge of the wafer. The number of cycles was varied to achieve the required thickness with minimum surface roughness. The stage was also rotated at 80 rpm, with the direction of rotation (clockwise/anticlockwise) changing at the end of every cycle. The microresonators were then baked at 180 °C for 90 seconds on a hot plate. After 30 cycles of spray-coating, the thickness of resist was measured to be 450$\pm$120 nm.

The spray-coated SiC/AlN microresonators were then patterned using electron beam lithography. The electron beam plotter used in this work is a modified 30 kV field-emission scanning electron microscope (SU-70, Hitachi) with DEBEN stage controller and Nanometer Pattern Generating System (www.jcnabity.com) to control the beam raster as well as to design the pattern. An electron beam operating at 30 kV, with beam current of 357 pA and line doses of 8 nC/cm and 4 nC/cm, were used to pattern arrays of concentric circles and dots in PMMA, as shown in figures 3–4 and 3–5, respectively. The patterns were developed at room temperature by

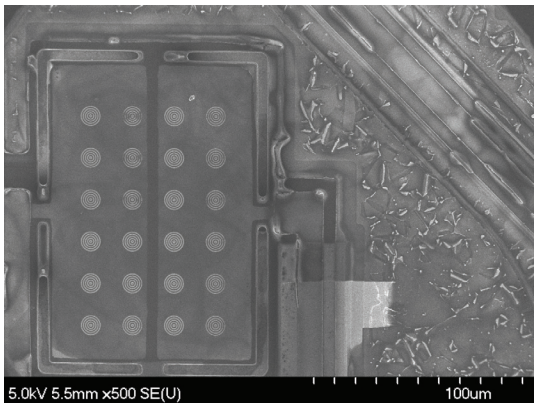

(a) Array of concentric circles

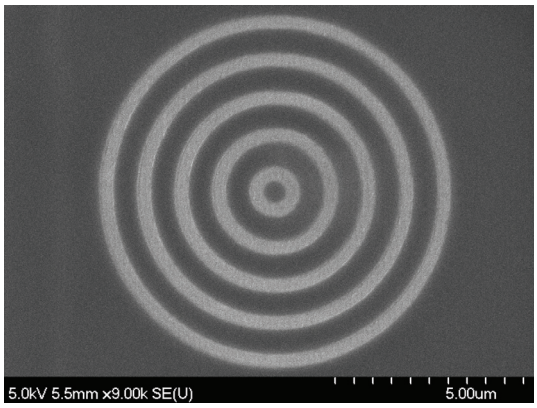

(b) Magnified image of the concentric circles

Figure 3–4: Examples of nanostructures patterned using PMMA on the SiC/AlN plate-mode resonators. The darker regions in this image are PMMA and the brighter regions are 500 nm wide trenches exposing the underlying AlN. A set of five concentric circles were patterned with an electron dose of 8 nC/cm. The diameters of the innermost and outermost circles are 1 μm and 5 μm, respectively. This pattern was replicated across the surface of the resonator with a center-to-center spacing of 20 μm.

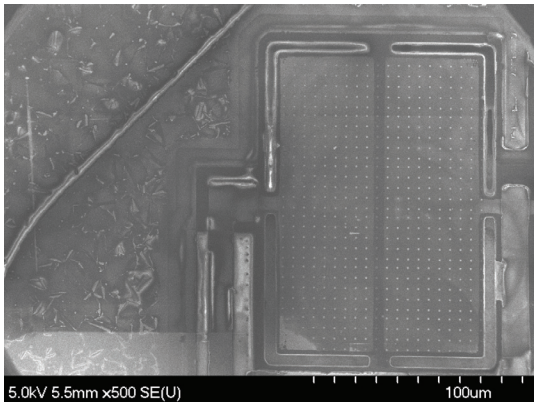

(a) Array of dots

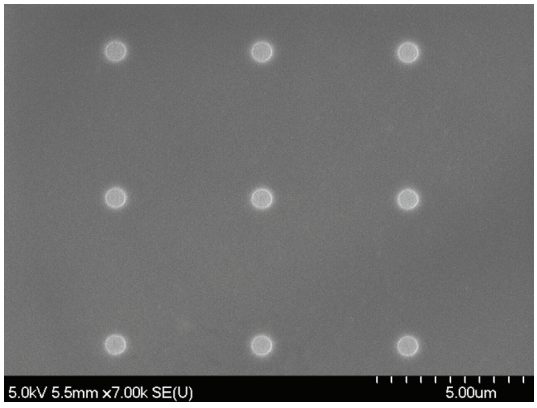

(b) Magnified image of the dots

Figure 3–5: More examples of nanostructures patterned using PMMA on the SiC/AlN plate-mode resonators. The darker regions in this image are PMMA and the brighter regions are the exposed underlying AlN thin film. Arrays of holes with a diameter of $\sim$500 nm and center-to-center spacing of 5 μm are patterned using an electron dose of 4 nC/cm.

immersing the structures for two minutes in a solution that contained MIBK and isopropyl alcohol (IPA) in a ratio of 1:3 by volume. Finally, the specimens were soaked in IPA for 30 seconds and then permitted to dry in air.

3.4 Patterning on AFM cantilevers

Metallic nanostructures were patterned on commercial bulk-micromachined Si cantilevers (NSC16/AlBS, Mikromasch) used for scanning probe microscopy. This integration was achieved by first creating polymeric nanostructures using a process similar to the one described earlier. Subsequently, the metal was integrated using a lift-off technique, as described below. The silicon cantilevers (NSC16/AlBS, Mikromasch) were 230±5 μm long, 40±3 μm wide, and 7±0.5 μm thick. In order to facilitate lift-off, the microcantilever was first spray-coated with a copolymer, MMA-MAA EL11 (Microchem, Inc.). The resist was diluted with MIBK so that the weight ratio of ethyl lactate (EL) to MIBK was 1:1.7, and 5 cycles of spray-coating led to deposition of 390±37 nm of the resist on the microcantilever. The coated cantilever was baked at 150 °C for 90 seconds. This was followed by spray-coating 20 cycles of PMMA A2, which led to deposition of 203±33 nm of the resist. The coated cantilever was again baked at 180 °C for 90 seconds. The bilayer-resist-coated microcantilever was patterned using electron beam lithography with electron doses in the range of 6 nC/cm to 8 nC/cm, and then developed using a solution of MIBK and IPA, as described earlier. Thin films of aluminium were then deposited on the microcantilevers using BJD1800 electron beam evaporator (Temescal) using an operating voltage of 9 kV, emission current of 400 mA, and a background vacuum of 2×10^{-6} Torr. The

deposition rate of Al was 0.2 nm/s. For lift-off, a resist-stripper Remover PG (Microchem Inc.) was heated at 60 °C and the microcantilever was soaked in the heated resist-stripper for 30 minutes. Figure 3–6 illustrates examples of patterns made by this procedure.

A patterned nanocomposite consisting of lines of PMMA completely enveloped by aluminium was also fabricated. The nanocomposite comprises of 450 nm thick and 600nm wide PMMA lines, coated entirely by 60 nm thin film of aluminium. First, patterns consisting of lines with center-to-center distance of 1 μm were made with high electron line-dose of 8 nC/cm, on an aluminium-coated Si cantilever. This high dose leads to lateral spreading of the electrons, leading to wider patterns in the resist. The average width of the trenches in PMMA is around 400 nm. 60 nm of Al is sputter-coated on the patterned PMMA. The parameters used on the MRC603 DC sputtering system were as follows: Argon pressure of 25 mTorr, power of 1.5 kW, scan-rate of 30 cm/min, pre-sputter time of 1 minute, and background vacuum of 1×10^{-6} Torr. This process leads to diffraction grating like structures, as shown in figure 3.4.

3.5 Applications

Coating the entire surface of an AFM microcantilever with a metallic film enhances optical reflectivity, but is also associated with several detrimental side-effects. First, coating the entire surface of a microcantilever with a metallic thin film will lead to a disproportionately large increase in damping [8]. Second, in cases where an optical beam is used to detect deflection of the microcantilever, the metallic coating

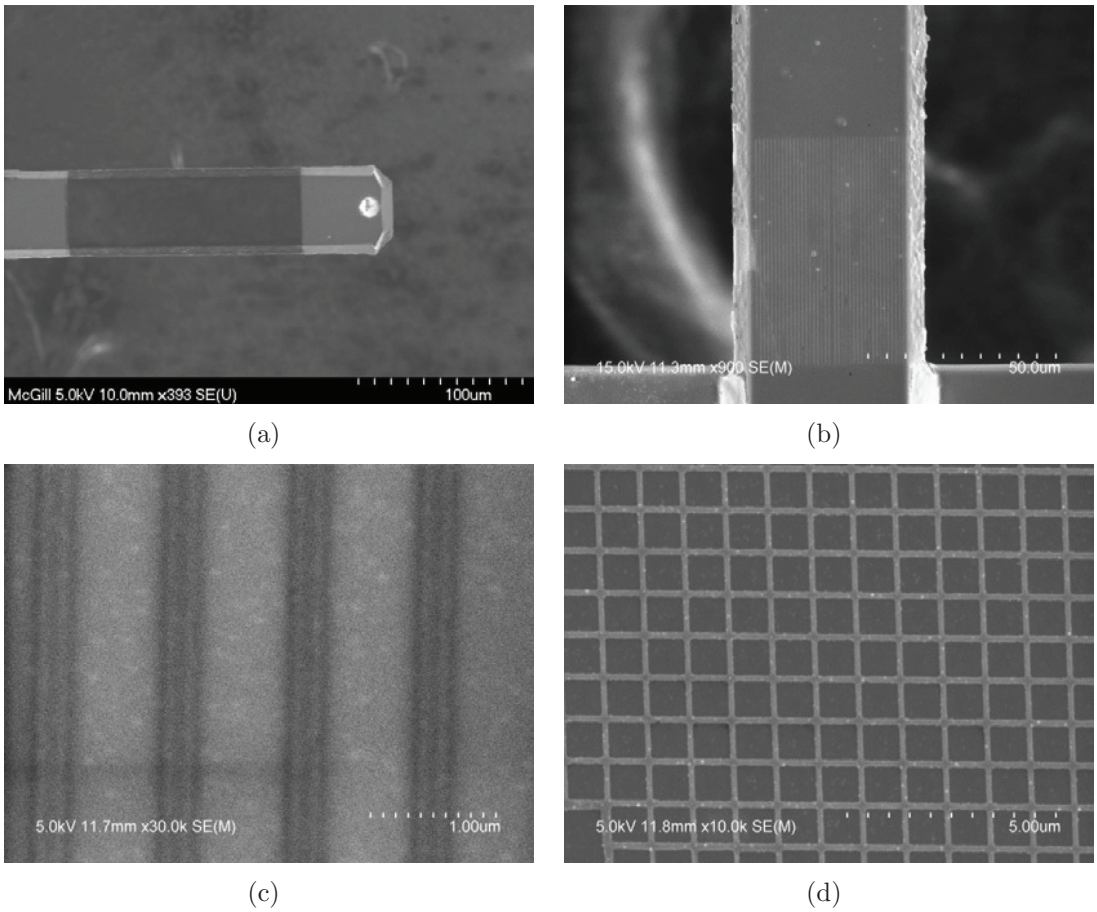

(a) (b)

(c) (d)

Figure 3–6: Electron micrographs of patterns produced on commercial silicon microcantilevers. (a) Selective removal of PMMA from an area measuring 50 μm×50 μm at the tip and base, exposing the underlying silicon. The darker region in the middle of the cantilever is PMMAcoated. (b) Arrays of nanowires were patterned in an area measuring 60 μm×40 μm at the base of the microcantilever using an electron dose of 8 nC/cm. This image shows the structure coated with 11 nm of aluminium before lift-off. (c) Images of aluminium nanowires produced after liftoff. Each nanowire is 11 nm thick and 260±3 nm wide, and aligned along the axis of the silicon microcantilever. (d) Checkerboard pattern of aluminium nanowires on a silicon microcantilever produced using an electron dose of 6 nC/cm. Each nanowire is 50 nm thick and 135±2 nm wide, and the centre-to-centre distance between the nanowires is 1 μm.

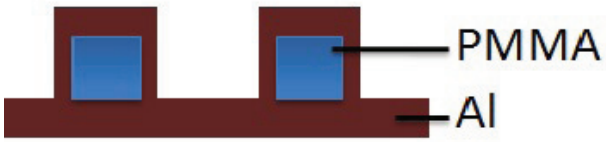

(a)

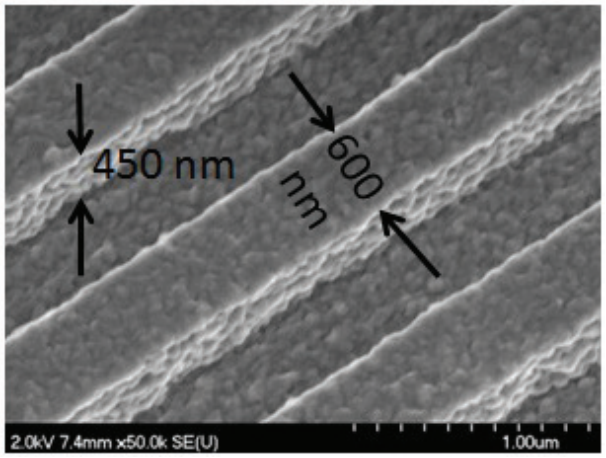

(b)

Figure 3–7: Patterned nanocomposite lines on aluminium-coated Si cantilevers: (a) Schematic cross-sectional image showing PMMA nanowires completely enclosed by aluminium; (b) Scanning electron microscope image of nanocomposite lines. These lines are ≈600 nm in width, and the centre-to-centre distance between adjacent lines is 1 μm. The lines have an inner core of 450 nm thick PMMA, enclosed by 60 nm of aluminium.

couples fluctuations of the light beam power into cantilever bending caused by thermal stresses, and increases noise in measurement of cantilever deflection [97]. One strategy to reduce these detrimental side-effects is to pattern metallic nanostructures on select locations of the cantilever. A recent study has shown that patterning Fresnel lens on the surface of a microcantilever can lead to significant reduction of noise [97]. Another study (closely related to this thesis) has shown that selective metallization of a microcantilever, on locations away from regions of high strain energy such as the root of the cantilever, will lead to a significant decrease in damping [98]. The approach developed in this chapter can be used for such applications aimed at reducing the detrimental side-effects of a full metallic coating.

This approach for integrating nanomaterials with MEMS can also be used for fundamental studies of material properties. One example of such a study is presented in chapter 5. A microcantilever plarform is used to measure dissipation by internal friction in aluminium nanowires.

3.6 Summary

The results presented in this chapter demonstrate the versatility of an approach that combines spray-coating of electron beam resist, deposition of metallic thin films by evaporation, and electron beam lithography to integrate polymeric and metallic nanomaterials on micromachined silicon and silicon carbide resonators. All the micromachining steps are completed before the synthesis and integration of the nanomaterial. Therefore, the choice of the steps used for deposition and etching, which can require harsh chemical or thermal conditions, are not constrained by compatibility with the nanomaterial. However, some standard processes used for patterning must

be modified to account for the low strength of the fragile micromachined components. One example is the use of spray-coating to replace spin coating for dispensing electron beam resist. In this approach to integrating nanomaterials with MEMS, some of the steps like electron beam lithography rely upon serial processes. However, the time required for patterning the micromachined structures is comparable to other serial processes, such as wire-bonding, that are routinely used to produce microelectronics and MEMS. Thus, depending on the application, the value added by the nanomaterial can offset the additional time required for the process of integration.

CHAPTER 4
Characterization of polymer nanocomposites for MEMS applications

4.1 Introduction

Polymer nanocomposites comprise of a class of advanced engineering materials with nanomaterial fillers (in the form of nanoparticles, nanotubes, and nanowires) embedded within a polymer matrix. There is a growing interest to integrate polymer nanocomposites, especially those reinforced with carbon nanotubes to MEMS [70, 99, 100], and is also reflected in this chapter[1] . One potential application of polymer nanocomposites reinforced with carbon nanotubes is for microfabricated electrostatic actuators [99]. Low voltage of actuation, as well as high speed of actuation characterize ideal micro-actuators. The voltage of actuation is directly proportional to the elastic modulus, E, of the material of which the micro-actuator is fabricated. The speed of actuation of micro-actuators is measured in terms of longitudinal wave velocity, which is defined as $c = \sqrt{\frac{E}{\rho}}$, where ρ is the density. Therefore, a material well-suited for functioning as a micro-actuator should possess low elastic modulus

[1] Parts of this chapter appear in peer-reviewed articles: (i) K.Das, C. Park, R. Le Faive, P. Hubert, and S. Vengallatore, "Synthesis and Characterization of Nanocomposite Thin Films for MEMS Applications", *Materials Research Society Symposium Proceedings*, volume 1222, pp. 99–104, 2010; (ii) B. Ashrafi, K. Das, R. Le Faive, P. Hubert, and S. Vengallatore, "Measuring the Elastic Properties of Freestanding Thick Films Using a Nanoindenter-Based Bending Test", *Experimental Mechanics*, volume 52, number 4, 2012

and high longitudinal wave velocity. Figure 4–1 shows an Ashby-type materials selection chart for micro-actuators, where longitudinal wave velocity is plotted against elastic modulus for a wide range of materials [99]. This graph shows that polymer nanocomposites reinforced with uniformly dispersed single-walled carbon nanotubes, aligned along the axis of the micro-actuator, can attain longitudinal wave velocities similar to materials commonly used in microfabrication processes, however at considerably lower elastic moduli.

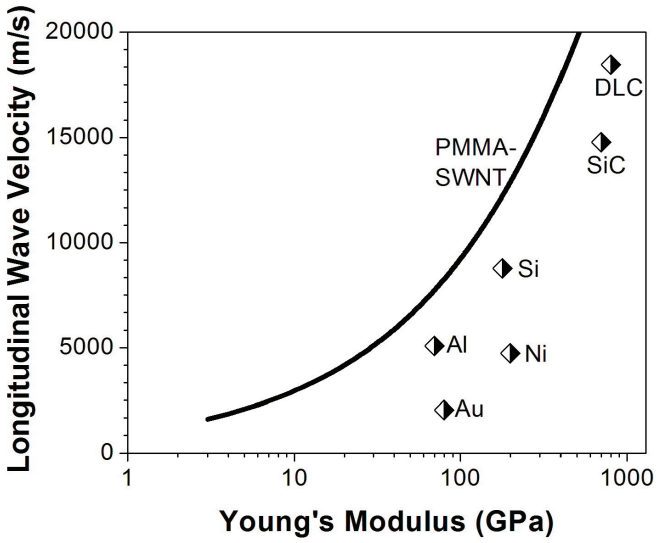

Figure 4–1: Material selection chart for microactuators. The solid curve represents the predictions from Eshelby-Mori-Tanaka micromechanics for a nanocomposite consisting of uniformly dispersed and aligned single-walled carbon nanotubes (SWNTs) in a polymethyl methacrylate (PMMA) matrix [99].

Moreover, using polymer nanocomposites allows tuning of the mechanical properties through control of the volume fraction of the reinforcement phase. Previously, Eshelby-Mori-Tanaka-based micromechanics was used to evaluate the elastic modulus

of polymethyl methacrylate (PMMA) nanocomposites reinforced with single-walled carbon nanotubes (SWNTs), and with multi-walled carbon nanotubes (MWNTs), as a function of the volume fraction, aspect ratio, and orientation of the reinforcements [99]. Similar exercises were also performed for MY0510 epoxy/functionalized SWNT nanocomposites and copolymerized vinyl ester epoxy/functionalized SWNT nanocomposites [101]. Subsequently, MY0510 epoxy and vinyl ester epoxy were reinforced with functionalized SWNTs up to 4 weight% by simple mixing and thin films of the nanocomposites were obtained by casting [99,102]. In addition, carbon nanotube buckypaper films were impregnated with epoxy resin using vacuum impregnation and hot-press techniques to obatin non-dilute nanocomposite films with ∼30–40 volume% of carbon nanotubes [99]. These dilute and non-dilute nanocomposite thin films were mechanically tested using a nanoindenter-based bending test, to obtain elastic modulus of the nanocomposites [102]. In all cases, the experimentally-obtained elastic modulus was lower than the theoretical predictions. It was suggested that poor dispersion of SWNTs and poor bonding at the polymer/nanotube interface were responsible for this discrepany between the theoretical and experimentally-obtained elastic moduli of the nanocomposites [99]. These observations and results motivated the study presented in this chapter.

Polymer nanocomposites were prepared by a method involving in-situ polymerization, and ultrasonic mixing. This method is believed to lead to superior bonding between the nanotube and the polymer, and to uniform distribution of carbon nanotubes in the polymer matrix. The materials and the procedure of synthesis of

nanocomposite films are detailed in section 4.2. Section 4.3 introduces Eshelby-Mori-Tanaka micromechanics and uses it to obtain a theoretical estimate of upper and lower bounds of elastic modulus of the nanocomposites. Section 4.4 describes the nanoindenter-based bending test method that was used to measure the elastic properties of these nanocomposites. The protocol for calibration of the nanoindenter, and the method of selection of maximum load are presented in this section, along with an estimate of the error involved in this technique. The experimentally evaluated elastic modulus of the nanocomposite films are presented in section 4.5 and compared with the predicted elastic modulus. Section 4.6 discusses the results in relation to the microstructure of the nanocomposite films.

4.2 Materials

Eight samples having 2,6-bis(3-aminophenoxy) benzonitrile/4, 4 - oxydiphthalic anhydride [(β-CN)APB/ODPA] polyimide as matrix, with 0, 0.05, 0.1, 0.2, 0.5, 1, 2 and 10 vol% SWNT (produced using High Pressure Carbon Monoxide (HiPCO) process) were provided by National Institute of Aerospace, USA. The procedure for synthesizing these nanocomposites has been described in detail by Park *et al.* [103] and is summarized here. Purified SWNTs processed using high pressure carbon monoxide (HiPCO) were purchased from CNI (Houston, TX, USA). The diameter of SWNT was in the range of 0.85-1.22 nm based on Raman spectroscopy. The SWNT-polyimide composites were prepared by in-situ polymerization under sonication. The diamine and dianhydride, used to synthesize the nitrile polyimide, were 2,6-bis(3-aminophenoxy) benzonitrile ((β-CN)APB) and 4,4 oxidiphthalic anhydride (ODPA), respectively. To prepare the SWNT/polyimide composite, SWNT

dispersed in anhydrous dimethyl acetamide (DMAc) was used as a solvent for the poly(amic acid) synthesis. The entire reaction was carried out with stirring, in a nitrogen-purged flask immersed in a 40 kHZ ultrasonic bath until the solution viscosity increased and stabilized. Sonication was terminated after three hours and stirring was continued for several hours to form a SWNT-poly(amic acid) solution. The resulting solution was cast onto a glass plate and dried in a dry air-flowing chamber. Subsequently, the dried tack-free film was thermally cured in a nitrogen oven to obtain solvent-free freestanding SWNT-polyimide film. A series of SWNT/polyimide nanocomposite films were prepared with SWNT concentrations ranging from 0.05 to 10.0 volume%.

To study the effect of SWNT synthesis and associated dispersion on the mechanical property of nanocomposites, a thin film having the same matrix but with 0.5 vol% laser-ablated (LA) SWNT (Tubes@Rice, Houston, Texas, USA) was synthesized. The procedure of synthesis for this LA-SWNT/polyimide nanocomposite is identical to that of HiPCO-SWNT/polyimide nanocomposite. The thicknesses of the nanocomposite thin films range from 20 μm to 70 μm.

4.3 Estimation of elastic modulus using Eshelby-Mori-Tanaka micromechanics

The prediction of the elastic modulus of a short fibre composite material is a fundamental problem of micromechanics and requires numerical analysis of internal stresses and strains in the composite. The internal stresses arise due to misfit between the shapes of the constituent phases [104]. The numerical analysis is computationally intensive for a reinforcement of arbitrary shape, but an elegant solution exists if the shape of the reinforcement is an ellipsoid, as elucidated by Eshelby's 'Equivalent

Homogeneous Inclusion' approach [105]. This approach involves representing the actual inclusion by one made of the matrix material but with an appropriate misfit strain in order to maintain an equal stress field as that of the original inclusion. However, this approach is valid for a single reinforcement embedded within an infinite matrix and hence can only be applied to 'dilute' systems.

Mori and Tanaka extended Eshelby's approach to 'non-dilute' systems with higher reinforcement content by introducing the concept of average inclusion-volume-fraction-dependent 'background stress' and calculated the average internal stress in the matrix [106]. Benveniste reformulated Mori-Tanaka theory for two-phase composites by suitable approximations of the 'concentration-factor tensor' [107]. This tensor relates the uniform strain in the inclusion embedded in the matrix to the average uniform strain of the composite. Thus the complete elastic stiffness tensor for a two-phase composite is given by [56, 107, 108][2] :

$$\mathbf{C}_c = \mathbf{C}_m + V_f\{(\mathbf{C}_f - \mathbf{C}_m)\mathbf{A}_f\}[(1 - V_f)\mathbf{I} + V_f\{\mathbf{A}_f\}]^{-1} \tag{4.1}$$

where $\mathbf{C}_c$, $\mathbf{C}_m$ and $\mathbf{C}_f$ are the stiffness tensors of the composite, matrix and reinforcement respectively. $\mathbf{I}$ is the fourth order identity tensor, V_f is the volume fraction of the reinforcement phase and curly brackets denote average over all possible orientations defined by the transformation from local coordinates to global coordinates.

[2] A detailed derivation of this equation is provided in Appendix A

$\mathbf{A}_f$ is the dilute mechanical strain tensor and is given by:

$$\mathbf{A}_f = [\mathbf{I} + \mathbf{S}^{-1}(\mathbf{C}_f - \mathbf{C}_m)]^{-1} \tag{4.2}$$

where $\mathbf{S}$ is the fourth-rank Eshelby tensor, components of which are functions of the geometry of the reinforcement and Poisson's ratio of the matrix. The components of the Eshelby tensor for some standard geometrical shapes have been calculated and are readily available in literature [109]. Equation 4.1 is used to evaluate the stiffness tensor for two configurations, namely those of aligned nanocomposites, where all inclusions are aligned in a particular direction, and random nanocomposites where reinforcement are distributed in a random fashion with no specific orientation. Schematic images of these two classes of nanocomposites are shown in figure 4–2.

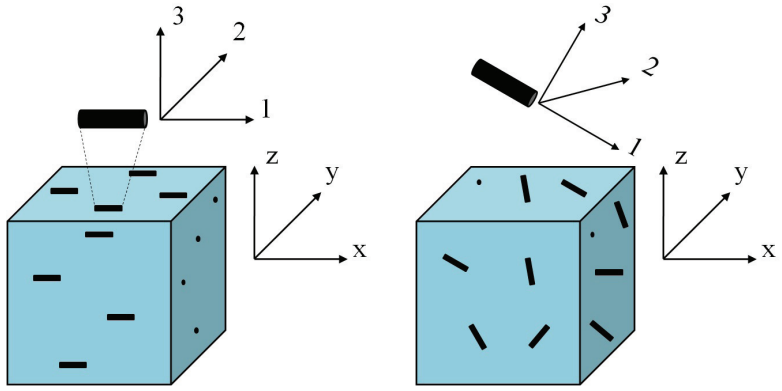

(a) Aligned nanocomposite (b) Random nanocomposite

Figure 4–2: Schematic illustration of the two types of nanocomposites considered: (a) Aligned nanocomposites, where the nanotubes are aligned in a particular direction (emphasized by showing the 1-2-3 local cartesian coordinates of the nanotube aligned to the global x-y-z cartesian coordinates), and (b) Random nanocomposites, where nanotubes do not have any specific orientation (i.e. the alignment of the local and global coordinates are not guaranteed).

In the present work, the PI matrix ([(β-CN)APB/ODPA] polyimide) and SWNT reinforcement have been assumed to be isotropic and transversely isotropic, respectively. The SWNTs are assumed to ellipsoidal, with aspect ratio (s) of 1000. The interfaces between the SWNTs and the polyimide matrix have been assumed to be optimized for perfect load transfer. The dispersion of the SWNTs in the polyimide matrix has also been assumed to be uniform. For the prior estimation of elastic modulus of the composites, the elastic modulus and Poisson's ratio of the matrix have been taken to be 2.7 GPa and 0.4 respectively [51]. Transverse isotropy of the SWNTs demand the use of 5 independent elastic constants. These constants are calculated using the available mechanical properties, namely E_{11} (longitudinal elastic modulus), K_{23} (transverse bulk modulus), G_{12} (in-plane shear modulus), G_{23} (transverse shear modulus), and ν_{12} (major Poisson's ratio) [99, 110, 111]. The indices of these constants relate to the local coordinate system 1-2-3, as depicted in figure 4–2. The values of these constants are provided in the table 4–1. The longitudinal elastic

Table 4–1: Properties of single walled carbon nanotubes [110].

Property	Value
E_{11}	1060 GPa
K_{23}	271 GPa
G_{12}	442 GPa
G_{23}	17 GPa
ν_{12}	0.16

modulus of the aligned and random nanocomposites were evaluated using

$$\mathrm{E_{11}} = \mathrm{C_{1111}} - \frac{2\mathrm{C_{1122}^2}}{\mathrm{C_{2222}} + \mathrm{C_{2233}}} \tag{4.3}$$

where C_{1111}, C_{1122}, C_{2222} and C_{2233} are components of the $\mathbf{C}_c$ stiffness tensor. Figure 4–3 shows the predicted upper and lower bounds of the elastic modulus for the PI/SWNT composites which are calculated using Eshelby-Mori-Tanaka micromechanics.

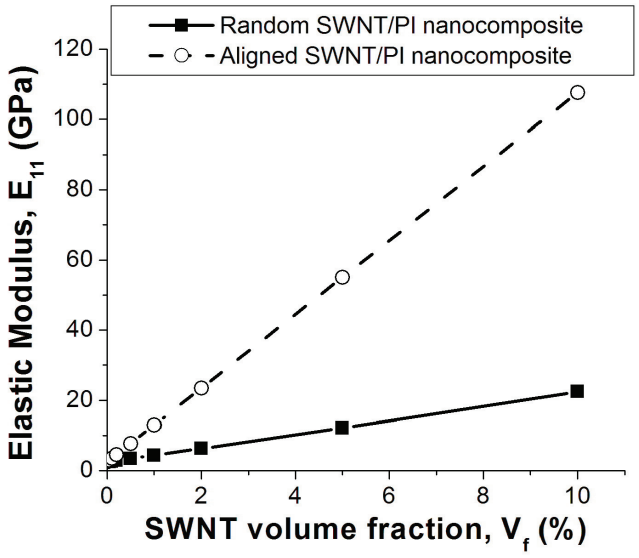

Figure 4–3: Variation of predicted values of longitudinal elastic modulus (E_{11}) of PI/SWNT nanocomposites as a function of volume fraction of SWNT.

This concludes theoretical estimation of elastic modulus of PI/SWNT nanocomposites. The next section presents the method used for experimental evaluation of elastic modulus of free-standing polyimide nanocomposite films.

4.4 Experimental method: Nanoindenter-based bending test

The essential concept of this test is to apply a force to a clamped plate, and to extract the elastic modulus of the plate from the measured load-displacement data. Consider a clamped circular film of radius a and thickness h which is under a force

P applied at the centre of the clamped film by a spherical indenter of tip-radius R, as shown in figure 4–4. The material of the film is assumed to be isotropic and homogeneous with elastic modulus E and Poisson's ratio ν.

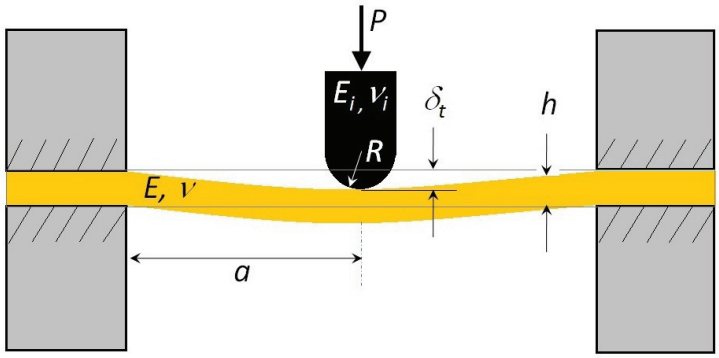

Figure 4–4: Schematic illustration of a clamped circular film of radius a and thickness h loaded centrally with force P, using a spherical tip of radius R. In this work, a diamond spherical tip of radius $R = 100$ μm was used. E and ν refer to the elastic modulus and Poisson's ratio of the film, while E_i and ν_i refer to the elastic modulus and Poisson's ratio of the indenter. The radius a is 1.25 mm.

For small deformation, classical plate theory yields an analytical solution, assuming zero or negligible pre-strain [112], which is given by:

$$\delta_p = \frac{Pa^2}{16\pi D}, \tag{4.4}$$

where δ_p is the deflection at the centre of the clamped circular film. D is the flexural rigidity given by:

$$D = \frac{Eh^3}{12(1-\nu^2)}. \tag{4.5}$$

However, the load is not a point-load, but is applied by a spherical indenter of radius R. This results in an additional contact displacement term while measuring the total

plate deflection (δ_t) under a spherical indenter. Therefore,

$$\delta_t = \delta_p + \delta_c, \tag{4.6}$$

where δ_c is the contact displacement. In the absence of any analytical solution of contact displacement of a clamped circular plate by a spherical tip, Hertz's formula for the indentation of an elastic half-space using a special indenter of radius R has been used as a first approximation to evaluate the contact displacement [113]. Therefore,

$$\delta_c = \sqrt[3]{\frac{9}{16}\frac{P^2}{RE_r^2}}. \tag{4.7}$$

The reduced modulus E_r is defined as:

$$\frac{1}{E_r} = \frac{1-\nu^2}{E} + \frac{1-\nu_i^2}{E_i}, \tag{4.8}$$

where E_i is the elastic modulus, and ν_i is the Poisson's ratio of the indenter tip. It is to be noted that this estimate for the contact displacement does not take into account the finite size and surface roughness of the film [114].

Hence the total plate deflection is given by:

$$\delta_t = \frac{3P(1-\nu^2)a^2}{4\pi E h^3} + \sqrt[3]{\frac{9}{16}\frac{P^2}{RE_r^2}}. \tag{4.9}$$

Equation 4.9 relates the total plate deflection to the applied load, and can be used to evaluate the elastic modulus of the film from the load-displacement ($P - \delta_t$) curves. This requires measuring the geometry of the clamped film (namely a and h), using an indenter of known geometry and material properties (namely, R, E_i, and ν_i), and assuming a value for the Poisson's ratio of the film. The Poisson's ratio of bulk

materials can be used if independent measurements on films are not available, since the Poisson's ratio of a material is insensitive to processing parameters, size-scale, and microstructure [115, 116].

Equation 4.9 is valid only when the deformation is within the linear plate bending regime and will not be valid if membrane stretching becomes significant. Therefore, it becomes essential to select appropriate geometry and loads, so that the deformation regime is that of linear plate-bending. Two non-dimensional parameters, dependent on the applied load and film geometry, have been identified in literature to determine whether or not stretching can be reasonably neglected [117,118]. These parameters are defined as follows:

$$\gamma = \frac{\log\left(\frac{P}{2\pi Eah}\right)}{\log\left(\frac{h}{a\sqrt{12(1-\nu^2)}}\right)} \tag{4.10}$$

$$\lambda = \left[12(1-\nu^2)\right]^3 \left(\frac{Pa^2}{Eh^4}\right)^2 \tag{4.11}$$

The films are considered to be in pure bending regime for $\gamma > 3$ and $\lambda < 85$, provided that the pre-strain in the film is negligible.

4.4.1 Implementation

This sub-section details the implementation of the bending test using a commercial nanoindenter. Calibration of the nanoindenter is described, and finally results on aluminium films are presented to estimate the utility and accuracy of this method.

Implementation of the nanoindenter-based bending test requires a careful consideration of the constraints imposed by the instrument to ensure that the film deforms

in the bending regime, and also to account for the displacement caused by the contact of the indenter with the freestanding clamped circular film. The commercial nanoindenter used is a Hysitron TriboIndenter (Hysitron, Minneapolis, USA), which is capable of measuring force with a resolution of micronewtons, and displacements with a resolution of nanometers. This instrument has a maximum contact-depth displacement of 5 μm, and the maximum load that can be applied is 14 mN. A spherical diamond indenter, with a radius of 100 μm is used. Selection of this indenter is based on the consideration that a larger tip-radius will lead to a smaller contact indentation, but make the test more susceptible to surface roughness. In addition, the range of tip-radii for commercially available indenters also played a role behind this choice of tip radius.

A custom-designed jig is used to secure the film and create a clamped circular free-standing film with a span radius of 1.25 mm [102]. Figure 4–5 shows an exploded schematic of the jig. It consists of two plates that are held together by small recessed hex screws. The lateral dimensions of the plates are 1.25 cm $\times$ 2 cm, and the central cylindrical holes, which define the radius of the clamped circular plate, have a radius of 1.25 mm.

The maximum load that can be applied using this instrument is 14 mN; however, a need to constrain the deformation of the film in bending regime usually necessitates the application of a load which is lower than the maximum applicable load. In addition, the maximum contact-depth displacement of the indenter tip is 5 μm. This puts additional constraints to restrict the load to smaller values.

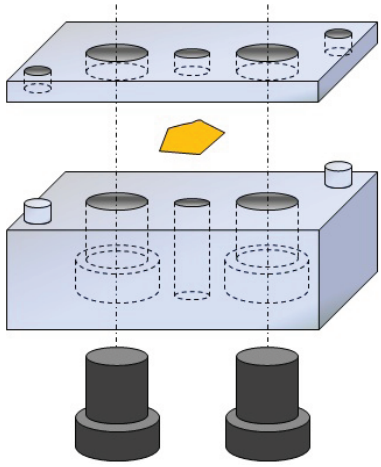

Figure 4–5: Schematic illustration (exploded view) of the jig used for clamping the film (test-specimen). The fixture consists of two plates that are held together by small recessed hex screws. The film is sandwiched between the two plates to create a clamped circular free-standing plate.

Calibration of the nanoindenter

Standard protocols were followed to calibrate the nanoindenter. Special care was taken to ensure that the tip is positioned at the centre of the clamped film and to correct for drift during testing.

The first step towards ensuring minimal error in positioning the tip at the centre of the clamped plate was to calibrate the optics and the stage-movement of the nanoindenter. The stage-optics calibration was performed by allowing the nanoindenter to make seven indents in the shape of letter H on an aluminium standard. Once the indents were done, the centre indent of the H was focused and positioned at the centre of the field of view. This calibration provided the software with coordinates between the center of the focal plane of the optics and the indenter probe. This allowed positioning the tip of the indenter with micrometer precision. The edge

of the hole in the top plate was identified with the optical microscope integrated with the nanoindenter. The coordinates of two sets of diametrically opposite points on the boundary of the circular edge was recorded, and the coordinate of the centre was calculated by taking the average of these four values. Using this procedure, the maximum error in locating the centre of the clamped circular film was found to be 30 μm, which is less than 3% of the radius of the clamped film. Now, the deflection of a clamped circular plate of radius a due to a point load P applied at a point located at a radial distance a_0 from the centre is given by [112]:

$$\delta_p = \frac{3(1-\nu^2)P}{4\pi E h^3}\frac{(a^2 - {a_0}^2)}{a^2}, \tag{4.12}$$

This expression reduces to equation 4.4 when $a_0 = 0$. It follows from equation 4.12 that the error in deflection due to a misalignment of 3% is less than 0.2%, and hence not a significant source of error.

In addition, calibration tests were performed to measure the load-frame compliance of the nanoindenter. The compliance of the instrument was measured to be 3 nm/mN. This value was subtracted from the measured load-displacement curves before analyzing the results.

Testing of a standard material (aluminium thick films)

The first set of tests were performed on a standard material (aluminium films) with well-known elastic properties in order to assess the accuracy of this method. 40 μm thick aluminium films were obtained from a commercial supplier (Goodfellow Cambridge Limited, Huntingdon, England) and cut into pieces with lateral dimensions of 3 mm before testing.

The surfaces of the aluminium films were imaged using scanning electron microscope (Hitachi FEG-SEM S-4700) and tapping-mode atomic force microscope (JEOL JSPM-5200). Representative micrographs are shown in Figure 4–6. The average surface roughness of these films is around 70 nm.

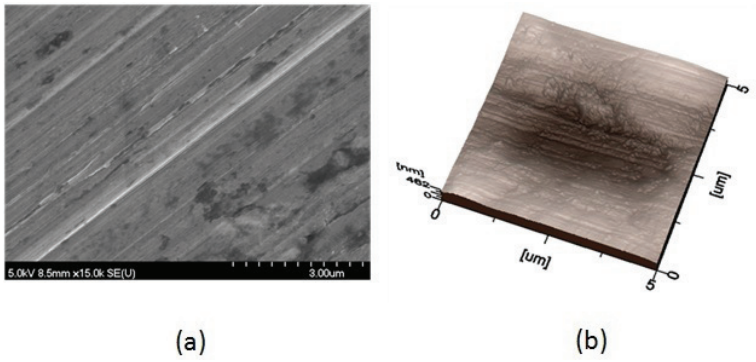

Figure 4–6: Images of the aluminium surface obtained by: (a) scanning electron microscope, and (b) scanning probe microscope.

These films were tested at maximum loads of 2 mN, 6 mN and 10 mN at a loading/unloading rate of 200 μN/s. All tests in this study were performed in the load-controlled mode and in open-loop testing regime. The test loads were selected by following the methodology mentioned in section 4.4, as shown in figure 4–7. In this figure, the applied load P is plotted as a function of the film thickness. The region to the right of the curves $\lambda = 85$ and $\gamma = 3$ represent the applicable loads such that the deformation of the film remains in the plate-bending regime. From the figure, the parameter $\gamma > 3$ is more suitable as a parameter to define the bending regime, since it incorporates the region defined by $\lambda < 85$. In addition, the constraint imposed by the nanoindenter, that the maximum contact-displacement is 5 μm is also incorporated in this figure. The applicable loads for the 40 μm thick aluminium

film are given by the dashed red line in the figure, and the red circles represent the loads at which tests were performed.

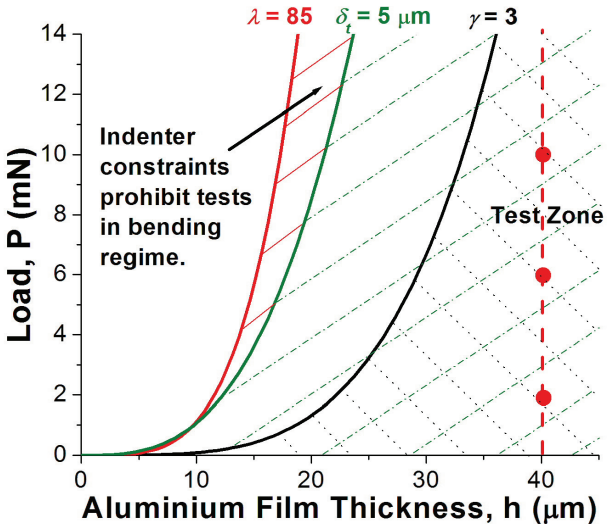

Figure 4–7: Test load determination. The cross-hatched region to the right of $\gamma = 3$ curve is the test-zone, the dashed red vertical line represent the allowable test loads for 40 μm thick film; the red circles represent the loads at which tests were performed.

Figure 4–8 shows a representative example of a load-displacement curve for a specimen tested to a maximum load of 10 mN. Examination of the specimen after testing revealed evidence of inelastic deformation at the clamping regions and at point of contact with the indenter. The elastic modulus of the film was extracted by performing nonlinear regression analysis analysis on the initial portion of the unloading curve in order to exclude the effects of any localized plasticity. In the nonlinear regression method employed here, in order to adjust theoretical (regression-fit) curve both in its shape and position to best match the data curve, a displacement

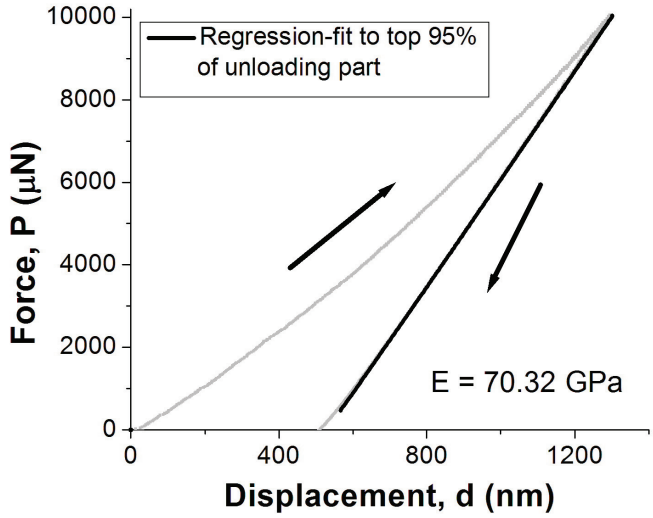

Figure 4–8: Load-displacement plot for a 40 μm thick aluminium film tested to a maximum load of 10 mN. The elastic modulus is extracted by performing nonlinear regression analysis on the initial 95% of the unloading curve.

offset term δ_0 is included in equation 4.9, so that,

$$\delta_t = \frac{3P(1-\nu^2)a^2}{4\pi E h^3} + \sqrt[3]{\frac{9}{16}\frac{P^2}{RE_r^2}} + \delta_0. \tag{4.13}$$

The regression is performed by assuming the load measurements to be error-free, and by using the *fminsearch* function in MATLAB, to find the values of E and δ_0 which minimize the sum of the squared errors between the displacement data and the fitted curve. Figure 4–9 summarizes the results of this analysis. Each datum in this plot corresponds to the average of ten tests. In addition, no significant difference was found when different portions (85%, 75%, and 65%) of the unloading curve were used for the regression analysis. In all cases, the mean value of the Young's modulus is in good agreement with the polycrystalline average value for bulk aluminium (70

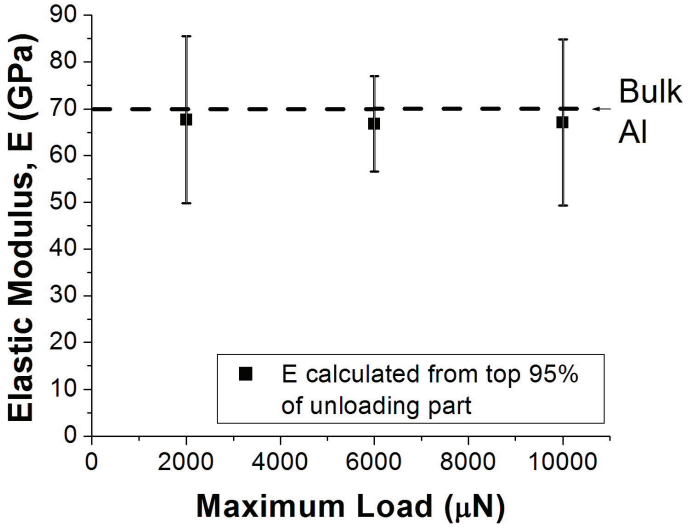

Figure 4–9: Variation of elastic modulus with maximum load. All results correspond to a loading/unloading rate of 200 μN/sec.

GPa) [116], as expected for thick films of this material. Tests were also conducted at three different loading/unloading rates of 10 μN/sec, 200 μN/sec, and 1000 μN/sec to study the rate-dependence. The variation of elastic modulus as a function of unloading rate is illustrated in figure 4–10. Each datum in this plot corresponds to an average of ten tests. The low value of average elastic modulus obtained using the unloading rate of 10 μN/sec is not yet well-understood. However, for tests with unloading rates of 200 μN/sec and above, the evaluated elastic modulus of the thick aluminium films are similar to the elastic modulus of bulk aluminium. Evaluation of the strain-rates during unloading revealed that the strain-rate was not constant. However, as shown in figure 4–11, for the unloading rate of 200 μN/sec, the strain rates remain within the quasi-static regime.

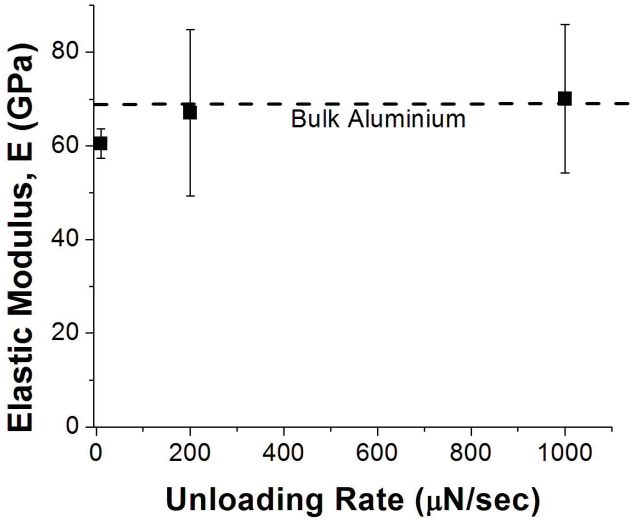

Figure 4–10: Variation of elastic modulus of 40 μm thick aluminium film with unloading rate. All measurements correspond to a maximum load of 10000 μN.

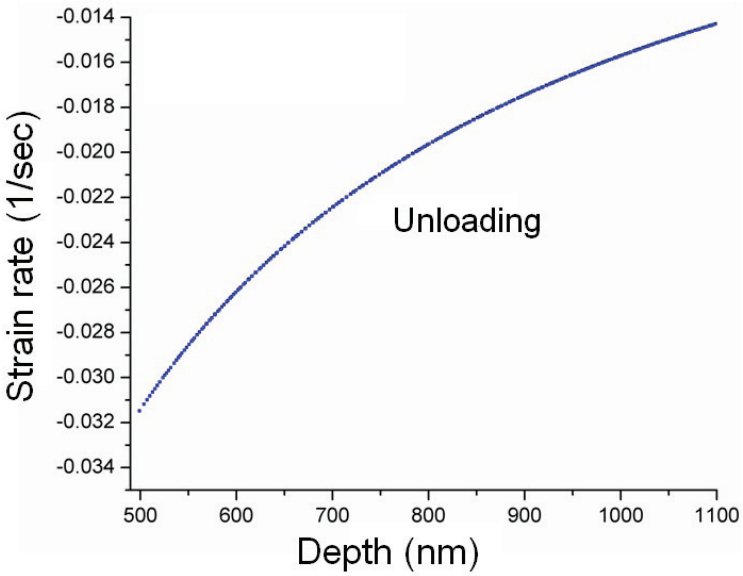

Figure 4–11: Variation of strain-rate in the top 95% of the unloading part of the load-displacement plot. The strain-rate corresponds to an unloading rate of 200 μN/sec.

This concludes the description of implementation of the bending test performed using a commercial nanoindenter. The accuracy of the test was assessed by measuring the elastic properties of a standard material, namely aluminium, and the effect of the maximum loads and the applied unloading rates on the elastic modulus of 40 μm thick aluminium films were studied. Application of the methodology discussed and implemented in the previous sections requires the deformation of the film in bending regime. Determination of such loads using equation 4.10 require an estimate of the range of possible values of the elastic modulus of the composite. In the case of aluminium film, bulk value of elastic modulus of aluminium was utilized; however, for novel nanocomposite materials, where bulk values of elastic modulus are not available one has to resort to micromechanics-based schemes in order to estimate the properties of the composite from the properties of their components. The procedure for doing so was described in section 4.3.

4.5 Experimental results for nanocomposite films

Table 4–2 shows the maximum loads that can be applied to the SWNT/PI nanocomposite films while maintaining the deformation in the bending regime. This table also lists the film thickness, concentration of SWNT, predicted value of elastic modulus of random nanocomposites used for this calculation, as well as the predicted maximum load evaluated using the parameter $\gamma > 3$. All load-displacement tests were carried out using the protocol that was established using the aluminium films, as discussed previously in subsection 4.4.1. All tests were performed at a loading/unloading rate of 20 μN/sec, and the elastic modulus was extracted from the top 95% of the unloading part of the load-displacement plots. Figures 4–12, 4–13,

Table 4–2: Maximum load used in nanoindenter-based bending test for the nanocomposite films. The row with (*) refers to the LA-SWNT reinforced nanocomposite.

SWNT concentration (volume%)	Film thickness (μm)	${E_{11}}^{predicted}$ (GPa)	${P_{max}}^{\gamma=3}$ (μN)	${P_{max}}^{used}$ (μN)
0	60	2.5	4070	3800
0.05	44	2.60	1220	800
0.10	53	2.69	2670	1800
0.20	50	2.89	2260	1800
0.50*	22*	3.46*	102*	50*
0.50	46	3.46	1940	850
1	52	4.42	4060	3800
2	63	6.63	12520	3800
10	26	22.41	1290	400

4–14, 4–15, 4–16, 4–17, 4–18 and 4–19 show typical load-displacement plots for the HiPCO-SWNT/PI nanocomposites. Figure 4–20 shows a typical load-displacement plot for the LA-SWNT/PI nanocomposite.

The measured variation of elastic modulus of SWNT/PI nanocomposites as a function of SWNT content is shown in figure 4–21. Each datum in figure 4–21 corresponds to results from a set of ten experiments. The elastic modulus initially increased from ∼2.5 GPa for pristine polyimide to ∼3.5 GPa when reinforced with 0.5 volume% of HiPCO-SWNT. However, with further increase in the content of this type of SWNT, the elastic modulus remained essentially constant at 3.5 GPa, even for high nanotube loading of 10 volume%. Intriguingly, the one specimen reinforced with 0.5 volume% LA-SWNT shows significantly different results. The average elastic modulus of this specimen was 4.8 GPa, which is higher than that of any of the nanocomposites reinforced with HiPCO-SWNT. The dashed line in figure 4–21 shows the expectation based on Eshelby-Mori-Tanaka micromechanics. This line was

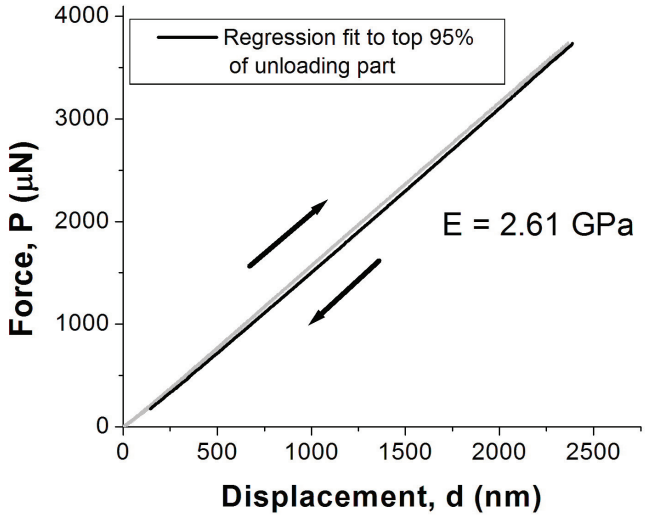

Figure 4–12: Representative load versus displacement plot for pristine PI.

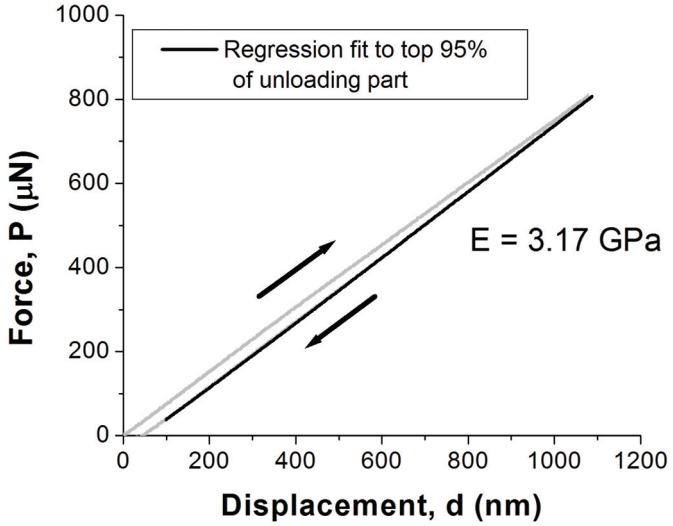

Figure 4–13: Representative load versus displacement plot for 0.05 volume% HiPCO-SWNT/PI nanocomposite.

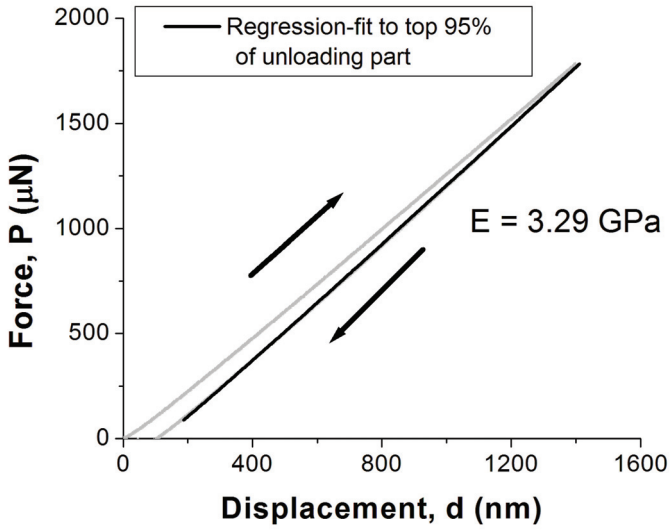

Figure 4–14: Representative load versus displacement plot for 0.1 volume% HiPCO-SWNT/PI nanocompite.

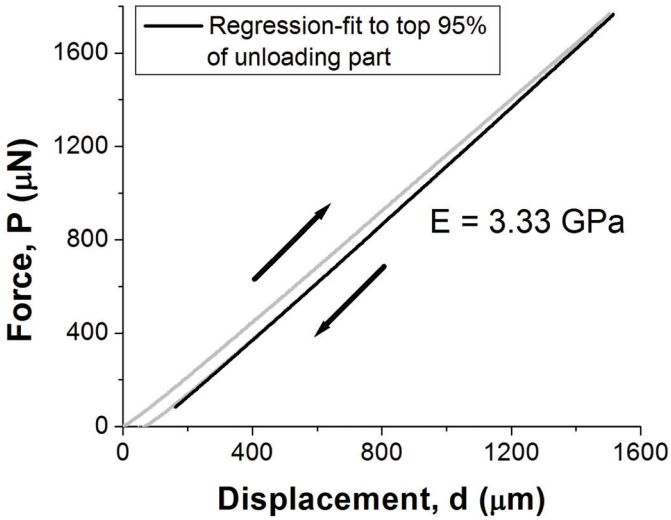

Figure 4–15: Representative load versus displacement plot for 0.2 volume% HiPCO-SWNT/PI nanocomposite.

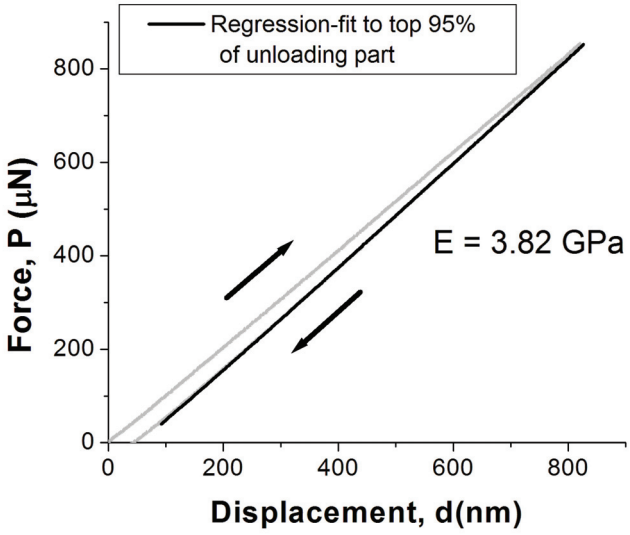

Figure 4–16: Representative load versus displacement plot for 0.5 volume% HiPCO-SWNT/PI nanocomposite

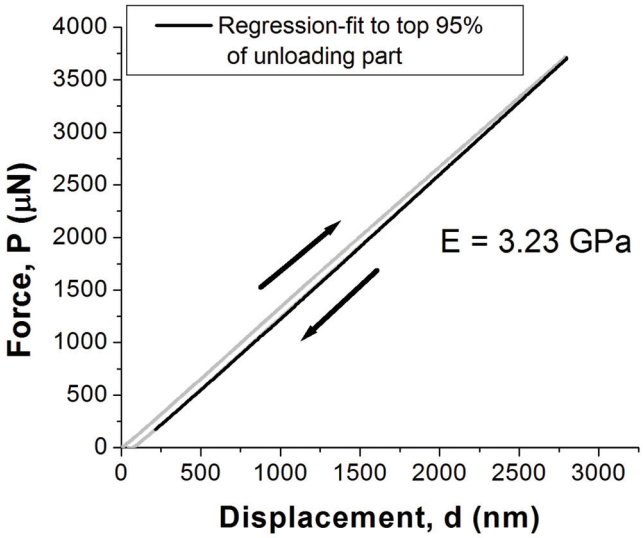

Figure 4–17: Representative load versus displacement plot for 1 volume% HiPCO-SWNT/PI nanocomposite

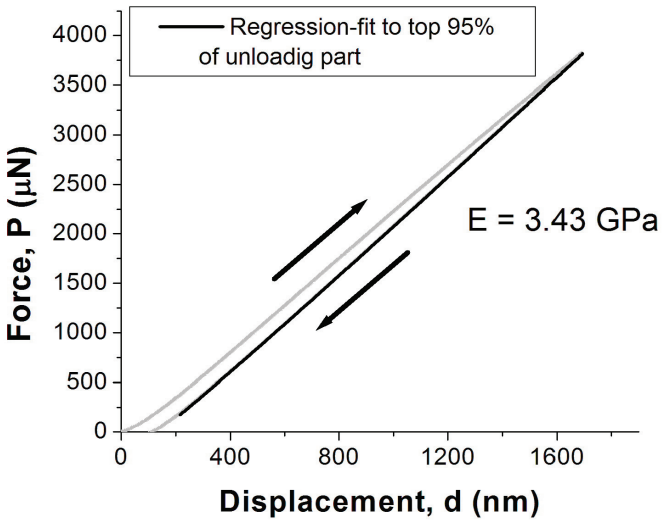

Figure 4–18: Representative load versus displacement plot for 2 volume% HiPCO-SWNT/PI nanocomposite

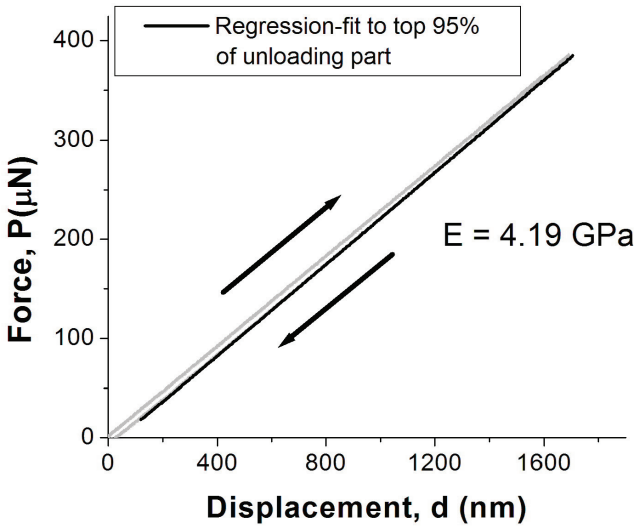

Figure 4–19: Representative load versus displacement plot for 10 volume% HiPCO-SWNT/PI nanocomposite

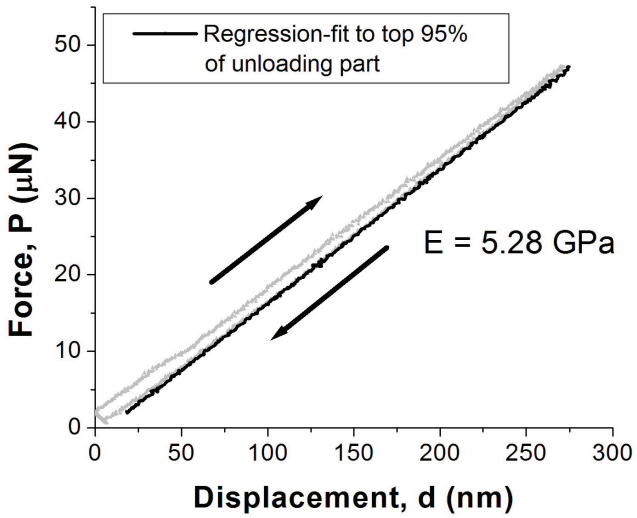

Figure 4–20: Representative load versus displacement plot for 0.5 volume% LA-SWNT/PI nanocomposites.

calculated by assuming polyimide as the matrix, uniformly dispersed SWNT with an aspect ratio of 1000 as the reinforcement, and a perfect load transfer between matrix and nanotubes. In addition, the nanotubes were assumed to be randomly aligned within the matrix. The comparison in figure 4–21 shows that the model is in good agreement with measurements only for the dilute nanocomposites with SWNT concentration less than 0.5 volume%.

4.6 Discussions

One of the factors for the relatively low elastic modulus of polyimide films reinforced with HiPCO-SWNT is the poor dispersion of the reinforcement within the matrix. Figure 4–22 shows polymer-transparent scanning electron micrographs at the same magnification for nanocomposite films containing 1 volume%, 2 volume%

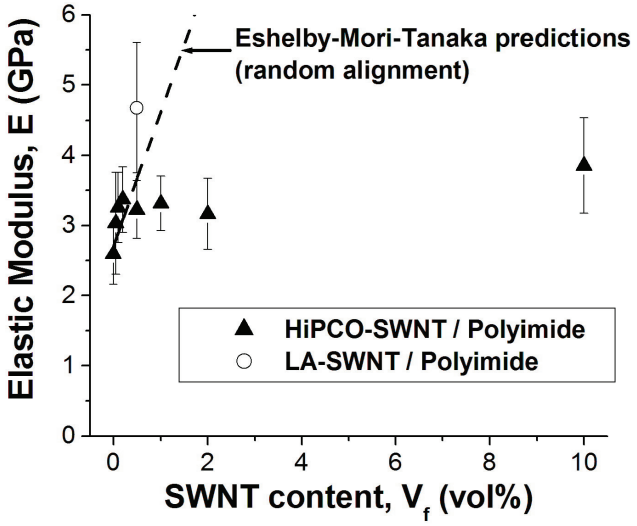

Figure 4–21: Variation of elastic modulus of SWNT/PI nanocomposites as a function of SWNT content.

and 10 volume% of SWNT. It is evident from these images that the nanotubes aggregate form narrow bundles, and that some bundles coalesce to form ropes and ribbon-like structures. These features lead to inefficient load transfer between matrix and nanotubes, which in turn affects the mechanical properties.

In stark contrast, the nanocomposite films reinforced with LA-SWNT show significantly better dispersion, as shown in figure 4–23. The detailed quantitative analysis of these images has been previously reported [52, 119]. In addition, the SWNT-bundles are much thicker in HiPCO-SWNT nanocomposites. Thicker SWNT bundles reduce the interfacial area between the SWNTs and the matrix, leading to reduced load transfer between the matrix and the reinforcement. These images suggest that superior dispersion and narrow SWNT bundle-sizes are the main factors for the increase in elastic modulus for the nanocomposite reinforced with LA-SWNT. SWNTs

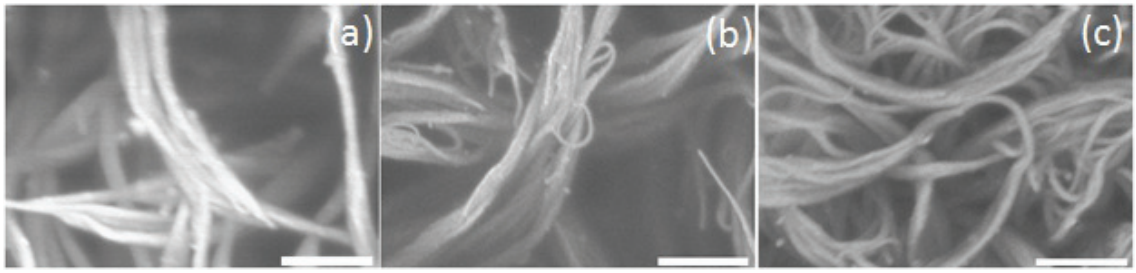

Figure 4–22: Scanning electron micrographs of HiPCO-SWNT/PI nanocomposites with varying SWNT concentrations: (a) 1 volume%, (b) 2 volume%, and (c) 10 volume%. The scale bars in these micrographs represent 500 nm.

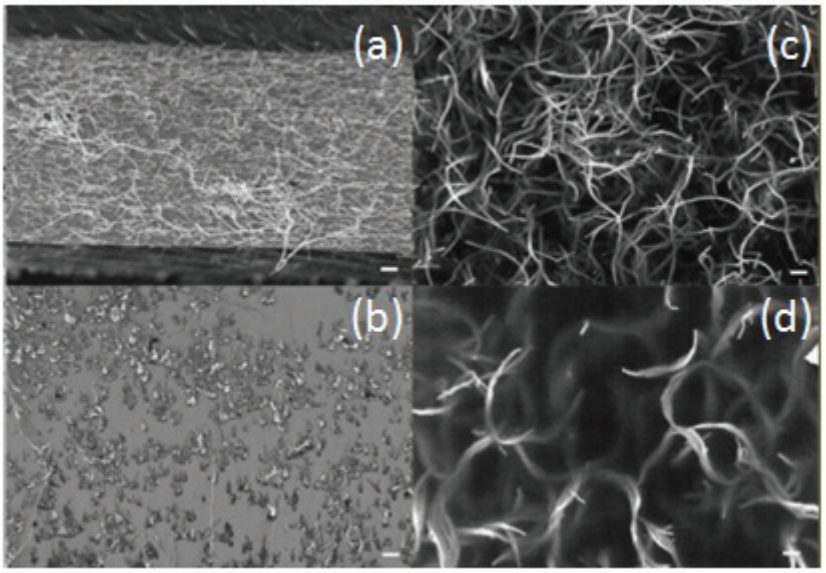

Figure 4–23: Cross-sectional scanning electron microscope images at low accelerating voltages ($\leq$ 1 kV): (a) 0.5 volume% LA-SWNT/PI and (b) 0.5 volume% HiPCO-SWNT/PI. Scale bars in (a) and (b) represent 1 μm. Scanning electron micrographs at high accelerating voltages ($\geq$ 5 kV): (c) 0.5 volume% LA-SWNT/PI and (d) 0.5 volume% HiPCO-SWNT/PI. Scale bars in (c) and (d) represent 500 nm. (Images reproduced from references [119] and [52])

produced by laser ablation have lower levels of contamination and lower densities of defects than those produced by other techniques such as HiPCO [120]. In addition, differences in the techniques used for purification of HiPCO-SWNTs and LA-SWNTs, can also cause different surface chemistries, leading to differences in interaction of the CNTs with each other and with the polymer matrix.

It is to be noted that the processing techniques for the synthesis of nanocomposites used in this work primarily aimed to improve distribution of the nanotubes in the matrix. However, beyond 0.5 volume% of HiPCO-SWNT, the experimentally evaluated elastic modulus of the nanocomposites is less than the theoretical value for uniformly dispersed and randomly aligned nanocomposite, signifying that in-situ polymerization and ultrasonication techniques are ineffective beyond 0.5 volume%. A surfactant can be used to enhance dispersion [49,50], however the effect of addition of the surfactant needs to be characterized.

4.7 Summary

In summary, the elastic moduli of polyimide films reinforced with SWNT at volume fractions ranging from 0 to 10% was measured. For dilute composites, the elastic modulus increased with increasing nanotube loading from 2.5 GPa for the neat polymer to 3.5 GPa for a nanocomposite containing 0.5 volume% of SWNT. However, with further increase in the nanotube content, the elastic modulus remained essentially constant even for high loadings of 10 volume% of SWNT. In addition, significantly different elastic moduli were measured for specimens containing the same volume fraction (0.5 volume%) of SWNT produced by two different processes.

These results vary considerably from the predictions obtained using Eshelby-Mori-Tanaka micromechanics, and highlight the need for the developing new techniques to better control the alignment and dispersion of the nanotubes in the polymer matrix.

CHAPTER 5
Damping in aluminium nanowires integrated to a microcantilever platform

5.1 Introduction

Miniaturized mechanical resonators are ubiquitous in microsystem technologies. Depending on their size, these miniaturized resonators are commonly referred to as micromechanical resonators or nanomechanical resonators. These devices are capable of vibration over a wide spectrum (10^2 Hz to 10^9 Hz) in a variety of modes (including bending and torsion of plates and beams). The use of miniaturized resonators as sensors has led to many impressive achievements. These devices have been able to detect forces and masses as small as 10^{-21} N and 10^{-21} grams, respectively [121]. Applications for micro- and nanomechanical resonators include sensing, imaging, signal processing, and vibration energy harvesting. For all these applications, it is desirable for the resonator to oscillate with low damping to improve sensitivity and frequency selectivity. Therefore, low-loss ceramic materials such as silicon and silicon carbide are used to make these microresonators.

In many cases, these miniaturized resonators are coated with metallic nanomaterials in the form of nanocrystalline thin films and patterned nanostructures to add new functionalities such as optical reflectivity, electrical conductivity, and surface chemistry. Unfortunately, the addition of new functionalities is frequently accompanied by a severe degradation in performance because the nanomaterials cause a

large increase in damping [8]. Even though the volume fraction of the integrated nanomaterial is small (ranging from 1 to 10%), damping can increase by an order of magnitude at some frequencies for some materials. Hence, strategies must be developed to decrease the damping, and optimize the performance and functionality, of the nanomaterial-coated microresonator. An essential input for these strategies is the value of damping of nanostructured thin films and nanowires.

The intrinsic material-related damping in nanostructured materials is due to the irreversible motion of crystallographic defects like vacancies, interstitials, dislocations, grain boundaries, phase boundaries, and twin boundaries. These defect-induced damping mechanisms are collectively referred to as internal friction. At present, little is known about the magnitude of internal friction in nanostructured thin films and in other nanostructured materials (such as nanowires and nanotubes). Therefore, it is necessary to undertake systematic measurements of internal friction in nanostructured materials as a function of temperature and frequency to establish process-structure-damping relationships. These relationships can then be used to guide the design of nanomaterial-integrated microresonators with optimal performance and functionality.

Several challenges must be solved in order to measure internal friction in nanostructured materials. Standard methods for actuating the structure and measuring vibration cannot be used because of the small size of the specimen and the small amplitude of vibration (often in the range of a few nanometers). Over the past decade, many new methods have been developed for dynamic characterization of thin films and nanowires. For example, electrical field-induced mechanical resonance tests have

been conducted inside a transmission electron microscope (TEM) to measure the resonance frequency and quality factor of individual carbon nanotubes [122], boron nitride nanotubes [123], zinc oxide nanobelts [124], and silicon carbide nanowires [125]. Optical interferometry has been used to characterize resonance characteristics and quality factors of silicon nanowires [126] and SiCN nanowires [127].

Even when these technical challenges are solved, it is difficult to calibrate measurements of damping made on free-standing monolithic nanomaterials. The essence of this difficulty lies in the difference between structural damping and material damping. When the measurement is made on a structure (such as a cantilevered or doubly-clamped nanowire), the resulting value of structural damping contains contributions from both extrinsic sources (such as losses from the supports and clamps) and intrinsic sources (internal friction). The extrinsic sources are not sufficiently well understood and their values cannot be predicted with confidence. Therefore, it is not possible to subtract all extrinsic contributions to structural damping obtained from free-standing nanomaterials.

An approach for solving this difficulty has recently been developed at McGill University. This approach combines the use of a composite microcantilever resonator with the ability to calibrate all measurements against the fundamental limits of thermoelastic damping. A silicon microcantilever platform has been developed and used to measure internal friction in thin films of aluminium, silver, and gold [8,98]. In this thesis, the capabilities of this microcantilever are extended to measure internal friction in nanostructured materials. The capabilities of the extended technique are

demonstrated by obtaining the first calibrated measurements of internal friction at room temperature in aluminium nanowires.

The remaining sections of this chapter are organized in the following fashion. Section 5.2 provides a discussion of the various extrinsic and intrinsic mechanisms of damping in microcantilever resonators. This information is useful for understanding the capabilities and limitations of the microcantilever platform. Subsequently, section 5.3 introduces the microcantilever platform. The extension of this platform to measure internal friction in nanowires requires developments on two fronts: developing experimental methods for integrating nanowires on the microcantilever, and formulating a model for the vibrations of the composite microcantilever to extract internal friction from structural damping. Section 5.4 presents the model and section 5.5 contains all experimental details of processing and measurement. Finally, section 5.6 presents results for internal friction in aluminium nanowires and section 5.7 proposes a mechanism for internal friction in these nanomaterials.

5.2 Mechanisms of damping

Mechanical damping is an estimate of the total energy dissipated per cycle of vibration, and is quantified in terms of the mechanical quality factor (Q-factor) or logarithmic decrement (δ, in case of free decay). For cases where energy dissipation is low, Q-factor and δ are related to the ratio of energy of vibration (W) and the energy lost per cycle (ΔW) by:

$$\delta = \frac{\pi}{Q} = \frac{\Delta W}{2W}. \tag{5.1}$$

A high value of Q-factor or a low value of δ denotes low damping while a highly damped structure will have a low Q-factor and high δ. Damping in microresonators arises from several sources: viscous damping, clamping losses, support losses, internal friction, and thermoelastic damping.

Viscous damping is the damping due to external environment of the microcantilever. A microcantilever operated in air or in any fluid medium is usually characterized by low Q-factors due to air-damping [128], squeezed-film damping [129], and complex interactions between the fluid and the vibrating structure [130]. For example, the Q-factors of microcantilevers operating in air under atmospheric pressure is limited in the range of 10–100, and to much lower values in a liquid medium [131]. Therefore, the microcantilevers must be operated in a low pressure or vacuum environment in order to achieve quality factors in the range of 10^4–10^6, which are required by most MEMS applications.

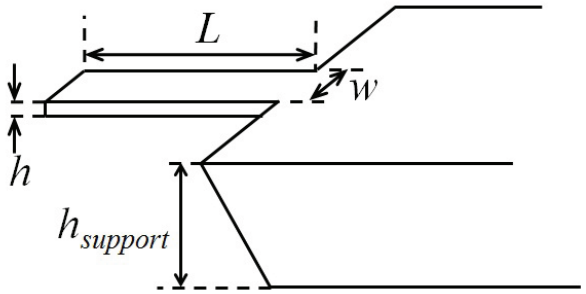

Figure 5–1: Schematic illustration of a microcantilever.

The geometry-dominated damping consist of two components, namely anchor losses, and clamping losses. Microcantilevers are usually attached to a much larger substrate for the convenience of handling, packaging and assembly. Figure 5–1 shows

a schematic image of a microcantilever. When the microcantilevers resonate, elastic stress waves are generated at the anchors and are transmitted to the substrate. A major part of these elastic waves are not reflected back to the resonator, and hence results in energy dissipation, known as anchor losses or support losses. Various models have been developed to predict the anchor losses of microcantilevers [132–134]. Assuming the support to be an infinite half-space, the anchor loss (δ_{anchor}) is related only to the geometry of the beam. The anchor loss for a microcantilever with a rectangular cross-section is directly proportional to the aspect ratios of the beam, namely w/L and h/L, where w, h, and L are width, thickness, and length of the beam, respectively, as shown in figure 5–1 [134]. The assumption of the support to be an infinite half-space is valid for nano-mechanical resonators, while for micro-mechanical resonators, the assumption of the support to be a semi-infinite plate, is reasonable. In this case, in addition to the aspect ratios of the beam, the support loss is also related to the ratio of thicknesses of the beam and the substrate i.e $h/h_{support}$, where $h_{support}$ is the thickness of the support structure. Therefore, support losses can be reduced by minimizing the ratios w/L, h/L, and $h/h_{support}$, which translates into making long, narrow and thin beams and making the beams much thinner than the support structure [134].

Dissipation also occurs by a mechanism known as slip-stick friction. This friction arises at the clamped end due to the high surface strain field at the root of the oscillating cantilever. Therefore minimizing clamping loss requires minimizing this surface strain at the clamped surface. Various configurations of cantilevered beams have been used to minimize the clamping loss (for example, read references [135–

138]). The essential feature of these designs is to remove the region of maximum strain away from the clamped surface. Therefore, clamping loss can be minimized by incorporating steps at the base of the cantilever. In case of a silicon microcantilever, this can be easily accomplished by bulk micromachining.

By operating the microcantilever in vacuum and by using a long, narrow and thin microcantilever with a step at its base, the environment-dominated and structure-dominated dissipation mechanisms can be made negligible. It is only then that, the remaining dissipation mechanisms, namely microstructure-dominated damping and thermoelastic damping become prominent. The dissipation that arises due to the motion of crystallographic defects and microstructural defects like vacancies, interstitial and substitutional defects, grain boundaries, twin boundaries, and dislocations within the microcantilever is known as internal friction. Experimental studies to evaluate internal friction as a function of frequency and temperature is known as mechanical spectroscopy [139, 140]. One strategy has come out of these studies to minimize internal friction in microcantilevers. This is to use a single-crystal of low-damping material like silicon or quartz as the microresonator.

Once all other mechanisms of damping in the microcantilever have been minimized, the one that remains is thermoelastic damping. For a vibrating microcantilever, periodic changes in stresses during vibration lead to a periodic changes in temperature. For a non-uniform stress-distribution in the vibrating structure like a microcantilever undergoing flexural vibrations, non-uniform temperature gradients and in turn heat currents arise, leading to an increase in the entropy of the system and

hence to energy dissipation [141]. This dissipation is known as the thermoelastic dissipation, and represents the minimum damping in a structure undergoing flexural vibrations. Zener has proposed a model which uses no free parameters to calculate thermoelastic damping of cantilevered beams [141]. Detailed one-dimensional [142, 143] and two-dimensional [144] models have also been proposed, which closely match the predictions obtained using Zener's model.

5.3 Microcantilever platforms for measuring internal friction

Microcantilever platforms have been widely used for measuring internal friction in deposited thin films. The microcantilever is machined out of a low-loss material (such as quartz, fused silica and single-crystal silicon). Internal friction is extracted by using two measurements: damping of the bare microcantilever, and damping after coating the structure with the thin film of interest. The first instance of the use of this approach appears in 1963 in a work by Weiss and Smith, where the authors used a micrometer-thick quartz ribbon in a clamped-free configuration as the measurement platform [145]. The measurements were performed in vacuum, and the cantilevered quartz ribbon was set into flexural vibration by a mechanical striker. The decay of the vibrating structure was measured using light reflected from the cantilever onto a photocell. This study demonstrated the presence of a Snoek relaxation peak in a 500 nm thin bcc iron film deposited on one side of the ribbon.

In 1975 Berry and Pritchet improved this method to what is currently known as the 'vibrating reed technique', and established a methodology for measuring internal friction in thin films. Specifically, they used a layer-by-layer partitioning of the dissipated energy to extract internal friction from the measurements of damping

of the bare and composite microcantilever [146]. The apparatus used by Berry and Pritchet consisted of a clamped-free beam made of a low damping material. Electrostatic interactions were used both for actuation and detection. Berry and Pritchet used this approach to study internal friction in thin films of copper-nickel, niobium, metallic glasses, and aluminium [147]. In subsequent efforts, this technique was extended to dielectric films as well as to study internal friction using both flexural and torsional vibrations [148]. The resolution was improved so that internal friction could be measured in a single monolayer of polymers [149]. The last two decades has seen increasing use of the vibrating reed technique to investigate internal friction in a wide range of thin film materials (see, for example, references [150–153]).

In general, all these versions of microcantilevers suffer from the problem of calibration. The layer-by-layer approach for partitioning dissipation makes it difficult to isolate the internal friction in the thin film. In a recent development, a solution has been found for this problem by calibrating all measurements against thermoelastic damping. The details of this approach are contained in the doctoral dissertation of G. Sosale [154], and are summarized below.

The total damping in the cantilever can be expressed as a sum of the dissipations from individual mechanisms. Therefore, in terms of logarithmic decrement,

$$\delta_s = \delta_{viscous} + \delta_{anchor} + \delta_{clamping} + \delta_{s,IF} + \delta_{s,TED}, \tag{5.2}$$

where δ_s, $\delta_{viscous}$, δ_{anchor}, $\delta_{clamping}$, $\delta_{s,IF}$, and $\delta_{s,TED}$ represent total damping, viscous losses, anchor losses, clamping losses, internal friction, and thermoelastic damping, respectively in the monolithic microcantilever (also called substrate). For a long,

narrow and thin single-crystal silicon microcantilever with a step at the base, and operating it in a low pressure or vacuum environment, it is possible to reduce the combined contribution of the viscous losses, anchor losses, support losses and internal friction to less than 10^{-5}. Hence, equation 5.2 reduces to

$$\delta_s = \delta_{s,TED} + O\left(10^{-5}\right). \tag{5.3}$$

This silicon microcantilever can now be used as a platform to measure internal friction in thin films. This is achieved by implementing the following steps:

- Microfabricate single-crystal silicon cantilevers with low aspect ratios (i.e. low w/L and $h/h_{support}$ ratios).
- Operate the microcantilever in vacuum, measure δ_s and verify if it follows equation 5.3.
- If the monolithic microcantilever follows equation 5.3, apply the nanomaterial on the microcantilever, ensuring that the adhesion between nanomaterial and the microcantilever surface is strong.
- Operate the composite microcantilever in vacuum, measure the logarithmic decrement of the composite, δ_c.
- The internal friction in the film is obtained from δ_s and δ_c as:

$$\delta_f = (\delta_c - \delta_s)\left[\frac{E_s h_s}{3E_f h_f}\right], \tag{5.4}$$

where E refers to elastic modulus and h refers to thickness. The subscripts 's' and 'f' refer to the substrate and to the film, respectively.

This method provides an accurate and highly repeatable measurement of internal friction in thin films deposited on the silicon microcantilever [8]. More recently, this technique has also been used to study the effect of selective metallization along the length of the cantilever. This study established the link between the mode shape, strain energy, and damping in the thin film. For example, placing the metal on a small region (say, 20 % of the length of the microcantilever) can lead to dramatically different structural damping depending on the location of the metallic patch. If this patch is at the tip of the microcantilever, there is no significant increase in damping. In contrast, the damping increases considerably when the same patch is located near the root of the microcantilever. This observation motivated a strategy for extending the microcantilever platform to measure internal friction in nanowires.

The next section develops a model for analyzing the effect of nanowire geometry on damping of the composite microcantilever. This model is used to extract the values of internal friction from the raw data which involves contributions from both the substrate and the deposited nanostructures.

5.4 A model to extract internal friction of nanowires

Let us consider a thin slender cantilever attached to a large base, as shown in figure 5–2. The cantilever has a rectangular cross-section with length L, width w, and thickness h_s. This cantilever acts as the substrate on which an array of N nanowires is patterned along the length of the beam, over an area comprising $\sim$20 % of the length from the root of the cantilever. Each nanowire has a uniform thickness h_f, width w_f, and length $0.2L$. The thickness of the nanowire is much less compared to the thickness and the width of the substrate, and the width of each nanowire is much

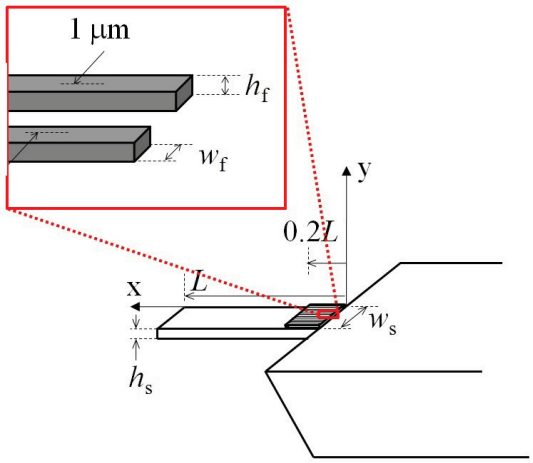

Figure 5–2: Schematic illustration of a microcantilever of length L, with an array of nanowires at the root of the cantilever. The inset shows two adjacent nanowires with centre-to-centre distance of 1 μm.

smaller compared to that of the substrate. The centre-to-centre distance between two adjacent nanowires is always maintained at 1 μm.

The nanowire assembly can be modelled as a patterned thin film. This bilayer composite structure is assumed to be an Euler-Bernoulli beam executing flexural vibration with small amplitude. Similar to the case of a thin film on a thick substrate, since $h_f \ll h_s$, addition of the nanowire assembly does not affect the mode shapes, natural frequencies, and location of the neutral axis of the substrate cantilever [146,155]. The damping in a given mode of flexural vibration can be evaluated by measuring logarithmic decrement (δ) under free-decay, and is given by:

$$\delta = \frac{\Delta W}{2W_{max}}, \tag{5.5}$$

where W_{max} is the maximum strain energy stored in the composite. The total damping in the composite cantilever δ_c can be expressed in terms of damping in the

substrate and that in the nanowire assembly. Hence,

$$\delta_c = \frac{\Delta W_c}{2W_{c,max}} = \frac{\Delta W_s + \Delta W_f}{2W_{c,max}}. \tag{5.6}$$

In this expression, ΔW_c, ΔW_s, and ΔW_f represent the energy dissipated for every cycle of vibration in the composite, substrate and the nanowire assembly, respectively. $W_{c,max}$ is the maximum strain energy stored in the composite structure. Since $h_f \ll h_s$, the contribution of the nanowire assembly to the maximum strain energy stored in the composite beam is negligible, hence $W_{c,max} \approx W_{s,max}$. Therefore,

$$\delta_c \approx \frac{\Delta W_s + \Delta W_f}{2W_{s,max}} = \frac{\Delta W_s}{2W_{s,max}} + \left(\frac{W_{f,max}}{W_{s,max}}\right)\frac{\Delta W_f}{2W_{f,max}} = \delta_s + \left(\frac{W_{f,max}}{W_{s,max}}\right)\delta_f, \tag{5.7}$$

where δ_c, δ_s, and δ_f are logarithmic decrement of the composite, substrate and the nanowire assembly, respectively. $W_{f,max}$ and $W_{s,max}$ are the maximum strain energy stored in the nanowire assembly and in the substrate, respectively. The term in the parenthesis is the ratio of the maximum elastic strain energy stored in the nanowire assembly and the substrate. From equation 5.7, the internal friction in the nanowire assembly can be calculated using

$$\delta_f = (\delta_c - \delta_s)\left(\frac{W_{s,max}}{W_{f,max}}\right). \tag{5.8}$$

This requires experimental measurement of δ_c and δ_s and numerical evaluation of $W_{f,max}$ and $W_{s,max}$. We evaluate the maximum elastic strain energy of the substrate and the film using a standard analysis of the quasi-static deformation of an Euler-Bernoulli beam. For an Euler-Bernoulli beam of length L, width w_s and thickness

h_s, the maximum strain energy for the substrate can be evaluated by [156]:

$$W_{s,max} = \frac{1}{2}\int_0^L E_s I_s \left(\frac{d^2 y_1}{dx^2}\right)^2 dx, \tag{5.9}$$

where E_s is the elastic modulus of the substrate, I_s is the area moment of inertia of the substrate, and $y_1(x)$ is the mode shape for the first mode of flexural vibration. Here $I_s = \frac{w_s h_s^3}{12}$, and

$$y_1(x) = sin(\lambda_1 x) - sinh(\lambda_1 x) + \frac{sin(\lambda_1 L) + sinh(\lambda_1 L)}{cos(\lambda_1 L) + cosh(\lambda_1 L)}\left[cosh(\lambda_1 x) - cos(\lambda_1 x)\right], \tag{5.10}$$

with $\lambda_1 L = 1.875104$. For a beam with an array of N nanowires along the length of the beam, patterned over an area comprising ~20 % of the length from the root of the cantilever, the maximum strain energy in the nanowire assembly is given by:

$$W_{f,max} = \frac{1}{2}\int_0^{0.2L} E_f N \left\{ I_f + w_f h_f \left(\frac{h_s + h_f}{2}\right)^2 \right\} \left(\frac{d^2 y_1}{dx^2}\right)^2 dx, \tag{5.11}$$

where the terms within the square brackets represent the moment of inertia of the nanowire assembly about the neutral axis of the cantilever, with $I_f = \frac{w_f h_f^3}{12}$. The number of nanowires N is related to the width of the substrate w_s and to the centre-to-centre spacing between adjacent nanowires (s) by $N = \frac{w_s}{s}$. Since $h_f \ll h_s$, we can neglect h_f^2 and higher order terms of h_f.Therefore,

$$W_{f,max} = \frac{1}{2}\frac{E_f N w_f h_f h_s^2}{4}\int_0^{0.2L} \left(\frac{d^2 y_1}{dx^2}\right)^2 dx. \tag{5.12}$$

Combining equations 5.8, 5.9 and 5.12 we obtain

$$\delta_f = (\delta_c - \delta_s) \left[\frac{E_s h_s}{3E_f h_f} \frac{w_s}{N w_f} \frac{\int_0^L \left(\frac{d^2 y_1}{dx^2} \right)^2 dx}{\int_0^{0.2L} \left(\frac{d^2 y_1}{dx^2} \right)^2 dx} \right]. \tag{5.13}$$

In the limit of a thin film spanning the entire width of the cantilever, this equation reduces to

$$\delta_f = (\delta_c - \delta_s) \left[\frac{E_s h_s}{3E_f h_f} \right], \tag{5.14}$$

which is the same expression derived by Berry and Pritchet [146]. This serves as a useful check on our derivation. Equations 5.13 has been used in this work to extract internal friction values of the nanostructures from that of the measured composite logarithmic decrement.

5.5 Experimental procedure

5.5.1 Fabrication

Fabrication of microcantilevers

The silicon microcantilevers were micromachined from double-side polished, (100)-oriented commercial grade silicon on insulator (SOI) wafers with 7.5–15 μm device layers, 600 nm buried oxide (BOX) layer, and 520–530 μm handle layer. The as-received wafers were subjected to solvent cleaning in acetone, isopropanol (IPA), and deionized water in order to remove any organic residues. The wafers were dried and 500 nm of silicon oxide was grown on both surfaces of the wafer at 1100 °C using a wet chemical vapour deposition (CVD) process. This CVD process involved subjecting the heated wafer for ∼26 minutes to a mixed gas-flow with hydrogen flow-rate of 3000 sccm, and oxygen flow-rate of 1750 sccm, in an oxidation furnace (Tylan).

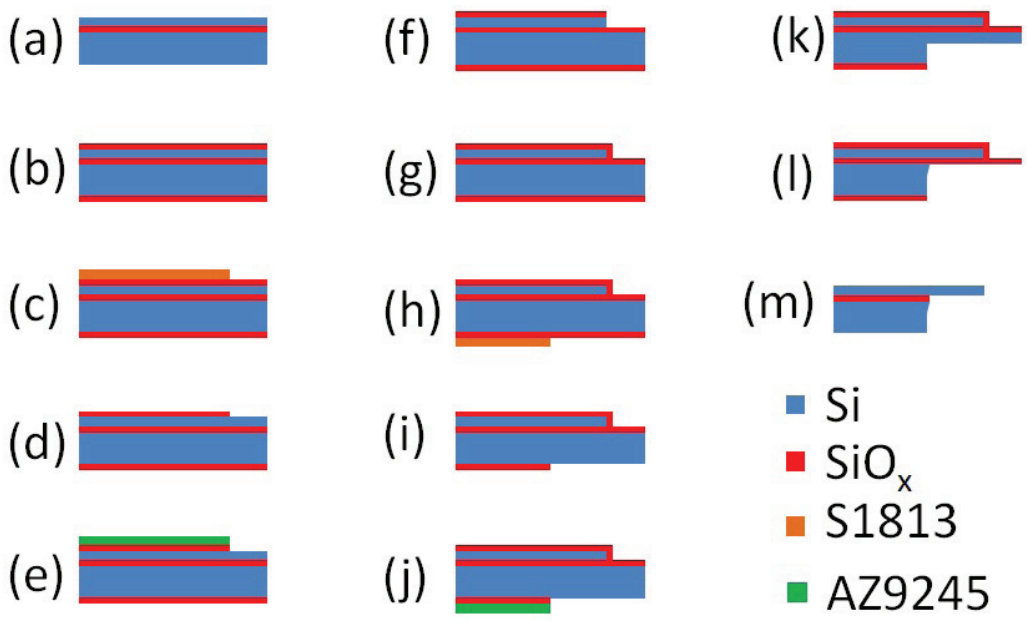

Figure 5–3: Process flow for fabrication of silicon microcantilevers: (a) solvent clean, (b) growth of 500 nm of oxide, (c) photolithography of S1813 photoresist on the device-layer, (d) dry etching of the oxide, (e) photolithography of AZ9245 photoresist, (f) DRIE of the device-layer Si, (g) growth of 100 nm of oxide, (h) photolithography of S1813 photoresist on the handle-layer, (i) dry etching of the oxide on the device-layer, (j) photolithography of AZ9245 photoresist, (k) DRIE of handle-layer Si, (l) wet etching of remaining handle-layer Si in 27 % TMAH, and (m) oxide strip in 49 % HF.

The oxide film on the top surface of the wafer was patterned using a standard photolithographic process. This photolithographic process consisted of spin-coating 1.4 μm of a positive photoresist S1813 (Microposit), baking the resist-coated wafer at 115 °C for 60 seconds, and exposing the resist-coated wafer with the top mask in the soft-contact mode, using an exposure dose of 70 mJ/cm^2. The exposure was performed using EVG620 photomask aligner (EV Group). The exposed wafer was then developed in MF-319 developer (Microposit), rinsed in deionized water and blow-dried. The wafer was hard-baked on a hot-plate at 90 °C for 90 seconds. The patterned photoresist layer acted as a mask for the dry-etching of the exposed oxide, performed using a gas plasma with CHF_3, Ar, CF_4 flow of 45 scc, 70 scc, and 7 scc respectively at 100 mTorr pressure for 100 seconds. The remaining resist layer was removed using oxygen plasma. The flow of oxygen was maintained at 45 scc for 300 seconds at a pressure of 150 mTorr. The dry etching and oxygen plasma clean were performed in Applied Materials P5000 Reactive Ion Etcher (RIE).

The wafer with patterned oxide layer on the top surface was then coated with a monolayer of hexamethyldisilzane (HMDS) at 115 °C using YES HMDS oven to improve photoresist adhesion, a critical factor in the subsequent deep reactive ion etching (DRIE) step. 10 μm of a positive photoresist AZ9245 (AZ Electronic Materials) was spin-coated on the top-side of the wafer, followed by soft-bake at 115 °C for 150 seconds. This was followed by exposing the resist-coated top surface of the wafer using the same top mask as was used before. Four exposure cycles, with an exposure dose of 250 mJ/cm^2 for each cycle were used. The development of the exposed wafer was performed in a solution containing four parts of deionized water

and one part of AZ400 developer (AZ Electronic Materials). The wafer was then blow-dried and post-baked at 115 °C for 150 seconds. The composite pattern consisting of the patterned oxide and the protective photoresist layers, acted as a hard mask during the subsequent deep reactive ion etching (DRIE) of silicon using Tegal SDE110 deep reactive ion etcher. The exposed silicon of the device layer was etched using gases consisting of C_4F_8, oxygen, and SF_6 with pulsed flows of 300 sccm, 200 sccm, and 700 sccm, respectively. The source-power was maintained at 2700 W, and the distance of the wafer from the source was maintained at 170 mm. This defined the geometry of the top-part of the cantilever. The remaining resist was removed using the oxygen plasma.

The wafer was again oxidized to grow ∼100 nm of silicon oxide so as to protect the side-walls of the etched silicon structures. The microfabrication steps related to patterning of the oxide using a bottom mask, and to the DRIE steps were repeated for the back surface of the wafer. The etch rate across the wafer during the DRIE process was non-uniform. Hence, DRIE was followed by a short tetramethyl ammonium hydroxide (TMAH) etch to release the beams, and a final hydrofluoric acid (HF) dip to strip the oxide from all surfaces of the micromachined cantilevers. This resulted in a series of cantilevers with lengths in the range of 700–1625 μm, widths in the range of 300–315 μm, and thicknesses being the same as that of the thicknesses of the device layers. Figure 5–4 shows a scanning electron microscope image of one of the micromachined silicon cantilevers. The natural frequencies of flexural vibrations of these beams range from 6.5 kHz to 24.5 kHz in the first mode.

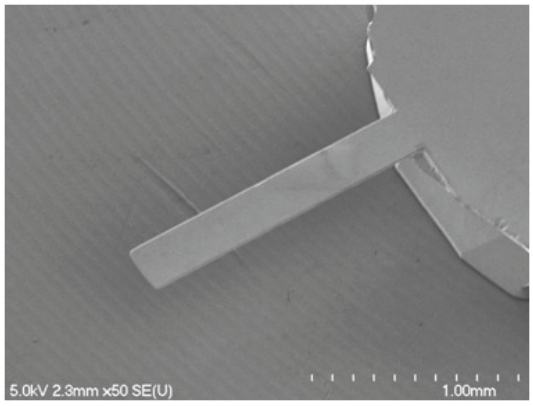

Figure 5–4: : Scanning electron microscope image of a micromachined silicon cantilever. This cantilever is 1622 μm long, 300 μm wide, 12.7 μm thick, and has a natural frequency of 6.5 kHz.

Fabrication of nanostructures on microcantilevers

Integration of metallic patterns and nanostructures was achieved on these fragile microcantilevers by employing spray-coating of electron beam resists, followed by electron beam lithography to define polymer structures, and a lift-off process. The spray-coating of electron beam resists was performed using a commercial spraycoater (EVG101, EVGroup). The dispense rate, the nozzle pressure, and the ultrasonic power were maintained at 5 μl/sec, 1000 mbar and 1.4 W, respectively. The spray-coating parameters were optimized for a 4 inch wafer, with the spray-coating being performed from edge-to-edge of the wafer. The number of cycles was varied to achieve the required thickness with minimum surface roughness. The stage was also rotated at 80 rpm, with the direction of rotation (clockwise/anticlockwise) changing at the end of every cycle. The microcantilevers were first spray-coated with a copolymer, MMA-MAA EL11 (Microchem, Inc.). The resist was diluted with MIBK so that the weight ratio of ethyl lactate (EL) to MIBK was 1:1.7, and 5 cycles of spray-coating led

to deposition of 390±37 nm of the resist on the microcantilever. The coated cantilever was baked at 150 °C for 90 seconds. This was followed by spray-coating 20 cycles of PMMA A2, which led to deposition of 203±33 nm of the resist. The coated cantilever was again baked at 180 °C for 90 seconds. The bilayer-resist-coated microcantilevers were patterned using electron beam lithography with an electron beam operating at 30 kV, with beam current of 357 pA and electron doses in the range of 6–8 nC/cm. The patterns were developed at room temperature by immersing the structures for two minutes in a solution that contained MIBK and isopropyl alcohol (IPA) in a ratio of 1:3 by volume. Finally, the specimens were soaked in IPA for 30 seconds, rinsed in deionised (DI) water and then permitted to dry in air. Thin films of aluminium with thicknesses of 50 nm and 100 nm were then deposited on the microcantilevers using BJD1800 electron beam evaporator (Temescal) using an operating voltage of 9 kV, emission current of ∼300 mA, and a background vacuum of 2×10^{-6} Torr. The deposition rate of Al was 0.2 nm/s. For lift-off, a resist-stripper Remover PG (Microchem Inc.) was heated at 60 °C and the microcantilever was soaked in the heated resist-stripper for 15 minutes. The patterned microcantilevers were rinsed in acetone, IPA and deionized water, and dried in air. Care was taken so that no water-marks were left on the microcantilever after drying. The beams were thus patterned with an array of nanowires parallel to and along the length of the beam. The nanowires patterned over an area comprising ∼20 % of the length from the base.

5.5.2 Microstructural characterization

The linewidth of the nanowires were measured from images obtained using scanning electron microscope (Hitachi FEGSEM S4700). Figure 5–5 shows a scanning

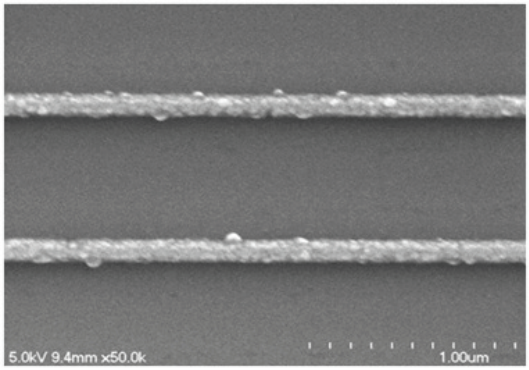

Figure 5–5: Scanning electron micrograph of 100 nm thick and ∼134 nm wide aluminium nanowires, with centre-to-centre spacing of 1 μm.

electron microscope image of the patterned aluminium nanonowires. Grain-size of the aluminium films and patterned nanowires were obtained from images using transmission electron microscope (Phillips CM200) using an operating voltage of 200 kV. For transmission electron microscopy, 100 nm thick silicon nitride membranes were coated with aluminium films with thicknesses of 50 nm and 100 nm. Figure 5–6(a) and figure 5–6(b) show the transmission electron micrographs of the microstructure of the 50 nm thick and 100 nm thick aluminium thin films, respectively. There exists a broad distribution in grain-size for the evaporated thin films. For the 50 nm thick aluminium film, the grain-sizes range from 18 nm to 72 nm, with an average grain-size of 42±13 nm, while for the 100 nm thick aluminium film the grain-sizes range from 17 nm to 137 nm, with an average grain-size of 72±26 nm.

Aluminium nanowires were also patterned on the silicon nitride membranes using the procedure described in the previous section. The patterned nanowires also exhibit microstructures similar to that of the thin films. Figure 5–7 shows a transmission electron microscope image of a 50 nm thick and 380 nm wide aluminium

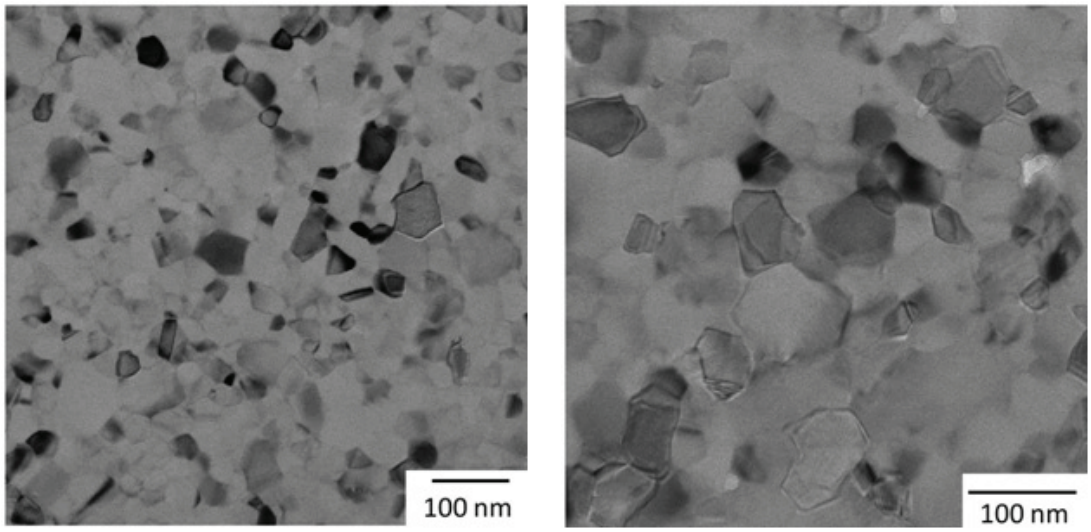

(a) (b)

Figure 5–6: Transmission electron microscope images of (a) 50 nm thick aluminium film with average grain-size of 42 nm, and (b) a 100 nm thick aluminium film with average grain-size of 72 nm.

nanowire patterned on a 100 nm thick silicon nitride membrane window. The average grain-size in the nanowire is 41±14 nm. Intrinsic growth-related residual stress of the aluminium films was measured using wafer curvature tests (Flexus 5200, KLA-Tencor). The residual stress in the 50 nm thick aluminium film was found to be -19 MPa, while that in the 100 nm thick aluminium film was -42 MPa.

5.5.3 Measurement of damping

The damping in monolithic silicon and aluminium-patterned silicon beams at room temperature was measured using the free-decay technique. Figure 5–8 shows a schematic of the damping measurement system. It primarily consisted of a cantilever securely clamped in a large, precisely machined base made of stainless steel. The clamp and cantilever assembly was mounted onto a piezoelectric shaker (NanoOP65,

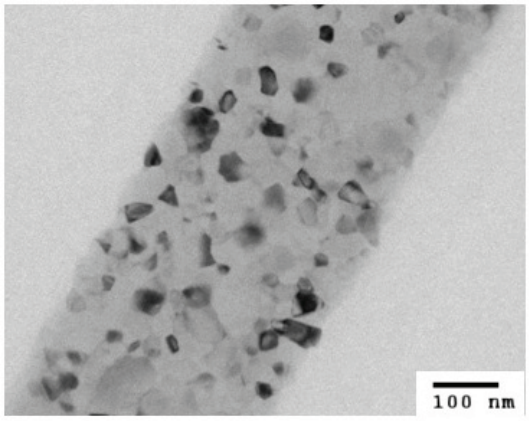

Figure 5–7: Transmission electron microscope images of 50 nm thick and 380 nm wide aluminium nanowire patterned on a 100 nm thick silicon nitride membrane. The average grain-size is 41 nm.

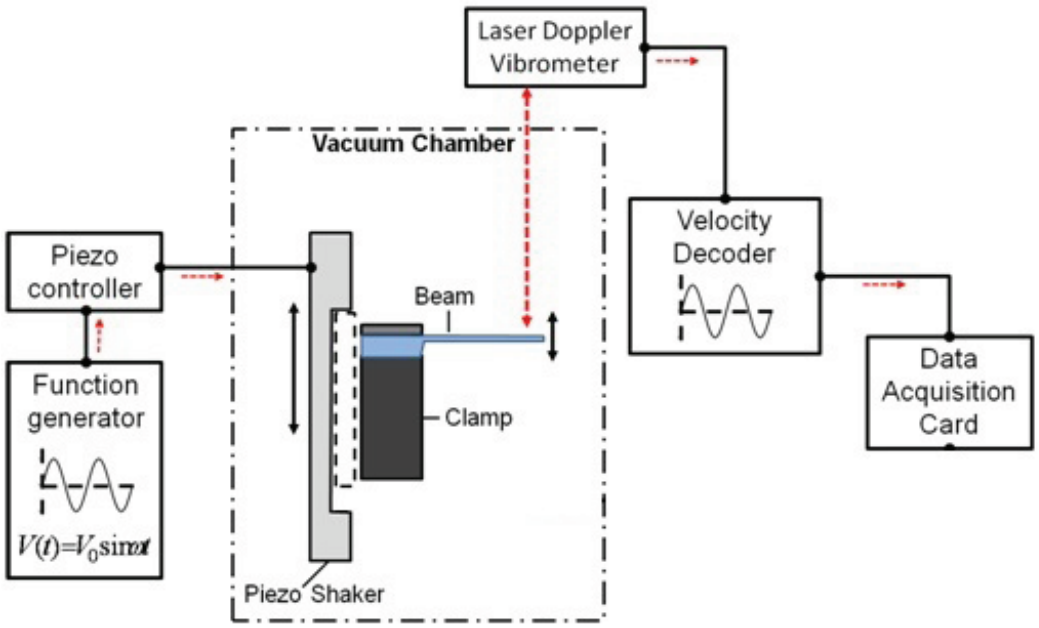

Figure 5–8: Schematic of components of the complete damping measurement system. The red dashed arrows indicate the flow of signal information [154].

Mad City labs Inc, WI, USA) and the whole assembly was put inside a vacuum chamber. The piezoelectric shaker was driven in open circuit by a function generator with an applied sinusoidal signal with peak-to-peak amplitude of 20 mV, and the dynamics of the beam was measured by a laser Doppler vibrometer (LDV) (OFV 5000, Polytec Inc., CA, USA) at pressures less than 10^{-4} mbar. The LDV had a sensitivity of 5 mm/sec/V. The spot-size of the laser beam was 40 μm at a distance of 30 cm. The cantilevers were first excited at a frequency close to but less than the first resonance frequency. The exciting signal was then terminated, and the free-decay of the beam was recorded using a data acquisition card. The sampling rate was maintained at values greater than at least ten times the measured natural frequency for the first mode. Processing of the recorded free-decay signal of the monolithic silicon cantilevers and the patterned cantilevers in MATLAB led to evaluation of the logarithmic decrement of the monolithic silicon cantilevers (δ_s), and the logarithmic decrement of the patterned composite cantilevers (δ_c), respectively. Details of instrumentation and signal-processing are available in reference [154]. For each specimen, at least three measurements were performed, and the mean values are reported, along with their associated standard deviation.

5.6 Results

Table 5–1 lists the measured logarithmic decrement at various frequencies for silicon cantilevers before and after they are coated with arrays of nanowires of length $0.2L$, aligned along the length the cantilever. Also listed in these tables are predicted values of thermoelastic damping of the uncoated silicon cantilevers. The

Table 5–1: Comparison of damping in silicon microcantilevers before and after patterning metallic nanowires with centre-to-centre spacing of 1 μm. The patterns were made over an area covering 20% of the length from the root of the cantilever. The mean width of the nanowires lies in the range of 110–396 nm. Two different thicknesses of the nanowires, 50 nm and 100 nm are considered. f denotes the resonant frequency of the cantilevers. h_f and w_f are the thickness and width of the nanowires. $\delta_{s,TED}$ is the thermoelastic damping of the monolithic silicon cantilever obtained from theory [141], while δ_s is the measured logarithmic decrement of the monolithic silicon cantilever. δ_c is the logarithmic decrement of the composite microcantilever. δ_f here represents internal friction in the array of nanowires.

f (Hz)	h_f (nm)	w_f (nm)	$\delta_{s,TED} \times 10^6$	$\delta_s \times 10^5$	$\delta_c \times 10^5$	δ_f
10622	100	118±13	3.53	1.02±0.09	4.89±0.11	0.035±0.001
21048	100	134±8	6.99	1.91±0.01	5.47±0.23	0.026±0.002
12444	50	396±8	4.13	1.19±0.15	5.97±0.05	0.026±0.001
6523	50	110±5	4.84	0.92±0.02	1.90±0.04	0.029±0.001

thermoelastic damping ($\delta_{s,TED}$) in the silicon beams were calculated using Zener's equation [141]:

$$\delta_{s,TED} = \frac{\pi E_s {\alpha_s}^2 T_0}{C_s} \frac{\Omega}{1+\Omega^2};\ \Omega = \omega \frac{C_s {h_s}^2}{\pi^2 k_s} \tag{5.15}$$

where α_s is the coefficient of linear expansion, T_0 is the equilibrium temperature of the beam, C_s is the specific heat per unit volume, ω is the angular frequency (in radians per second), k_s is the thermal conductivity, and Ω is the normalized frequency such that thermoelastic damping attains its maximum value at $\Omega = 1$. In this work, thermoelastic damping was evaluated at $T_0 = 300$ K, using well-known values of material parameters for (100)-oriented single-crystal silicon, viz: $E_s = 169$ GPa, $\alpha_s = 2.6 \times 10^6$ K^{-1}, $C_s = 2.6 \times 10^6$ J/m^3/K, and $k_s = 149$ W/m/K. The measured values of logarithmic decrement of the silicon cantilevers were close to the predicted thermoelastic damping for these beams. Logarithmic decrement for uncoated silicon cantilevers measured in this study was less than 1.9×10^{-5}, and the residual damping (i.e. the difference between the measured thermoelastic damping and the measured logarithmic decrement) was less than 1.2×10^{-5}. For the nanowires of similar width (in the range of 110–134 nm), the damping in the composite cantilevers with 100 nm thick nanowires was found to be significantly greater than that with 50 nm thick nanowires. In addition, the internal friction of arrays of aluminium nanowires did not show significant dependence on frequency in the range of 6.5 kHz to 21 kHz.

Equation 5.13 has been used to extract the value of internal friction in the array of nanowires. The internal friction of the nanowire assembly lies in the range of 0.026–0.035 for the given frequency range. The standard deviation associated with the

values of internal friction was evaluated with the assumption that the uncertainties in the measurement of δ_s and δ_c solely contribute to the uncertainties in δ_f according to the following equation:

$$\sigma_f = \sqrt{{\sigma_s}^2 + {\sigma_c}^2} \left[\frac{E_s h_s}{3 E_f h_f} \frac{w_s}{N w_f} \frac{\int_0^L \left(\frac{d^2 y_1}{dx^2} \right)^2 dx}{\int_0^{0.2L} \left(\frac{d^2 y_1}{dx^2} \right)^2 dx} \right], \tag{5.16}$$

where σ_f, σ_s, and σ_c are the standard deviations associated with δ_f, δ_s, and δ_c respectively.

In order to compare the internal friction of the nanowires with those of film of similar thicknesses, internal friction of aluminium thin films with thicknesses of 50 nm and 100 nm were measured in the frequency range of 7.5–24.5 kHz. Table 5–2 summarizes the results of measurement of logarithmic decrement and the evaluation of internal friction in thin films. Equation 5.4 was used to evaluate the internal friction of aluminium films. The standard deviation in the values of δ_f for the thin films were also evaluated using an approach similar to one used for evaluating equation 5.16. The damping of the composite microresonators are found to increase proportionately with increasing thickness. For example, consider the the values of δ_c at 12234 Hz and 12236 Hz. The thickness of aluminium film for the case at 12234 Hz is twice that at 12236 Hz. The total damping in the composite microresonator with a natural frequency of 12234 Hz is almost twice the composite microresonator with a natural frequency of 12236 Hz. In addition, the internal friction of aluminium thin films did not exhibit significant frequency dependence over the frequency range of 7.5 kHz to 24.5 kHz.

Table 5–2: Comparison of damping in silicon microcantilevers before and after coating with thin film of aluminium. Two different thicknesses of the thin film, 50 nm and 100 nm are considered. h_f and w_f are the thickness and width of the nanowires. $\delta_{s,TED}$ is the thermoelastic damping of the monolithic silicon cantilever obtained from theory [141], while δ_s is the measured logarithmic decrement of the monolithic silicon cantilever. δ_c is the logarithmic decrement of the composite microcantilever. δ_f here represents internal friction in the array of nanowires.

f (Hz)	h_f (nm)	$\delta_{s,TED} \times 10^6$ (nm)	$\delta_s \times 10^5$	$\delta_c \times 10^5$	δ_f
12234	100	4.07	1.15±0.04	54.60±1.57	0.035±0.001
24536	100	8.15	1.76±0.01	43.60±3.19	0.027±0.002
7535	50	8.11	1.04±0.04	15.80±0.24	0.034±0.001
12236	50	4.07	1.14±0.13	29.50±2.34	0.037±0.003

A comparison of internal friction in aluminium thin films and nanowires does not reveal any significant size effects on dissipation at room temperature. The transmission electron microscope image, as shown in figure 5–7 confirms that the nanowire is polycrystalline and that the grain-size and the distribution of grain-sizes in the nanowire is similar to that of a thin film of the same thickness, and hence supports the experimental observation of similar internal friction values for both nanowires and thin films.

5.7 Discussions

There are four broad mechanisms by which aluminium nanowires and thin films on a microcantilever dissipate energy. The first mechanism of energy dissipation is the thermoelastic damping. The contribution of thermoelastic damping in aluminium

thin film on a silicon microcantilever has been calculated, and is found to be negligible compared to the total energy dissipated, and hence can be safely neglected [8]. The second source of dissipation is sliding at the aluminium/silicon interface, while the third source of dissipation is irreversible motion of surface defects. It has been noted in this study that the overall damping of a composite microcantilever increases proportionately as the thickness of aluminium thin film or aluminium nanowires increases. Similar thickness dependence of damping of microcantilevers coated with metallic thin film has been noted in an earlier study for aluminium, gold and silver thin films [8]. If interfacial sliding or dissipation due to surface defects were dominant, then damping in composite microcantilevers would not be dependent on the thickness of the nanostructures. Hence, the second and the third sources of damping in the aluminium thin film and nanowires can be ruled out. The fourth source of damping is irreversible motion of crystallographic and microstructural defects within the aluminium thin film and nanowires. By a process of elimination, it is concluded that dissipation in aluminium thin films and nanowires is dominated by the motion of crystallographic defects in the nanomaterials.

Crystallographic defects in polycrystalline thin films and nanowires can be of several types, such as vacancies, dislocations, grain boundaries and voids. A survey of literature on internal friction of thin aluminium films suggest that there exists a relationship between grain boundaries and dissipation, especially at low temperatures. Previous studies measured internal friction of aluminium thin films as a function of temperature [147, 151]. These studies showed that there exists a low temperature relaxation peak [147]. The origin of this low temperature relaxation peak was found

to be in grain boundaries [151]. Moreover, a recent study of internal friction of annealed aluminium thin films has demonstrated that the magnitude of internal friction at room temperature depends on grain size [157]. Thus, it is plausible that grain boundary sliding is a dominant mechanism in aluminium thin films. As noted before, from the microstructural characterization, aluminium nanowires exhibit similar grain-size distribution as that of thin films with same thickness. Therefore, similarity in the values of internal friction of the aluminium nanowire assembly and of the aluminium thin film is consistent with grain boundary sliding being the dominant dissipation mechanism in aluminium nanowires at room temperature. However, it is important to note that the average grain size of the nanowires was significantly less than the width of the nanowires measured in this study. Expectations based on the mechanism of grain-boundary sliding suggest that significant size effects will appear in nanowires with grain sizes comparable to width.

5.8 Summary

This chapter presented the first calibrated measurement of internal friction in aluminium nanowires. At the heart of this measurement are two methods: (i) the use of a silicon microcantilever-based measurement technique which can accurately evaluate internal friction by minimizing support and viscous losses and by calibrating damping of the substrate with respect to thermoelastic damping limit, and (ii) the ability to integrate metallic nanowires on fragile micromachined cantilevers using a recipe which combines spray-coating, electron beam lithography, physical vapour deposition and lift-off processes. The internal friction of aluminium nanowires with widths in the range of 110–396 nm, and thicknesses in the range of 50–100 nm, are

in the range of 0.026–0.035 within the frequency range of 6.5–21 kHz. These values match very closely the internal friction values obtained for thin films of aluminium within the frequency range of 7.5–24.5 kHz. These results show that internal friction in aluminium nanowires exhibit no dramatic size effect. Therefore, measurements of internal friction of thin aluminium films can be used to predict the damping of a composite microcantilever with aluminium nanowires of the same thickness, and aligned along the length of the cantilever.

CHAPTER 6
Characterization of carbon nanotube/titanium nitride porous nanocomposite films

6.1 Introduction

The emergence of new classes of nanomaterials coupled with novel routes for synthesis and microfabrication can lead to materials with new architectures at micrometer and nanometer length scales. Establishing process-structure-property relationships for this class of nanomaterials is useful because such relationships can help microsystems designers to evaluate the utility and applications of these materials. This chapter explores one such material, namely, a porous ceramic nanocomposite. This ceramic nanocomposite consists of a dense forest of tangled multi-walled carbon nanotubes (MWNTs) sheathed by a continuous layer of titanium nitride (TiN). A schematic of the nanocomposite is shown in figure 6–1.

Figure 6–1: Schematic image of carbon nanotube/titanium nitride nanocomposite. The nanotubes are represented by the black curves, and TiN coatings are represented in yellow [158].

The guiding objective behind having an open structure of carbon nanotubes (CNTs) is to have a larger surface area in order to enhance electrical, thermal and electrochemical transport. However, maintaining the mechanical integrity of such a structure is a major issue since the nanotube structure can be subject to wear under mechanical stresses, during operation. A protective layer around the CNTs can improve the integrity of such open structures. The choice of TiN as the protective material is due to its desirable properties like excellent oxidative stability, corrosion resistance and good electrical conductivity [159–161]. These properties make TiN an excellent candidate as electronic conductors in microelectronic devices and as electrodes in electrochemical devices.

Evaluation of mechanical properties of such nanocomposite structures is crucial to estimate the reliability of these nanocomposites. To this end, the response of CNT/TiN nanocomposite to indentation is presented in this chapter. The next section describes the synthesis of the CNT/TiN nanocomposite. Section 6.3 presents the concepts of nanoindentation testing. A literature review of mechanical properties of similar CNT assemblies is presented in section 6.4. Finally, the experimental procedure and results of the indentation tests are discussed.

6.2 Synthesis

The synthesis of this nanocomposite was performed by Dr. Carole Emilie Baddour of the Department of Chemical Engineering, McGill University. The essential steps are to grow a uniform layer of multi-walled carbon nanotubes on a 304 stainless steel substrate. Subsequently, the nanotube network was coated with a thin film of TiN. The details of this synthesis are briefly summarized below.

A simple process of fabricating multi-walled carbon nanotubes directly on stainless steel substrates was developed by Baddour *et al.* [158,162]. In this thermal chemical vapour deposition (CVD) process, the 304 stainless steel plates that were used as substrate to grow carbon nanotubes also acted as a catalyst and provided active sites for nanotube growth, and hence no external addition of catalyst precursors was required. The steel plates were 0.796 mm thick, 15 mm long and 15 mm wide. The stainless steel plates were cleaned with acetone in an ultrasonic bath and etched in 35-38% HCl for 5 minutes. Then, the etched steel plates were heat-treated at 850 °C for 30 minutes while maintaining a flow of N_2. Afterwards, the temperature was reduced to the synthesis temperature of 700 °C. At this point C_2H_2 was introduced for 5 minutes. A 30 minute growth period in the presence of N_2 at the synthesis temperature was then imposed before the cool down. The flow rate of N_2 (the carrier gas) and C_2H_2 (the carbon source) during the thermal CVD process was 592 ± 5 sccm and 45 ± 5 sccm, respectively. A uniform layer of CNT forms on the stainless steel substrates, as shown in figure 6–2. The CNTs are 20 - 70 nm in diameter and grow in a randomly oriented manner, creating a 'felt-like' structure. The thickness of the CNT 'felt' is estimated to be 1 - 3 μm.

The CNT layer was coated with TiN using cathodic arc deposition. This step was performed rapidly after the growth of the CNT network, allowing the individual nanotube to be coated with TiN in a way to provide a full protective layer around the tubes. The TiN forms an architectural scaffold holding the nanotube 'felt' mechanically. Initially, the vacuum chamber was pumped down to 5.0×10^{-5} Torr for

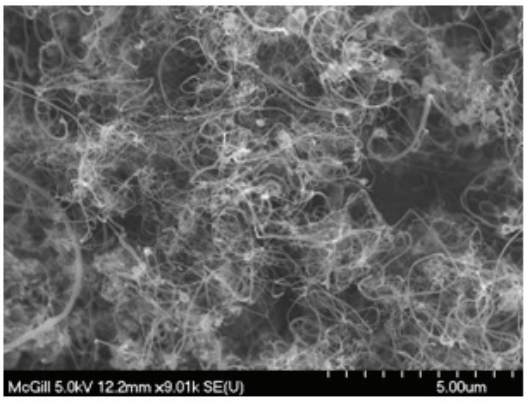

Figure 6–2: Scanning electron microscope image of a CNT 'felt' [158].

30 minutes to remove gases, dust particles and any contaminants from the chamber. During this time, the heaters were turned on to heat the chamber walls and specimens to 100 °C. Titanium was used as the cathode, while the CNT sample and the deposition chamber formed the anode. The cathode current was set at 60 A. The TiN coating was formed in the presence of nitrogen gas at a flow-rate of 123 sccm and a chamber pressure of 1.2×10^{-2} Torr. Two sets of nanocomposite samples were synthesized, one with a substrate bias voltage of -150 V and the other with a substrate bias voltage of -400 V. For each set, four deposition times (5, 15, 30 and 60 minutes) were used. During the TiN deposition process, the temperature of the deposition chamber rose to 400–450 °C. Figures 6–3 and 6–4 show the scanning electron microscope images of the CNT/TiN nanocomposites.

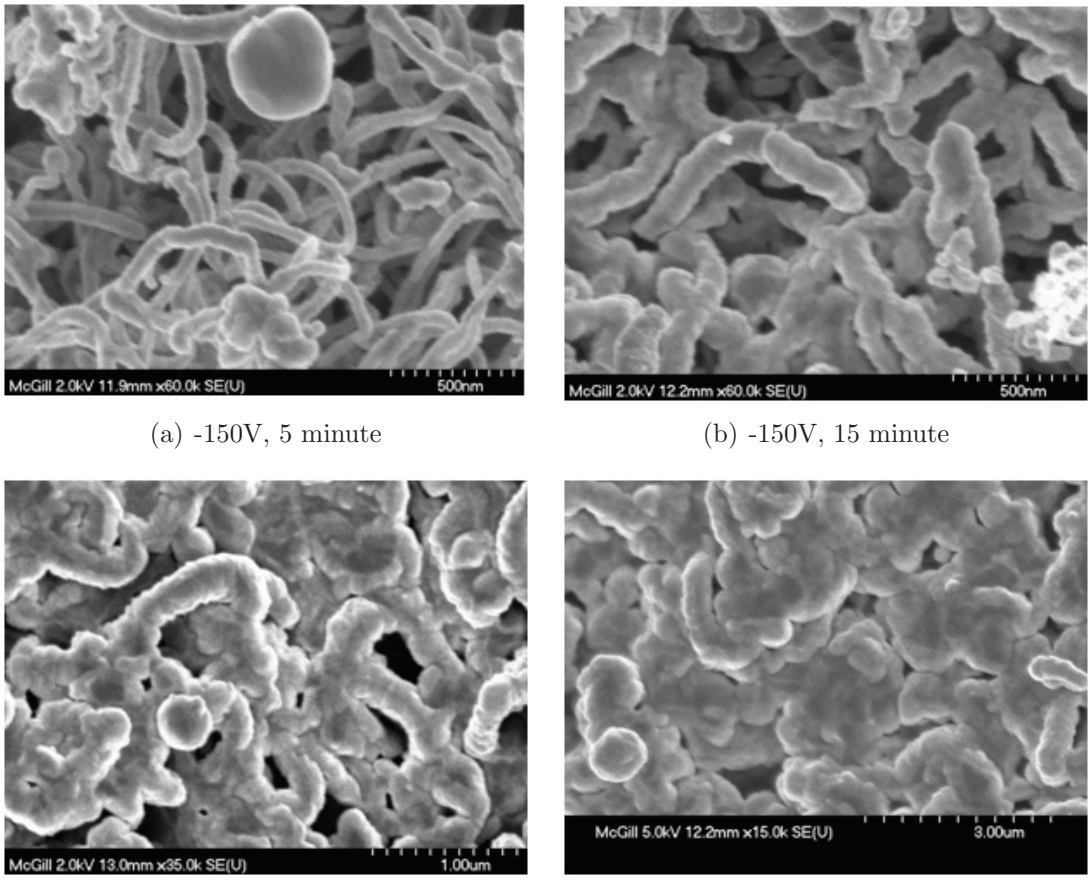

(a) -150V, 5 minute

(b) -150V, 15 minute

(c) -150V, 30 minute

(d) -150V, 60 minute

Figure 6–3: Scanning electron microscope images of CNTs coated with TiN. TiN was deposited at -150V bias and deposition times of (a) 5 min, (b) 15 min, (c) 30 min, and (d) 60 min, using cathodic arc deposition [158].

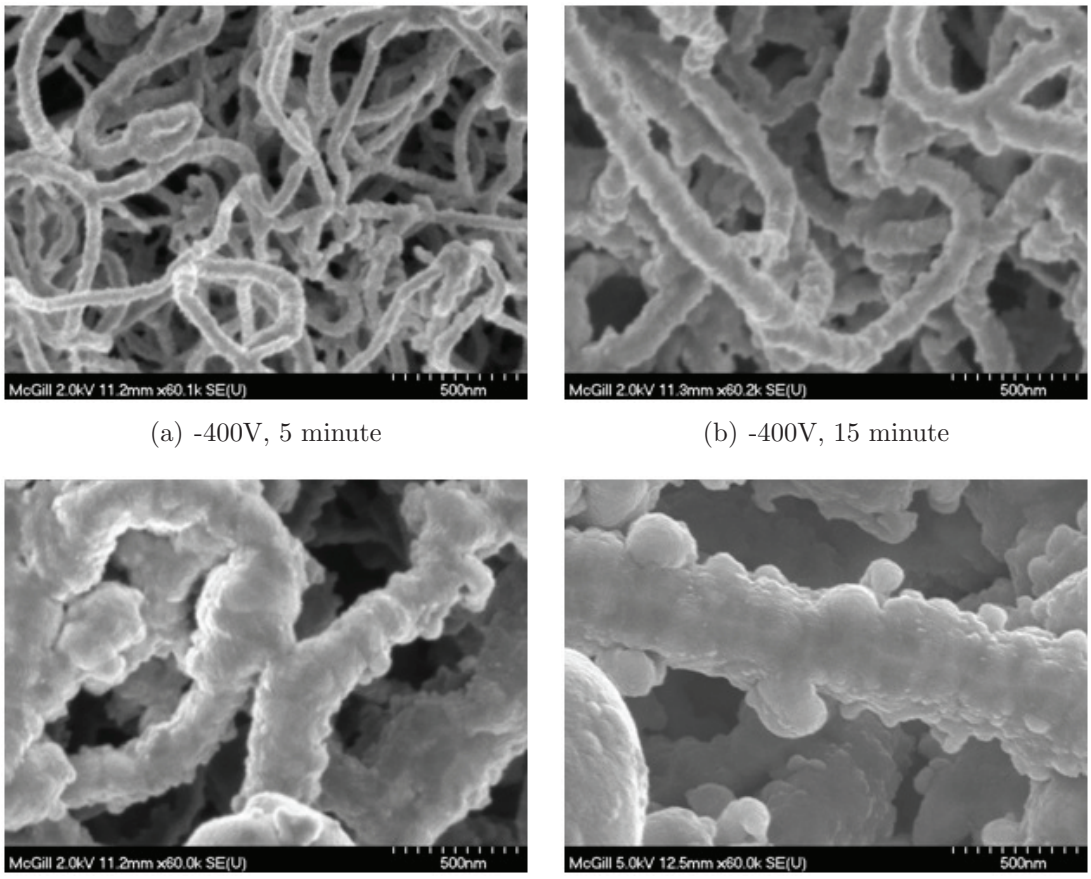

(a) -400V, 5 minute

(b) -400V, 15 minute

(c) -400V, 30 minute

(d) -400V, 60 minute

Figure 6–4: Scanning electron microscope images of CNTs coated with TiN. TiN was deposited at -400V bias and deposition times of (a) 5 min, (b) 15 min, (c) 30 min, and (d) 60 min, using cathodic arc deposition [158].

6.3 Principles of nanoindentation

The technique of nanoindentation has been widely used to measure the mechanical properties of thin films. This technique involves the application of a small load (in the range of a few micronewtons to tens of millinewtons) using an indenter (conospherical or Berkovich) on the surface of the test specimen, such that the depth of penetration is of the order of nanometers. The load is then withdrawn and the depth of indentation is continuously recorded for the entire loading-unloading cycle. Figure 6–5 shows a schematic of a typical load-displacement plot. The model proposed by Oliver and Pharr is commonly used to extract the elastic modulus and hardness from the load-displacement plot [163]. The major assumption of this model is that the loading segment contains contribution from both elastic and plastic deformation, while during unloading only the elastic component of the total displacement is recovered. The essential features of a load-displacement plot are shown in figure 6–5. To evaluate the contact stiffness (S) of the material under investigation, it is necessary to evaluate the slope of the unloading part of the load-displacement plot. The unloading part of the load-displacement plot can be modeled using:

$$P = \alpha(d - d_f)^m, \tag{6.1}$$

where P is the load, d is the displacement, and d_f is the final displacement of the indenter on complete unloading. α and m are power-law coefficients which are obtained through curve-fitting. The contact stiffness S is obtained by taking slope of this curve at the maximum displacement, d_{max}. In order to evaluate the elastic modulus and hardness of the material, it is necessary to know the contact area. The

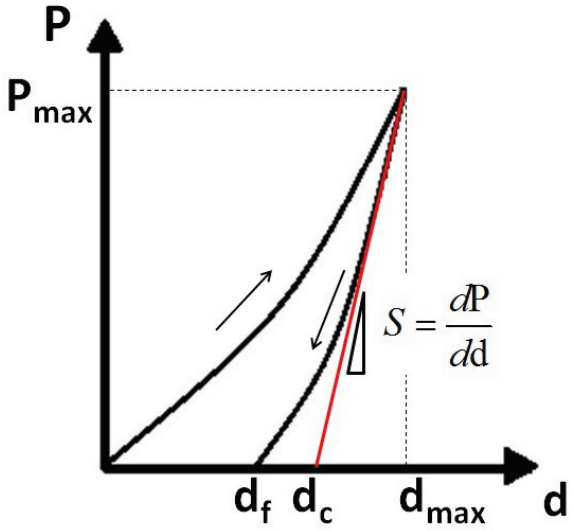

Figure 6–5: A schematic load(P) vs displacement plot (d) for an indentation experiment. P_{max} and d_{max} are the maximum load and displacement, respectively. d_f is the final displacement on complete unloading, and d_c is the depth along which contact is made along the indenter and the specimen. S is the contact stiffness and is defined as the slope of the unloading part of the load-displacement plot, represented by the red line, which is tangent to the unloading curve.

contact area can be estimated by measuring the dimensions of the residual imprint. Alternately, the contact depth d_c and the geometry of the indenter can be used to calculate the contact area, without the need for imaging the residual imprint. The contact depth for a conospherical indenter can be obtained, is given by [163, 164]:

$$d_c = d_{max} - 0.75\frac{P_{max}}{S}, \tag{6.2}$$

where d_{max} is the displacement corresponding to the maximum load P_{max}. The contact area A can then be defined as $A = F(d_c)$, where $F(d_c)$ is known as the area function. Determination of the area function requires careful calibration made

independently on materials with known elastic modulus. Once the area function is known, the effective elastic modulus, E_r (also known as reduced modulus and indentation modulus) can be calculated using the relation:

$$E_r = \frac{S\sqrt{\pi}}{2\sqrt{A}}. \tag{6.3}$$

The effective modulus takes into account the elastic properties of both the indenter and the indented material, and is given by:

$$\frac{1}{E_r} = \frac{1-\nu^2}{E} + \frac{1-\nu_i^2}{E_i}, \tag{6.4}$$

where E is the elastic modulus of the test-specimen, ν is the Poisson's ratio of the test specimen, E_i is the elastic modulus of the indenter tip, and ν_i is the Poisson's ratio of the indenter tip. Though equation 6.3 was derived to model the contact between a rigid indenter with a homogeneous elastic half-space [165], this equation was found to be valid for other material configurations such as open cell metallic foams [166], and hence justifies the use of equation 6.3 in the present context of measuring mechanical properties of CNT 'felt'. In the next section, several instances of using the Oliver-Pharr model for networks of CNTs are documented.

6.4 Literature review on nanoindentation of carbon nanotube networks

Since the discovery of carbon nanotubes by Iijima [167] a great deal of research has been directed towards evaluation of mechanical [168], electrical and thermal [169] properties of single CNTs. The properties of the CNTs vary depending on whether they are single-walled carbon nanotubes (SWNTs) or multi-walled carbon nanotubes (MwNTs), and also on the chirality of the nanotubes. However, the properties of

an intertwined network of CNTs are expected to be significantly different from the properties of stand-alone CNT. In literature, these networks are described variously as 'CNT felt', 'CNT turfs' or as 'CNT forests'.

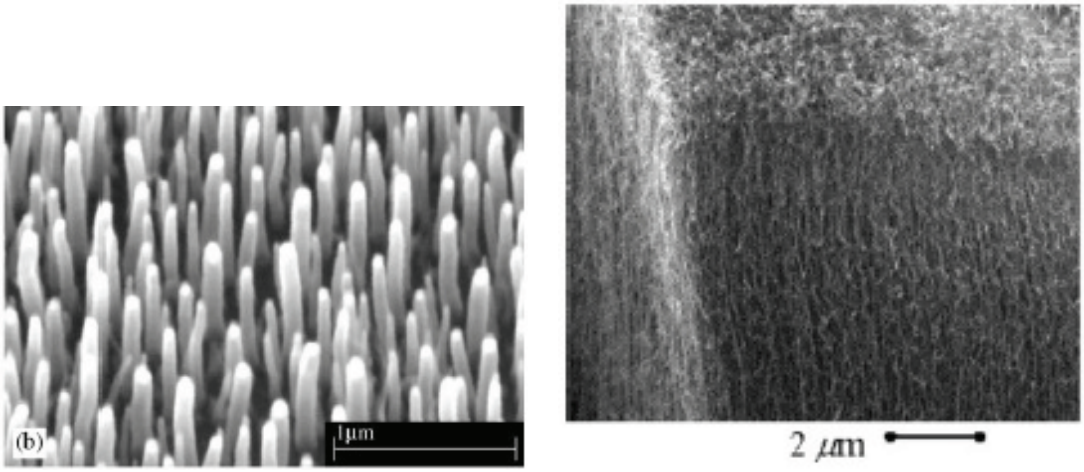

(a) VACNT forest (b) CNT turf

Figure 6–6: Arrays of carbon nanotubes: (a) Vertically aligned carbon nanotube (VACNT) 'forest', where the MWNTs are well-separated and are perfectly vertical [170], and (b) carbon nanotube 'turf', where the nanotubes are curved, and are predominantly vertical, with some of the CNTs being inclined or even horizontal [171].

Qi *et al.* performed nanoindentaion tests on arrays of vertically aligned carbon nanotubes (VACNTs) and evaluated the effective wall modulus and the effective axial modulus of a single MWNTs [170]. This structure consisted of thick, widely-spaced, and perfectly vertical MWNTs, as is shown in figure 6–6(a), and the indentation was performed using a steel AFM cantilever with a three-sided pyramidal diamond tip. The diamond tip had an apex angle of 60° and a tip-radius less than 25 nm. The geometry and arrangement of the CNTs and the indenter-tip led to successive bending of adjacent MWNTs as the pyramidal tip penetrated into the structure.

The load-displacement profile was modeled and effective bending and axial modulus of single MWNT was obtained. However, this work did not provide any quantitative data on the collective mechanical properties of the VACNT arrays. Qualitatively, from the load-displacement plots, it was inferred that VACNT arrays with higher areal density of nanotubes provided higher resistance to indentation, and that an array with the same areal density, but smaller (in terms of length) and thicker (in terms of diameter) nanotubes would also exhibit higher stiffness.

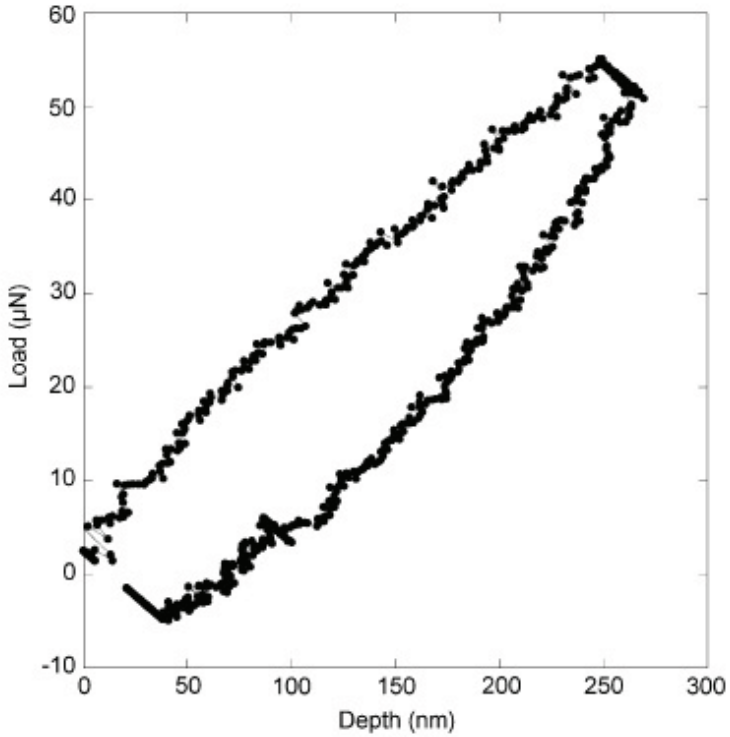

Figure 6–7: Typical load-displacement plot for a CNT turf, obtained with a Berkovich diamond indenter with effective tip-radius of 1.8 μm [172].

McCarter *et al.* performed quasi-static and dynamic nanoindentation tests on a CNT 'turf' using a Berkovich diamond tip with an effective tip-radius of 1.8 μm [172].

The Oliver and Pharr method [163] was used to extract effective elastic modulus from the load-displacement plots. Figure 6–7 shows a typical load-displacement plot for the CNT 'turf'. The salient features of the load-displacement plot are: (i) the deformation is completely reversible, (ii) the turf exhibits time-dependent relaxation when held at a constant load, and (iii) there exists strong adhesion between the tip and the turf, as shown by the negative load when the tip is being withdrawn from the turf. Besides, the elastic modulus of the turf was found to vary significantly with the density of the CNTs as well as with the number of contact-sites between the CNTs. For low number of contact-sites, the elastic modulus was found to be in the range of 0.03–0.08 GPa, while for a large number of contact-sites, the elastic modulus varied in the range of 0.1–0.3 GPa. In addition, the tangent modulus, obtained from the dynamic tests, was found to decrease with increasing strain. Mesarovic *et al.* developed a quasi-rheological, linear viscoelastic model to explain the load-displacement plot of the CNT turf [171]. Zbib *et al.* performed nanoindentation tests and compression tests on CNT turfs, patterned in the form of cylinders. Standard nanoindentation tests led to an effective elastic modulus of 14.9±5.7 MPa, and hardness of 2.5 MPa [173, 174].

6.5 Experimental procedure

Load-controlled nanoindentation tests were conducted to evaluate the contact stiffness and effective modulus of the CNT/TiN nanocomposites using a Hysitron Ubi nanoindenter with feedback control testing capability. The feedback control provided precise control of the nanoindentation probe in both load and displacement-controlled modes and is ideal for testing soft materials and ultra-thin films. It also

provides superior force sensitivity for the study of pre-contact tip-sample interaction. A conospherical indenter with tip-radius of 100 μm was used. Due to the open structure of the material, loads as low as 5–10 μN led to $\sim$100 nm displacement of the indenter in the depth direction for films which were 1–3 μm in thickness. Therefore, to ensure minimum effect from the substrate in the evaluation of elastic properties of the nanocomposite film, the applicable maximum load was restricted to 5–10 μN, with loading/unloading time of 5 seconds, and 2 second hold at the maximum load. All tests for the CNT/TiN nanocomposite films were performed at a maximum load of 10 μN, and loading/unloading rate of 2 μN/sec, as shown in figure 6–8. The pre-load for the tests was 1 μN and these load-control tests were feedback controlled. Standard protocols were followed for calibrating the nanoindenter and the tip-area function. The drift was measured before each test, so as to make corrections for thermal drift. The distance between adjacent indentations was chosen to be 10 μm. The contact stiffness was evaluated from the region between top 20% and 95% of the unloading part of the load versus displacement plot, using the TriboScan software. For each sample, at least 10 tests were done, and the mean value of contact stiffness and standard deviation were reported.

6.6 Results and discussions

Figures 6–9 show typical load-displacement plot obtained for the CNT felt. Figures 6–10, 6–11, 6–12, and 6–13 show typical load-displacement plots obtained for CNT/TiN nanocomposite deposited with a bias voltage of -150 V and TiN coating times of 5 minutes, 15 minutes, 30 minutes and 60 minutes, respectively. Similarly, figures 6–14, 6–15, 6–16, and 6–17 show typical load-displacement plots obtained for

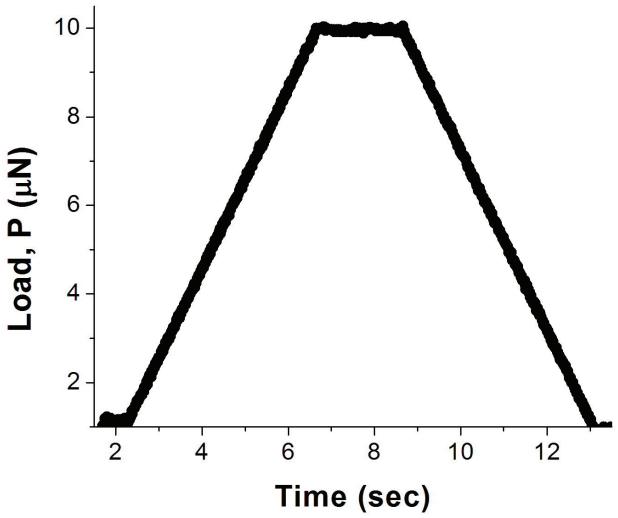

Figure 6–8: Load profile used for the load-controlled nanoindentation tests

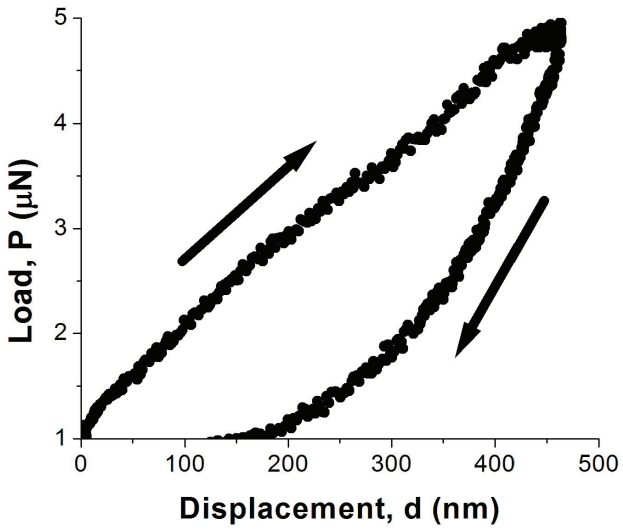

Figure 6–9: Typical load-displacement plot for a CNT felt.

CNT/TiN nanocomposites deposited with a bias voltage of -400V and TiN coating times of 5 minutes, 15 minutes, 30 minutes, and 60 minutes, respectively. The 1-D transducer used for the nanoindentation tests has a load resolution of 1 nN, a load noise floor of 100 nN, a displacement resolution of 0.04 nm and a displacement noise floor of 0.2 nm. The load versus displacement plots clearly show that the data collected are well above the load and displacement noise floors.

The CNT 'felt' possessed extremely low contact stiffness of 0.04±0.03 μN/nm, with an effective modulus of 4.4±2.7 MPa. The low value of effective modulus of the CNT 'felt' is similar to that of the CNT 'turf', however unlike the indentation response observed for the CNT 'turf', the CNT 'felt' and the CNT/TiN nanocomposite do not show any significant time-dependent relaxation when held at the maximum load. Moreover, no effect of adhesion between the tip and the sample was observed.

The effect of TiN coating time on the contact stiffness and effective modulus of the nanocomposites are shown in figure 6–19 and figure 6–18, respectively. In these figures the contact stiffness and effective modulus of CNT/TiN nanocomposite are plotted against TiN coating time for two sets of samples, as described in section 6.2. From the scanning electron microscope images in figures 6–3 and 6–4 it is evident that for both substrate bias voltages, the thickness of TiN coating around the CNTs increases with increasing TiN coating time. Figure 6–18 shows that increased TiN deposition times led to higher contact stiffness and effective modulus values for both bias voltages used. The average contact stiffness increased from 0.4 μN/nm to 2.6 μN/nm, while the effective modulus increased from 172 MPa to 2.5 GPa as the TiN coating time increases from 5 minutes to 60 minutes, the substrate bias being -150 V.

Similarly, for the case where the substrate bias is -400 V, the average contact stiffness increased from 0.18 μN/nm to 1.86 μN/nm, and effective modulus increased from 64 MPa for 5 minutes of TiN deposition to 1.6 GPa for 60 minutes of TiN deposition. In addition, for a given sample, the standard deviation in the contact stiffness and effective modulus was as high as 60% of the average value. This variation is consistent with expectations based on the microstructure and topography from one location to another.

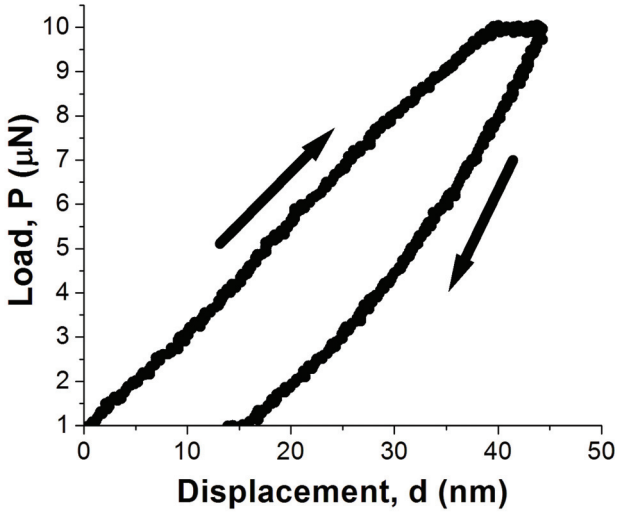

Figure 6–10: Typical load versus displacement plots for CNT/TiN nanocomposites, where TiN is deposited with a bias voltage of -150 V, and coating time of 5 minutes.

The scanning electron microscope images also indicate that substrate bias voltage during TiN deposition has an effect on the microstructure. A bias voltage of -400 V leads to a deeper penetration of TiN in the CNT network compared to that obtained with a bias voltage of -150 V, where deposition of TiN mainly occurs on

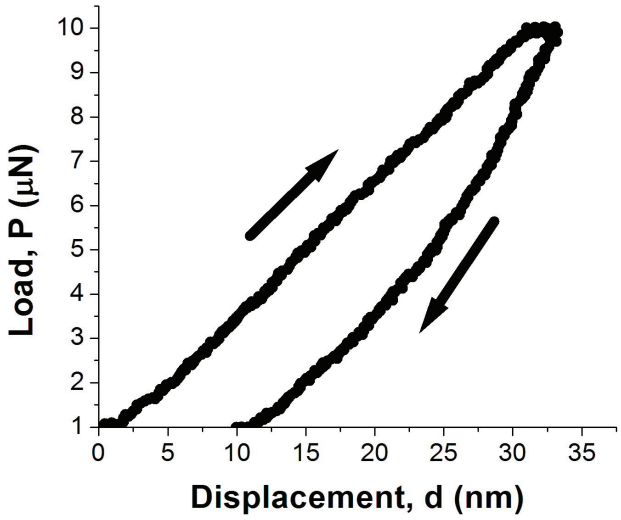

Figure 6–11: Typical load versus displacement plots for CNT/TiN nanocomposites, where TiN is deposited with a bias voltage of -150 V, and coating time of 15 minutes.

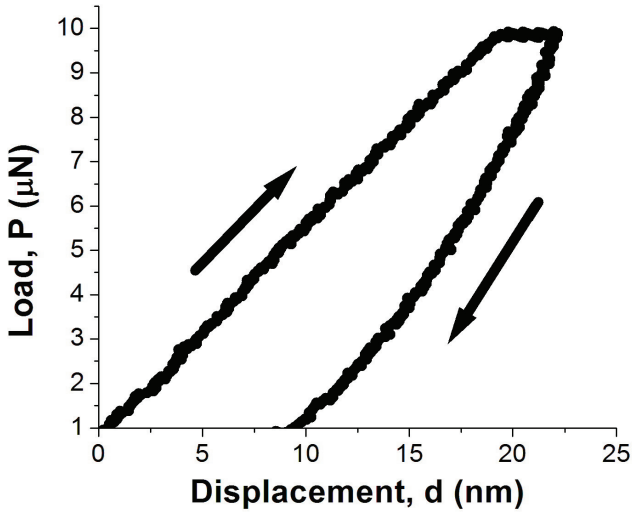

Figure 6–12: Typical load versus displacement plots for CNT/TiN nanocomposites, where TiN is deposited with a bias voltage of -150 V, and coating time of 30 minutes.

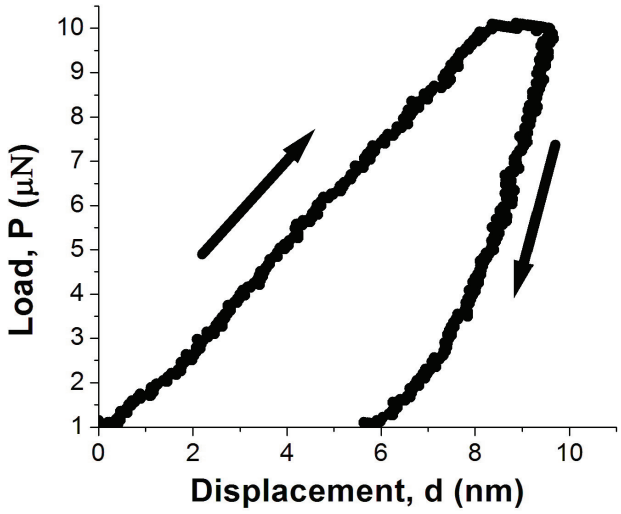

Figure 6–13: Typical load versus displacement plots for CNT/TiN nanocomposites, where TiN is deposited with a bias voltage of -150 V, and coating time of 60 minutes.

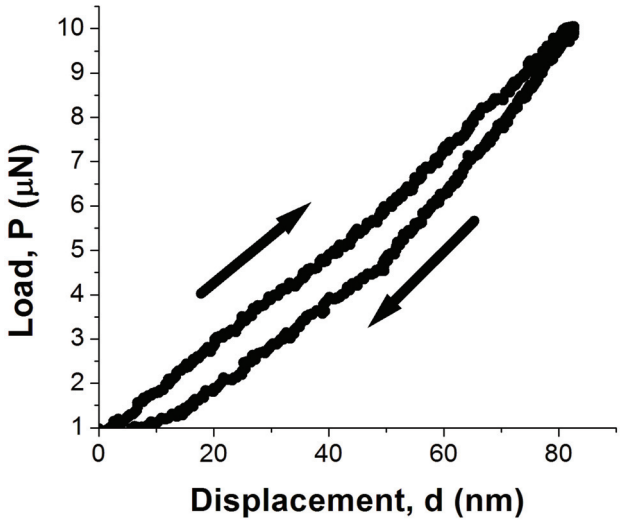

Figure 6–14: Typical load versus displacement plots for CNT/TiN nanocomposites, where TiN is deposited with a bias voltage of -400 V, and coating times of 5 minutes.

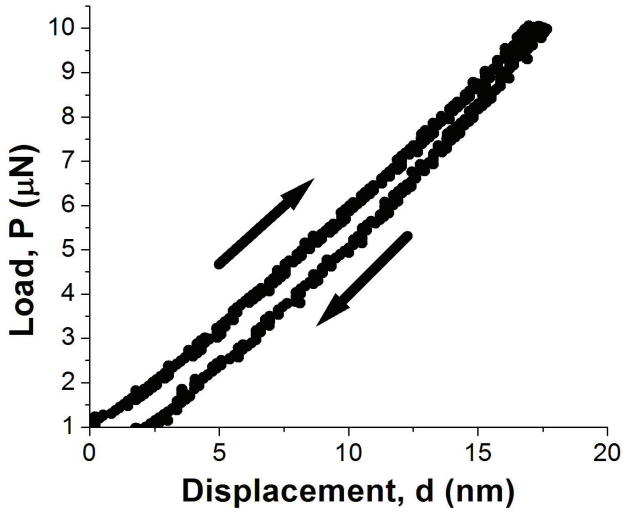

Figure 6–15: Typical load versus displacement plots for CNT/TiN nanocomposites, where TiN is deposited with a bias voltage of -400 V, and coating times of 15 minutes.

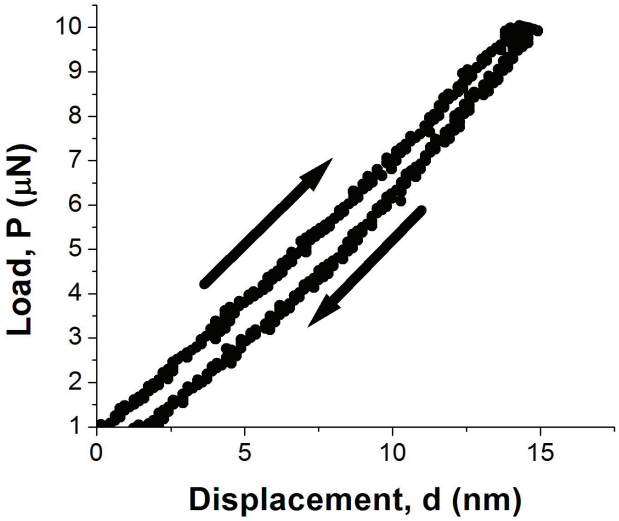

Figure 6–16: Typical load versus displacement plots for CNT/TiN nanocomposites, where TiN is deposited with a bias voltage of -400 V, and coating times of 30 minutes.

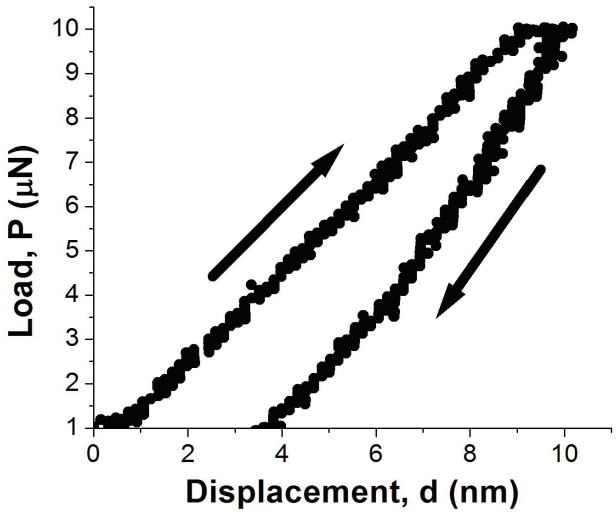

Figure 6–17: Typical load versus displacement plots for CNT/TiN nanocomposites, where TiN is deposited with a bias voltage of -400 V, and coating times of 60 minutes.

the exposed CNTs on the topmost surface. However, figure 6–18 shows that this difference in microstructure does not translate into significantly different values for effective modulus. But, on examining the load-displacement plots of the nanocomposites deposited at the two different bias voltages, it was observed that the unloading curve follows the loading curve more closely, and that the final displacement (d_f) was lesser for the nanocomposites deposited using -400 V bias voltage, than those deposited using -150 V bias voltage. This indicates a difference in the deformation mechanism of the two nanocomposites.

6.7 Potential applications

One potential application of the CNT/TiN nanocomposite is in the field of RF-MEMS as switches. Figure 6–20 shows a schematic of a typical RF-MEMS switch.

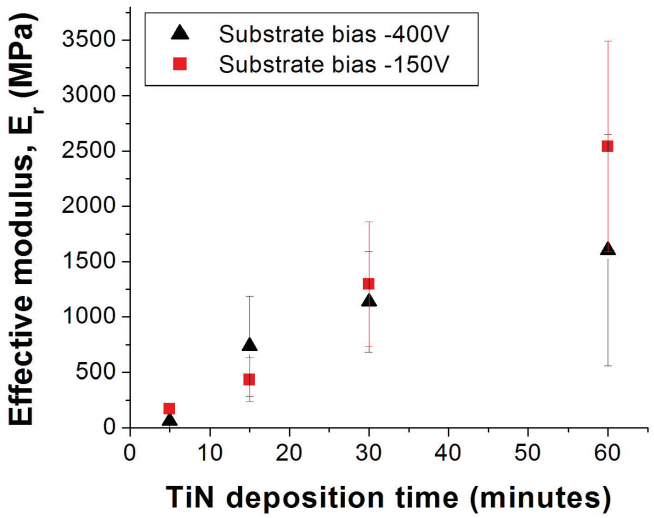

Figure 6–18: Variation of effective elastic modulus of the CNT/TiN nanocomposites as a function of TiN coating time. TiN coating was performed using two substrate bias voltages of -150 V and -400 V.

The CNT/TiN nanocomposite can be used as the upper contact and/or the lower contact dimple. Historically, metals such as gold (Au) have been used as the material for electrical contacts in MEMS switches. The poor reliability of the MEMS switches has been attributed to wear of the metallic coating under service conditions [176]. McBride *et al.* have suggested the use of CNT/Au composites as a solution to the above problem, since the CNT/Au nanocomposite possesses the desirable properties required for a material to act as an electrical contact, namely high conductivity and high resistance to wear and oxidation [176, 177]. However, this CNT/Au composite is also subject to wear due to localized melting of gold during each contact. One way to circumvent this problem is to replace Au with TiN, and hence solve problems of electro-migration and localized melting which are usually associated with metals.

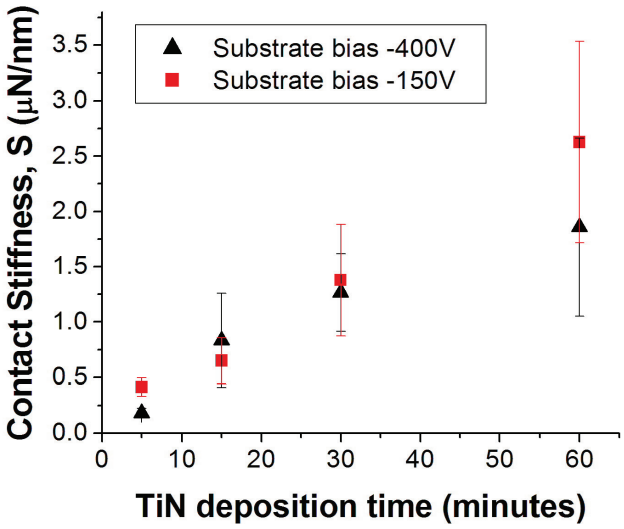

Figure 6–19: Variation of contact stiffness of the CNT/TiN nanocomposites as a function of TiN coating time. TiN coating was performed using two substrate bias voltages of -150 V and -400 V.

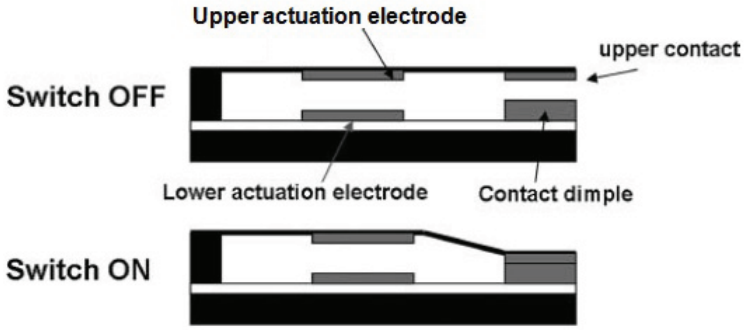

Figure 6–20: Basic structure of a RF-MEMS switch along with the 'on' and 'off' states [175].

6.8 Summary

In this chapter, the effective modulus of CNT 'felt' and CNT/TiN nanocomposites have been evaluated by nanoindentation using the Oliver-Pharr model. The effect of TiN coating time as well as the effect of a process parameter, namely the substrate bias voltage during TiN deposition, was evaluated. As expected, for both bias voltages used, the effective modulus increases with increasing TiN deposition time from about 4 MPa for bare CNT felt (without TiN) to around 2.5 GPa for CNT felt coated with TiN for 60 minutes. The CNT felt and the CNT/TiN nanocomposites did not show any viscoelastic response as was observed in the literature for CNT arrays. The low elastic modulus, leading to high compressibility, along with negligible adhesion of the CNT/TiN nanocomposites make them useful materials for MEMS switches. In this context, the CNT/TiN nanocomposites deposited using substrate bias of -150 V are more suitable due to the lower residual displacement on unloading than the CNT/TiN nanocomposites deposited using substrate bias of -400 V.

CHAPTER 7
Conclusions and future work

This thesis explored the integration of nanostructured materials with microsystems, and focused on two major challenges for integration. The first challenge is that of processing, and the second challenge is obtaining process-structure-property relationships of nanomaterials integrated with MEMS.

Chapters 2 and 3 dealt with the issue of processing. Chapter 2 presented a literature review of the various routes of integration. Both bottom-up and top-down methods, including methods for integrating nanocomposites to MEMS, were reviewed based on their level of control over direction, location, dispersion as well as whether the method can be applied as a wafer-level process or a device-level process. Bottom-up methods like self-assembly are parallel processes and are ideal for cases requiring a uniform distribution of nanomaterials. On the other hand, top-down nanofabrication processes allow excellent nanometer-level control over position and direction, but are either extremely costly or are serial processes. Hence top-down methods are restricted to high-end and low-volume applications. Hybrid processes which combine the ease of integration and parallel nature of bottom-up processes with nanometer-level control over location, direction and dispersion of nanomaterials of top-down processes need to be developed for making the leap from academic laboratories to industry.

In addition, one gap in integration methods, namely, the lack of an approach to integrate metallic nanostructures as a final step after micromachining MEMS

structures was identified. Chapter 3 addressed this gap by developing an approach combining spray-coating of electron beam resists, electron beam lithography, physical vapour deposition and lift-off processes to obtain polymeric and metallic nanostructures on micromachined MEMS structures. This approach holds promise since it enables rapid development of prototype nanomaterial-integrated devices, based on previously existing MEMS structures.

The remaining chapters of the thesis explored the second issue of establishing process-structure-property relationships for three different nanomaterials. The first of these studies dealt with single-walled carbon nanotubes(SWNT)/polyimide(PI) nanocomposites. Measurement of elastic modulus and microstructural examination of nanocomposite thin films performed in this study established that the method of synthesis was inadequate to produce nanocomposite films with uniform dispersion of carbon nanotubes beyond 0.5 volume%. Hence, the processing route requires modification, for example, by the addition of surfactants, to enable higher loading of nanomaterials, while maintaining a uniform dispersion. In addition, processes for etching such nanocomposite films need to be developed to fabricate nanocomposite MEMS devices. One promising approach is the fabrication of polymer nanocomposites with aligned carbon nanotubes [70].

The second study dealt with the measurement of internal friction of aluminium nanowires. These measurements were made using a microcantilever platform, which has been previously used for damping studies of metallic thin films [8, 98]. The extension of this platform to nanowires required developments on three fronts: (i) patterning nanowires on a micromachined microresonator, (ii) developing a protocol

for measuring damping of these nanostructures using the microcantilever platform, so that support losses can be segregated from losses intrinsic to the material, and (iii) formulating a model to extract internal friction of the nanowires from total damping of a nanowire-integrated composite microresonator. This study showed that the values of internal friction of aluminium nanowires at room temperature matched closely with those for aluminium thin films of the same thickness, measured over a similar frequency range. The average grain size was significantly less than the width of the nanowires measured in this study. Expectations based on the mechanism of grain-boundary sliding suggest that significant size effects will appear in nanowires with grain sizes comparable to width.

The third study explored the mechanical properties of a porous nanocomposite film consisting of a carbon nanotube network that was conformally coated with a thin film of titanium nitride (TiN). The architecture of this nanocomposite is inherently non-uniform, which led to significant variations in mechanical properties from location to location. The effective modulus was measured using nanoindentation and was found to increase in proportion to the thickness of the TiN coating.

In summary, the contributions of this thesis - processes for materials integration, techniques for measuring material properties, and process-structure-property relationships for three nanomaterials - establish a foundation for rational integration of nanomaterials with MEMS.

7.1 Suggestions for future research

The foundation established by this thesis can be developed in several different directions. Some of these are discussed below.

Extending the nanofabrication approach to new materials and to lower linewidths

The idea of nanofabrication on micromachined structures presented in chapter 3 can be extended to lower linewidths either by reducing the thickness of the spray-coated resist, or by using electron beam plotters operated at high accelerating voltages of the order of hundred kilovolts. More materials like ceramic oxides available through sol-gel processing route can also be included by optimizing spray-coating parameters for the 'sol'. Another extension of this approach is to parallel, non-contact nanofabrication techniques. The first step in this direction will be to develop spray-coating procedures for resists used in deep ultra-violet lithography and extreme ultra-violet lithography.

Establishing process-structure-property relationships of polymer nanocomposite films

In addition to carbon nanotubes, polymer films reinforced with nanomaterials in the form of nanoparticles and nanowires can have applications in microsystems, where they can act as structural and/or functional components. For example, silver in the form of nanowires and nanoparticles can be added to photoresists like SU8 to improve structural (mechanical) properties like elastic modulus. Figure 7–1 shows Eshelby-Mori-Tanaka predictions of elastic modulus of SU8 nanocomposites, as a function of volume fraction of the reinforcement phase, which can be in the form of nanowires or nanoparticles. Even when the improvement of mechanical properties is not significant (as in the case of reinforcement with nanoparticles or randomly-aligned nanowire, especially at low volume fractions), there can be a significant improvement in electrical, magnetic and chemical properties. For example, addition

of low volume fraction of silver nanoparticles can improve electrical conductivity of the nanocomposite film. The effect of nanomaterial reinforcement on physical and chemical properties of the nanocomposite films should continue to be studied, and process-structure-property relationships of nanocomposite films with various combinations of matrices and reinforcements need to be established to aid designers of microsystems in selection of appropriate materials and processes.

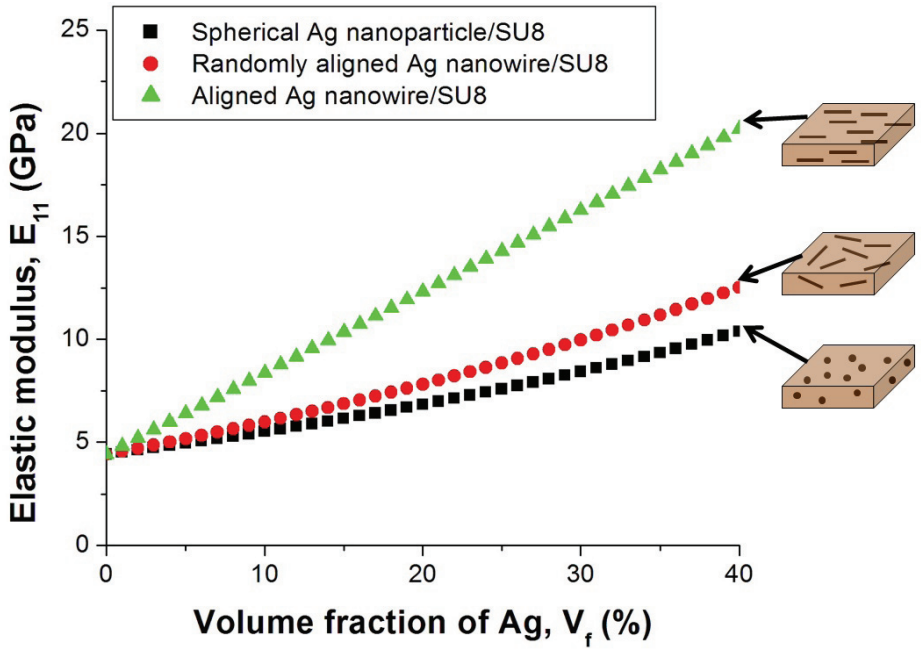

Figure 7–1: Variation of elastic modulus of Ag/SU8 nanocomposite as a function of volume fraction and geometry of Ag.

Exploration of size-effects of internal friction of nanomaterials

Systematic studies of the effects of frequency and temperature on internal friction of nanomaterials are crucial to explore size-effects in internal friction of nanomaterials. The microcantilever platform discussed in chapter 5 provides a tool to systematically study internal friction of nanomaterials in the form of ultra-thin films and patterned arrays of nanowires of metals. This platform can be used to explore size-effects of nanomaterials in the form of nanowires, nanotubes and nanoparticles, which can be patterned, grown and assembled on the microcantilever. Experiments need to be designed to evaluate the contribution from the various dissipation sources. The effects of adhesion between the nanomaterial and the microcantilever in the form of interfacial sliding is likely to gain prominence for some categories of self-assembled nanomaterials.

Exploring the applicability of porous nanocomposite films as MEMS switches

Porous nanocomposite films, consisting of carbon nanotube network coated with a thin film of titanium nitride, exhibit large compressibility and low adhesion. These properties make them potential candidates for MEMS switches. A future direction of work with this material can involve testing the applicability of such composites as MEMS switches. This can be done by selectively growing vertically aligned carbon nanotube arrays, coating them with a wear-resistant, conductive layer like titanium nitride, and then comparing such structures with conventional MEMS switches in terms of conduction, adhesion to the other electrode, and reliability.

APPENDIX A
Eshelby-Mori-Tanaka micromechanics

Consider a two-phase composite consisting of a matrix phase with stiffness $\mathbf{C}_m$, and a reinforcement phase with stiffness tensor $\mathbf{C}_f$. The volume fractions of the matrix and reinforcement are V_m and V_f, respectively, such that $V_m + V_f = 1$. Consider an average stress $\bar{\sigma}$ applied to a composite, leading to an average strain $\bar{\epsilon}$. The applied stress is distributed among the constituent phases, such that

$$\bar{\sigma} = V_m \bar{\sigma}_m + V_f \{\bar{\sigma}_f\}, \tag{A.1}$$

where $\bar{\sigma}_m$ and $\bar{\sigma}_f$ are average stresses in the matrix and in the reinforcement, respectively, and curly brackets denote average over all possible orientations. Now, $\bar{\sigma}_m = \mathbf{C}_m \bar{\epsilon}_m$, and $\bar{\sigma}_f = \mathbf{C}_f \bar{\epsilon}_f$, where $\bar{\epsilon}_m$ and $\bar{\epsilon}_f$ are average strains in the matrix and in the reinforcement, respectively. The effective stiffness tensor of the composite is given by

$$\mathbf{C}_c = \frac{\bar{\sigma}}{\bar{\epsilon}}. \tag{A.2}$$

Now, we define orientation dependent tensors $\mathbf{A_m}$ and $\mathbf{A_f}$ for the matrix and reinforcement respectively, called the 'concentration factors' as:

$$\bar{\epsilon}_m = \mathbf{A}_m \bar{\epsilon}; \tag{A.3}$$

$$\bar{\epsilon}_f = \mathbf{A}_f \bar{\epsilon}, \tag{A.4}$$

such that $V_m\mathbf{A}_m + V_f\mathbf{A}_f = \mathbf{I}$. Using equations A.1 and A.2, we get

$$\mathbf{C}_c = \mathbf{C}_m + V_f\{(\mathbf{C}_f - \mathbf{C}_m)\,\mathbf{A}_f\}. \tag{A.5}$$

Evaluation of the fourth order stiffness tensor for the composite thus requires evaluation of equation A.5. Since the volume fraction of the reinforcement, stiffness matrices of the constituent matrix and reinforcement phases are already known, knowledge of the concentration factor of the reinforcement is sufficient to evaluate the stiffness tensor of the composite. We are interested in calculating the stiffness tensor for a 'non-dilute' composite i.e. a composite where interaction between the reinforcements are significant. To this end we first present the Eshelby approach and calculate the concentration factor tensor for 'dilute' approximation [105]. Next, we extend the analysis to non-dilute regime using a modified Mori-Tanaka approach [107].

Eshelby approach

Eshelby approach is based on representing the actual inclusion by one which is ellipsoidal in shape and is made of the matrix material. This inclusion is known as the 'equivalent homogeneous inclusion' and an appropriate strain (known as the 'equivalent transformation strain') is chosen such that the stress field is identical to that of the original reinforcement. The ellipsoidal shape of the reinforcement and the equivalent homogeneous inclusion ensures that stress and strain at all points within it is uniform. In order to calculate the stress in this equivalent homogeneous inclusion, Eshelby imagined a series of cutting and joining steps. In the first step, an ellipsoidal volume is cut from the matrix and is allowed to undergo a uniform stress-free transformation, giving rise to a transformation strain, ϵ^T in the inclusion. Then

surface tractions are applied to return it to its original shape, such that strain in the inclusion is zero. Next, the equivalent homogeneous inclusion is put back in the hole in the matrix (the region from which the inclusion was removed), the surfaces are joined and the surface tractions are removed. On reaching equilibrium, the constrained shape of the inclusion leads to a constrained strain ϵ^C in the homogeneous inclusion. The constrained strain and the transformation strain are related by:

$$\epsilon^C = \mathbf{S}\epsilon^T, \tag{A.6}$$

where $\mathbf{S}$ is the Eshelby tensor.This tensor is calculated in terms of the aspect ratio of the inclusion and the Poissson's ratio of the matrix material.

Let us consider a composite subject to an average strain $\bar{\epsilon}$. The total stress in the equivalent homogeneous inclusion is given by:

$$\sigma^{homogeneous} = \mathbf{C}_m \left(\bar{\epsilon} + \epsilon^C - \epsilon^T\right). \tag{A.7}$$

Similarly, the stress in the real inclusion is given by:

$$\sigma^{real} = \mathbf{C}_f \left(\bar{\epsilon} + \epsilon^C\right). \tag{A.8}$$

Since these two stresses must be equal, therefore from equations A.7 and A.8, and using equation A.6 we get

$$\epsilon^T = {\mathbf{C}_m}^{-1} \left(\mathbf{C}_m - \mathbf{C}_f\right) \bar{\epsilon}_f. \tag{A.9}$$

Again the strain in the real inclusion is given by:

$$\bar{\epsilon}_f = \bar{\epsilon} + \epsilon^C. \tag{A.10}$$

Using equations A.6and equation A.9 in equation A.10 we get the strain in the real inclusion in terms of the average strain in the composite as:

$$\bar{\epsilon}_f = \left[\mathbf{I} + \mathbf{S}\mathbf{C}_m{}^{-1}\left(\mathbf{C}_m - \mathbf{C}_f\right)\right]^{-1}\bar{\epsilon}. \tag{A.11}$$

Comparing equations A.4 and A.11 allows us to evaluate $\mathbf{A}_f$ as:

$$\mathbf{A}_f = \left[\mathbf{I} + \mathbf{S}\mathbf{C}_m{}^{-1}\left(\mathbf{C}_m - \mathbf{C}_f\right)\right]^{-1}. \tag{A.12}$$

But this represents the case for a single inclusion in an infinite matrix and does not take into account the interaction between the inclusions. Hence, Eshelby formulation is valid only for composites with 'dilute' or very low concentration of the reinforcement phase.

Mori-Tanaka approach

When multiple inclusions are present in the matrix, the stress fields of the inclusions interact. Mori-Tanaka approach takes into consideration the interaction of the inclusions in the matrix by modeling these interacting stress fields as an average background stress. The concept of this background stress is introduced in the Eshelby approach, as if it is externally applied, and this facilitates the extension of the Eshelby approach to composites having high volume fraction of reinforcements in the matrix. Again, we follow the same analysis as the Eshelby approach, and equate the stresses in the equivalent homogeneous inclusion and the actual inclusion. The only difference is the presence of the average background strain (ϵ_b) in the matrix due to the presence of all the inclusions. Therefore,

$$\mathbf{C}_m\left(\bar{\epsilon} + \epsilon^C + \epsilon_b - \epsilon^T\right) = \mathbf{C}_f\left(\bar{\epsilon} + \epsilon_b + \epsilon^C\right). \tag{A.13}$$

It is easy to show from equation A.13, using equation A.6, that

$$\bar{\epsilon}_f = \left[\mathbf{I} + \mathbf{S}{\mathbf{C}_m}^{-1}\left(\mathbf{C}_m - \mathbf{C}_f\right)\right]^{-1}\bar{\epsilon}_m \tag{A.14}$$

Therefore, we find that $\bar{\epsilon}_f = {\mathbf{A}_f}^{dilute}\bar{\epsilon}_m$. Now, we assume the average strain distribution in the composite is

$$\bar{\epsilon} = V_m\bar{\epsilon}_m + V_f\left\{\bar{\epsilon}_f\right\}. \tag{A.15}$$

Using equations A.14, A.4 in the equation A.15, we get the concentration factor tensor for the in a 'non-dilute' composite as:

$$\mathbf{A}_f = {\mathbf{A}_f}^{dilute}\left[V_m\mathbf{I} + V_f\left\{{\mathbf{A}_f}^{dilute}\right\}\right]^{-1}. \tag{A.16}$$

Therefore, stiffness tensor for a 'non-dilute' composite can be evaluated using equation A.5. This gives

$$\mathbf{C}_c = \mathbf{C}_m + V_f\{(\mathbf{C}_f - \mathbf{C}_m)\mathbf{A}_f\}[(1 - V_f)\mathbf{I} + V_f\{\mathbf{A}_f\}]^{-1} \tag{A.17}$$

Eshelby-Mori-Tanaka approach has been used to predict the elastic modulus of composites with nano-scale reinforcements. A wide variety of matrices (polymer, metallic and ceramic) and reinforcements have been studied using this approach. The matrices and reinforcements are usually assumed to be isotropic (unless specified otherwise) and two geometries of reinforcement, namely spherical nanoparticle and cylindrical nanowire, have been considered by selecting appropriate Eshelby tensors. The interfaces between the reinforcement phase and the matrix have been assumed to be optimized for a perfect load transfer. The dispersion of the reinforcement phase in the matrix has been assumed to be uniform. Figure A–1 show one example of

such analysis, where the elastic modulus of polymer matrix composites have been plotted as functions of their reinforcement content. In all cases, the increase in elastic modulus due to nanowire reinforcement exceeds that due to spherical nanoparticles, and the alignment of the nanowires in the matrix yields much higher elastic modulus compared to the randomly aligned nanowires or nanoparticles.

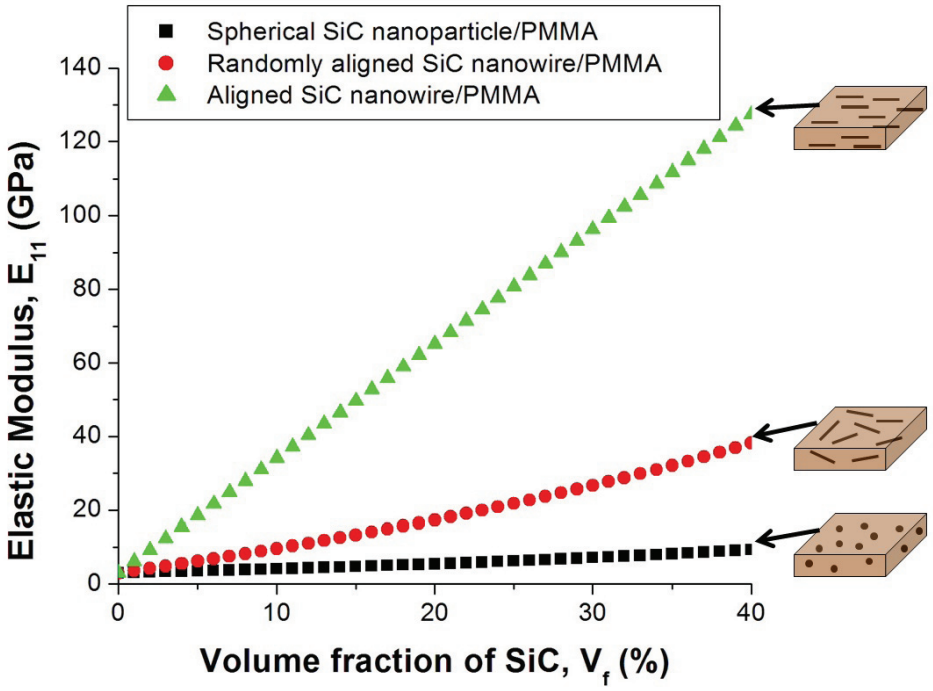

Figure A–1: Variation of elastic modulus of SiC/PMMA nanocomposite as a function of volume fraction and geometry of SiC.

References

[1] J. Bryzek, S. Roundy, B. Bircumshaw, C. Chung, K. Castellino, J. Stetter, and M. Vestel, "Marvelous MEMS," *IEEE Circuits and Devices Magazine*, vol. 22, no. 2, pp. 8–28, 2006.

[2] E. Mounier and L. Robin, "Status of the MEMS industry 2011," tech. rep., Yole Developpement, 2011.

[3] P. Sarro, "Silicon carbide as a new MEMS technology," *Sensors and Actuators A: Physical*, vol. 82, no. 1-3, pp. 210–218, 2000.

[4] P. French, P. Sarro, R. Mallee, E. Fakkeldij, and R. Wolffenbuttel, "Optimization of a low-stress silicon nitride process for surface-micromachining applications," *Sensors and Actuators A: Physical*, vol. 58, no. 2, pp. 149–157, 1997.

[5] O. Auciello, J. Birrell, J. Carlisle, J. Gerbi, X. Xiao, B. Peng, and H. Espinosa, "Materials science and fabrication processes for a new MEMS technology based on ultrananocrystalline diamond thin films," *Journal of Physics: Condensed Matter*, vol. 16, p. R539, 2004.

[6] S. Wilson, R. Jourdain, Q. Zhang, R. Dorey, C. Bowen, M. Willander, Q. Wahab, and S. Al-hilli, "New materials for micro-scale sensors and actuators: An engineering review," *Materials Science and Engineering: R: Reports*, vol. 56, no. 1-6, pp. 1–129, 2007.

[7] M. Ashby, P. Ferreira, and D. Schodek, *Nanomaterials, Nanotechnologies and Design: An Introduction for Engineers and Architects*. Elsevier, 2009.

[8] G. Sosale, S. Prabhakar, L. Fréchette, and S. Vengallatore, "A microcantilever platform for measuring internal friction in thin films using thermoelastic damping for calibration," *Journal of Microelectromechanical Systems*, no. 99, pp. 1–10, 2011.

[9] S. Senturia, *Microsystem design*. Springer Netherlands, 2001.

[10] B. Alaca, "Integration of one-dimensional nanostructures with microsystems: An overview," *International Materials Reviews*, vol. 54, no. 5, p. 245, 2009.

[11] Q. Ye, A. Cassell, H. Liu, K. Chao, J. Han, and M. Meyyappan, "Large-scale fabrication of carbon nanotube probe tips for atomic force microscopy critical dimension imaging applications," *Nano Letters*, vol. 4, no. 7, pp. 1301–1308, 2004.

[12] G. Whitesides and B. Grzybowski, "Self-assembly at all scales," *Science*, vol. 295, no. 5564, p. 2418, 2002.

[13] Y. Wang and W. Zhou, "A review on inorganic nanostructure self-assembly," *Journal of Nanoscience and Nanotechnology*, vol. 10, no. 3, pp. 1563–1583, 2010.

[14] H. Pohl, *Dielectrophoresis: The Behavior of Neutral Matter in Nonuniform Electric Fields*. Cambridge University Press Cambridge, 1978.

[15] C. Yu, Q. Hao, S. Saha, L. Shi, X. Kong, and Z. Wang, "Integration of metal oxide nanobelts with microsystems for nerve agent detection," *Applied Physics Letters*, vol. 86, p. 063101, 2005.

[16] K. Benkstein, C. Martinez, G. Li, D. Meier, C. Montgomery, and S. Semancik, "Integration of nanostructured materials with MEMS microhotplate platforms to enhance chemical sensor performance," *Journal of Nanoparticle Research*, vol. 8, pp. 809–822, 2006. 10.1007/s11051-005-9019-8.

[17] C. Hangarter and N. Myung, "Magnetic alignment of nanowires," *Chemistry of Materials*, vol. 17, no. 6, pp. 1320–1324, 2005.

[18] S. Niyogi, C. Hangarter, R. Thamankar, Y. Chiang, R. Kawakami, N. Myung, and R. Haddon, "Magnetically assembled multiwalled carbon nanotubes on ferromagnetic contacts," *The Journal of Physical Chemistry B*, vol. 108, no. 51, pp. 19818–19824, 2004.

[19] E. Kim, Y. Xia, and G. Whitesides, "Micromolding in capillaries: Applications in materials science," *Journal of the American Chemical Society*, vol. 118, no. 24, pp. 5722–5731, 1996.

[20] Y. Huang, X. Duan, Q. Wei, and C. Lieber, "Directed assembly of one-dimensional nanostructures into functional networks," *Science*, vol. 291, no. 5504, p. 630, 2001.

[21] A. Zribi, A. Knobloch, and R. Rao, "CO_2 detection using carbon nanotube networks and micromachined resonant transducers," *Applied Physics Letters*, vol. 86, p. 203112, 2005.

[22] Q. Wan, Q. Li, Y. Chen, T. Wang, X. He, J. Li, and C. Lin, "Fabrication and ethanol sensing characteristics of ZnO nanowire gas sensors," *Applied Physics Letters*, vol. 84, p. 3654, 2004.

[23] Z. Gu, D. Gracias, and A. Tseng, *Nanowire Assembly and Integration*, ch. 6, pp. 187–211. World Scientific Publishing Co. Pte. Ltd.: Singapore, 2008.

[24] B. Sosnowchik and L. Lin, "Rapid synthesis of carbon nanotubes by bulk and localized inductive heating," *IEEE 20th International Conference onMicro Electro Mechanical Systems*, pp. 835–838, 2007.

[25] S. Han, X. Liu, and C. Zhou, "Template-free directional growth of single-walled carbon nanotubes on a-and r-plane sapphire," *Journal of the American Chemical Society*, vol. 127, no. 15, pp. 5294–5295, 2005.

[26] W. Teh, C. Smith, K. Teo, R. Lacerda, G. Amaratunga, W. Milne, M. Castignolles, and A. Loiseau, "Integrating vertically aligned carbon nanotubes on micromechanical structures," *Journal of Vacuum Science & Technology B: Microelectronics and Nanometer Structures*, vol. 21, p. 1380, 2003.

[27] O. Englander, D. Christensen, and L. Lin, "Local synthesis of silicon nanowires and carbon nanotubes on microbridges," *Applied Physics Letters*, vol. 82, p. 4797, 2003.

[28] E. Sunden, T. Wright, J. Lee, W. King, and S. Graham, "Room-temperature chemical vapor deposition and mass detection on a heated atomic force microscope cantilever," *Applied Physics Letters*, vol. 88, p. 033107, 2006.

[29] M. Yu, O. Lourie, M. Dyer, K. Moloni, T. Kelly, and R. Ruoff, "Strength and breaking mechanism of multiwalled carbon nanotubes under tensile load," *Science*, vol. 287, no. 5453, pp. 637–640, 2000.

[30] D. Meier, S. Semancik, B. Button, E. Strelcov, and A. Kolmakov, "Coupling nanowire chemiresistors with mems microhotplate gas sensing platforms," *Applied Physics Letters*, vol. 91, p. 063118, 2007.

[31] K. Carlson, K. Andersen, V. Eichhorn, D. Petersen, K. Mølhave, I. Bu, K. Teo, W. Milne, S. Fatikow, and P. Bøggild, "A carbon nanofibre scanning probe

assembled using an electrothermal microgripper," *Nanotechnology*, vol. 18, p. 345501, 2007.

[32] K. Ekinci and M. Roukes, "Nanoelectromechanical systems," *Review of Scientific Instruments*, vol. 76, p. 061101, 2005.

[33] T. Toriyama, Y. Tanimoto, and S. Sugiyama, "Single crystal silicon nanowire piezoresistors for mechanical sensors," *Journal of Microelectromechanical Systems*, vol. 11, no. 5, pp. 605–611, 2002.

[34] T. Toriyama and S. Sugiyama, "Single crystal silicon piezoresistive nano-wire bridge," *Sensors and Actuators A: Physical*, vol. 108, no. 1-3, pp. 244–249, 2003.

[35] S. Donthu, N. Alem, Z. Pan, S. Li, G. Shekhawat, V. Dravid, K. Benkstein, and S. Semancik, "Directed fabrication of ceramic nanostructures on fragile substrates using soft-electron beam lithography (soft-eBL)," *IEEE Transactions on Nanotechnology*, vol. 7, no. 3, pp. 338–343, 2008.

[36] S. Donthu, Z. Pan, B. Myers, G. Shekhawat, N. Wu, and V. Dravid, "Facile scheme for fabricating solid-state nanostructures using e-beam lithography and solution precursors," *Nano Letters*, vol. 5, no. 9, pp. 1710–1715, 2005.

[37] S. Donthu, T. Sun, and V. Dravid, "Fabrication and structural evaluation of beaded inorganic nanostructures using soft-electron-beam lithography," *Advanced Materials*, vol. 19, no. 1, pp. 125–128, 2007.

[38] R. Agrawal, B. Peng, E. Gdoutos, and H. Espinosa, "Elasticity size effects in ZnO nanowires- a combined experimental-computational approach," *Nano letters*, vol. 8, no. 11, pp. 3668–3674, 2008.

[39] K. Lee, D. Abraham, F. Secord, and L. Landstein, "Submicron Si trench profiling with an electron-beam fabricated atomic force microscope tip," *Journal of Vacuum Science & Technology B: Microelectronics and Nanometer Structures*, vol. 9, no. 6, pp. 3562–3568, 1991.

[40] P. Bøggild, T. Hansen, O. Kuhn, F. Grey, T. Junno, and L. Montelius, "Scanning nanoscale multiprobes for conductivity measurements," *Review of Scientific Instruments*, vol. 71, p. 2781, 2000.

[41] T. Ooi, K. Matsumoto, M. Nakao, M. Otsubo, S. Shirakata, S. Tanaka, and Y. Hatamura, "3D nano wire-frame for handling and observing a single DNA

fiber," *The Thirteenth Annual International Conference on Micro Electro Mechanical Systems*, pp. 580–583, 2000.

[42] S. Matsui, "Three-dimensional nanostructure fabrication by focused ion beam chemical vapor deposition," *Springer Handbook of Nanotechnology*, pp. 211–229, 2010.

[43] N. Arellano, E. Quevy, J. Provine, R. Maboudian, and R. Howe, "Silicon nanowire coupled micro-resonators," *IEEE 21st International Conference on Micro Electro Mechanical Systems*, pp. 721–724, 2008.

[44] Z. Shan, R. Mishra, S. Asif, O. Warren, and A. Minor, "Mechanical annealing and source-limited deformation in submicrometre-diameter Ni crystals," *Nature Materials*, vol. 7, no. 2, pp. 115–119, 2007.

[45] L. Giannuzzi and F. Stevie, "A review of focused ion beam milling techniques for TEM specimen preparation," *Micron*, vol. 30, no. 3, pp. 197–204, 1999.

[46] S. Reyntjens and R. Puers, "A review of focused ion beam applications in microsystem technology," *Journal of Micromechanics and Microengineering*, vol. 11, p. 287, 2001.

[47] T. Ishii, H. Nozawa, T. Tamamura, and A. Ozawa, "C_{60}-incorporated nanocomposite resist system for practical nanometer pattern fabrication," *Journal of Vacuum Science & Technology B: Microelectronics and Nanometer Structures*, vol. 15, no. 6, pp. 2570–2574, 1997.

[48] Y. Hu, H. Wu, K. Gonsalves, and L. Merhari, "Nanocomposite resists for electron beam nanolithography," *Microelectronic Engineering*, vol. 56, no. 3-4, pp. 289–294, 2001.

[49] N. Romyen, S. Thongyai, and P. Praserthdam, "Alignment of carbon nanotubes in polyimide under electric and magnetic fields," *Journal of Applied Polymer Science*, vol. 123, no. 6, pp. 3470–3475, 2012.

[50] Q. Tang, Y. Chan, N. Wong, and R. Cheung, "Surfactant-assisted processing of polyimide/multiwall carbon nanotube nanocomposites for microelectronics applications," *Polymer International*, vol. 59, no. 9, pp. 1240–1245, 2010.

[51] Z. Ounaies, C. Park, H. J., and L. P., "Evidence of piezolelectricity in SWNT-polyimide and SWNT-PZT-polyimide composites," *Journal of Thermoplastic Composite Materials*, vol. 21, pp. 393 – 409, 2008.

[52] P. Lillehei, J.-W. Kim, L. Gibbons, and C. Park, "A quantitative assessment of carbon nanotube dispersion in polymer matrices," *Nanotechnology*, vol. 20, no. 325708, p. 7, 2009.

[53] Y. Lin, K. Zhou, B.and Fernando, P. Liu, L. Allard, and Y.-P. Sun, "Polymeric carbon nanocomposites from carbon nanotubes functionalized with matrix polymer," *Macromolecules*, vol. 36, no. 19, pp. 7199–7204, 2003. cited By (since 1996) 256.

[54] M. Paiva, B. Zhou, K. Fernando, Y. Lin, J. Kennedy, and Y.-P. Sun, "Mechanical and morphological characterization of polymer-carbon nanocomposites from functionalized carbon nanotubes," *Carbon*, vol. 42, no. 14, pp. 2849–2854, 2004. cited By (since 1996) 117.

[55] A. Garg and S. Sinnott, "Effect of chemical functionalization on the mechanical properties of carbon nanotubes," *Chemical Physics Letters*, vol. 295, no. 4, pp. 273–278, 1998.

[56] G. Odegard, T. Gates, K. Wise, C. Park, and E. Siochi, "Constitutive modelling of nanotube reinforced polymer composites," *Composites Science and Technology*, vol. 63, pp. 1671 – 1687, 2003.

[57] P. Renaud, S. Metz, S. Jiguet, and A. Bertsch, "Composite photopolymer microstructures: From planar to 3D devices," *TRANSDUCERS, 12th International Conference on Solid-State Sensors, Actuators and Microsystems, 2003*, vol. 2, pp. 991–994, 2003.

[58] S. Jiguet, M. Judelewicz, S. Mischler, A. Bertch, and P. Renaud, "Effect of filler behavior on nanocomposite SU8 photoresist for moving micro-parts," *Microelectronic Engineering*, vol. 83, no. 4-9, pp. 1273–1276, 2006.

[59] S. Jiguet, A. Bertsch, H. Hofmann, and P. Renaud, "Conductive SU8 photoresist for microfabrication," *Advanced Functional Materials*, vol. 15, no. 9, pp. 1511–1516, 2005.

[60] S. Jiguet, A. Bertsch, M. Judelewicz, H. Hofmann, and P. Renaud, "SU-8 nanocomposite photoresist with low stress properties for microfabrication applications," *Microelectronic Engineering*, vol. 83, no. 10, pp. 1966–1970, 2006.

[61] A. Zhang, S. He, K. Kim, Y. Yoon, R. Burzynski, M. Samoc, and P. Prasad, "Fabrication of submicron structures in nanoparticle/polymer composite by

holographic lithography and reactive ion etching," *Applied Physics Letters*, vol. 93, p. 203509, 2008.

[62] A. Voigt, M. Heinrich, C. Martin, A. Llobera, G. Gruetzner, and F. Pérez-Murano, "Improved properties of epoxy nanocomposites for specific applications in the field of MEMS/NEMS," *Microelectronic Engineering*, vol. 84, no. 5-8, pp. 1075–1079, 2007.

[63] V. Seena, A. Rajorya, P. Pant, S. Mukherji, and V. Rao, "Polymer microcantilever biochemical sensors with integrated polymer composites for electrical detection," *Solid State Sciences*, vol. 11, no. 9, pp. 1606–1611, 2009.

[64] V. Seena, A. Fernandes, P. Pant, S. Mukherji, and V. Ramgopal Rao, "Polymer nanocomposite nanomechanical cantilever sensors: Material characterization, device development and application in explosive vapour detection," *Nanotechnology*, vol. 22, p. 295501, 2011.

[65] S. Zhang, D. Sun, Y. Fu, and H. Du, "Recent advances of superhard nanocomposite coatings: A review," *Surface and Coatings Technology*, vol. 167, no. 2-3, pp. 113–119, 2003.

[66] J. Musil, P. Baroch, J. Vlcek, K. Nam, and J. Han, "Reactive magnetron sputtering of thin films: Present status and trends," *Thin Solid Films*, vol. 475, no. 1-2, pp. 208–218, 2005.

[67] G. Robert and I. Parkin, "Aerosol assisted chemical vapor deposition using nanoparticle precursors: A route to nanocomposite thin films," *Journal of the American Chemical Society*, vol. 128, no. 5, pp. 1587–1597, 2006.

[68] P. Jedrzejowski, J. Klemberg-Sapieha, and L. Martinu, "Relationship between the mechanical properties and the microstructure of nanocomposite $TiN/SiN_{1.3}$ coatings prepared by low temperature plasma enhanced chemical vapor deposition," *Thin Solid Films*, vol. 426, no. 1-2, pp. 150–159, 2003.

[69] A. Abramson, W. Kim, S. Huxtable, H. Yan, Y. Wu, A. Majumdar, C. Tien, and P. Yang, "Fabrication and characterization of a nanowire/polymer-based nanocomposite for a prototype thermoelectric device," *Journal of Microelectromechanical Systems*, vol. 13, no. 3, pp. 505–513, 2004.

[70] L. Jiang, S. Spearing, M. M.A., and J. N.M., "Formation and mechanical characterisation of SU8 composite films reinforced with horizontally aligned

and high volume fraction CNTs," *Composites Science and Technology*, vol. 71, no. 10, pp. 1301 – 1308, 2011.

[71] L. Pei, J. Abbott, K. Zufelt, A. Davis, M. Zappe, K. Decker, S. Liddiard, R. Vanfleet, M. Linford, and R. Davis, "Processing of thin carbon nanotube-polyimide composite membranes," *Nanoscience and Nanotechnology Letters*, vol. 3, no. 4, pp. 451–457, 2011.

[72] J. Celis, J. Roos, and C. Buelens, "A mathematical model for the electrolytic codeposition of particles with a metallic matrix," *Journal of the Electrochemical Society*, vol. 134, p. 1402, 1987.

[73] A. Möller and H. Hahn, "Synthesis and characterization of nanocrystalline Ni/ZrO_2 composite coatings," *Nanostructured Materials*, vol. 12, no. 1-4, pp. 259–262, 1999.

[74] J. Li, Y. Sun, X. Sun, and J. Qiao, "Mechanical and corrosion-resistance performance of electrodeposited titania-nickel nanocomposite coatings," *Surface and Coatings Technology*, vol. 192, no. 2-3, pp. 331–335, 2005.

[75] K. Teh, Y. Cheng, and L. Lin, "Nickel nano-composite film for MEMS applications," *TRANSDUCERS,12th International Conference on Solid-State Sensors, Actuators and Microsystems, 2003*, vol. 2, pp. 1534–1537, 2003.

[76] K. Teh, Y. Cheng, and L. Lin, "MEMS fabrication based on nickel-nanocomposite: Film deposition and characterization," *Journal of Micromechanics and Microengineering*, vol. 15, p. 2205, 2005.

[77] L. Tsai, G. Shen, Y. Cheng, and W. Hsu, "Power and reliability improvement of an electro-thermal microactuator using Ni-diamond nanocomposite," *54th Electronic Components and Technology Conference Proceedings*, vol. 1, pp. 472–476, 2004.

[78] L. Tsai, G. Shen, Y. Cheng, and W. Hsu, "Performance improvement of an electrothermal microactuator fabricated using Ni-diamond nanocomposite," *Journal of Microelectromechanical Systems*, vol. 15, no. 1, pp. 149–158, 2006.

[79] G. Shen, Y. Cheng, and L. Tsai, "Synthesis and characterization of Ni-P-CNT's nanocomposite film for MEMS applications," *IEEE Transactions onNanotechnology*, vol. 4, no. 5, pp. 539–547, 2005.

[80] L. Tsai, Y. Cheng, W. Hsu, and W. Fang, "Ni-carbon nanotubes nanocomposite for robust microelectromechanical systems fabrication," *Journal of Vacuum Science & Technology B: Microelectronics and Nanometer Structures*, vol. 24, no. 1, pp. 205–210, 2006.

[81] A. Heilmann, *Polymer Films with Embedded Metal Nanoparticles*, vol. 52. Springer Verlag, 2003.

[82] L. Hench and J. West, "The sol-gel process," *Chemical Reviews*, vol. 90, no. 1, pp. 33–72, 1990.

[83] E. Traversa, M. Di Vona, P. Nunziante, S. Licoccia, T. Sasaki, and N. Koshizaki, "Sol-gel preparation and characterization of $Ag - TiO_2$ nanocomposite thin films," *Journal of Sol-Gel Science and Technology*, vol. 19, no. 1, pp. 733–736, 2000.

[84] J. Yoon, T. Sasaki, N. Koshizaki, and E. Traversa, "Preparation and characterization of M/TiO_2 (M= Ag, Au, Pt) nanocomposite thin films," *Scripta Materialia*, vol. 44, no. 8-9, pp. 1865–1868, 2001.

[85] H. Schmidt, G. Jonschker, S. Goedicke, and M. Mennig, "The sol-gel process as a basic technology for nanoparticle-dispersed inorganic-organic composites," *Journal of Sol-Gel Science and Technology*, vol. 19, no. 1, pp. 39–51, 2000.

[86] W. Fritzsche, H. Porwol, A. Wiegand, S. Bornmann, and J. Köhler, "In-situ formation of Ag-containing nanoparticles in thin polymer films," *Nanostructured Materials*, vol. 10, no. 1, pp. 89–97, 1998.

[87] R. Abargues, J. Marqués-Hueso, J. Canet-Ferrer, E. Pedrueza, J. Valdés, E. Jimenez, and J. Martínez-Pastor, "High-resolution electron-beam patternable nanocomposite containing metal nanoparticles for plasmonics," *Nanotechnology*, vol. 19, p. 355308, 2008.

[88] G. Decher and J. Schlenoff, *Multilayer Thin Films*. Wiley Online Library, 2003.

[89] C. Jiang, S. Markutsya, Y. Pikus, and V. Tsukruk, "Freely suspended nanocomposite membranes as highly sensitive sensors," *Nature Materials*, vol. 3, no. 10, pp. 721–728, 2004.

[90] N. Pham, T. Scholtes, R. Klerk, B. Wieder, P. Sarro, and J. Burghartz, "Direct spray coating of photoresist for MEMS applications," *Proceedings of SPIE*, vol. 4557, p. 312, 2001.

[91] L. Yu, Y. Lee, F. Tay, and C. Iliescu, "Spray coating of photoresist for 3d microstructures with different geometries," *Journal of Physics: Conference Series*, vol. 34, p. 937, 2006.

[92] N. Pham, J. Burghartz, and P. Sarro, "Spray coating of photoresist for pattern transfer on high topography surfaces," *Journal of Micromechanics and Microengineering*, vol. 15, p. 691, 2005.

[93] J. Linden, C. Thanner, B. Schaaf, S. Wolff, L. B., and E. Oesterschulze, "Spray coating of PMMA for pattern transfer via electron beam lithography on surfaces with high topography," *Microelectronic Engineering*, vol. 88, no. 8, pp. 2030–2032, 2011.

[94] A. Tseng, K. Chen, C. Chen, and K. Ma, "Electron beam lithography in nanoscale fabrication: Recent development," *IEEE Transactions on Electronics Packaging Manufacturing*, vol. 26, no. 2, pp. 141–149, 2003.

[95] G. Brewer and J. Ballantyne, *Electron-beam technology in microelectronic fabrication*. Academic press New York, 1980.

[96] D. Doppalapudi, R. Mlcak, J. LeClair, P. Gwynne, J. Bridgham, S. Purchase, M. Skelton, G. Schultz, and H. Tuller, "MEMS microresonators for high temperature sensor applications," *Materials Research Society Symposium Proceedings*, vol. 1222, pp. 1222–DD01–02, 2009.

[97] A. Labuda, J. Bates, and P. Grütter, "The noise of coated cantilevers," *Nanotechnology*, vol. 23, p. 025503, 2012.

[98] G. Sosale, K. Das, L. Fréchette, and S. Vengallatore, "Controlling damping and quality factors of silicon microcantilevers by selective metallization," *Journal of Micromechanics and Microengineering*, vol. 21, p. 105010, 2011.

[99] B. Ashrafi, P. Hubert, and S. Vengallatore, "Carbon nanotube-reinforced composites as structural materials for microactuators in microelectromechanical systems," *Nanotechnology*, vol. 17, pp. 4895–4903, 2006.

[100] D. Zhang and T. Cui, "Tunable mechanical properties of self-assembled SWNT/polymer nanocomposite films for MEMS," in *IEEE 24th International Conference on Micro Electro Mechanical Systems (MEMS), 2011*, pp. 497 –500, jan. 2011.

[101] B. Ashrafi, *Theoretical and Experimental Investigations of the Elastic Properties of Carbon Nanotube - Reinforced Polymer Thin Films*. PhD thesis, McGill University, 2008.

[102] P. Hubert, B. Ashrafi, K. Adhikari, J. Meredith, S. Vengallatore, J. Guan, and B. Simard, "Synthesis and characterization of carbon nanotube-reinforced epoxy: Correlation between viscosity and elastic modulus," *Composites Science and Technology*, vol. 69, pp. 2274 – 2280, 2009.

[103] C. Park, Z. Ounaies, K. Watson, R. Crooks, J. Connell, S. Lowther, E. Siochi, J. Harrison, and T. St. Clair, "Dispersion of single wall carbon nanotubes by in situ polymerization under sonication," *Chemical Physics Letters*, vol. 364, pp. 303 – 308, 2002.

[104] T. Clyne and P. Withers, *An Introduction to Metal Matrix Composites*. Cambridge University Press, 1995.

[105] J. Eshelby, "The determination of the elastic field of an ellipsoidal inclusion, and related problems," *Proceedings of the Royal Society of London*, vol. 241, pp. 376 – 396, 1957.

[106] T. Mori and K. Tanaka, "Average stress in matrix and average elastic energy of materials with misfitting inclusions," *Acta Metallurgica*, vol. 21, pp. 571–574, 1973.

[107] Y. Benveniste, "A new approach to the application of Mori-Tanaka's theory in composite materials," *Mechanics of Materials*, vol. 69, pp. 147 – 157, 1987.

[108] C. Chen and C. Cheng, "Effectieve elastic moduli of misoriented short-fiber composites," *Journal of Solids and Structures*, vol. 33, pp. 2519 – 2539, 1996.

[109] M. Mura, *Micromechanics of Defects in Solids*. Martinus Nijhoff Publishers, 1987.

[110] L. Shen and J. Li, "Transversely isotropic elastic properties of single-walled carbon nanotubes," *Physical Review B*, vol. 69, p. 045414, 2004.

[111] B. Ashrafi and P. Hubert, "Modeling the elastic properties of carbon nanotube array/polymer composites," *Composites Science & Technology*, vol. 66, no. 3-4, pp. 387–396, 2006.

[112] S. Timoshenko and S. Woinowsky-Krieger, *Theory of Plates and Shells*. McGraw-Hill, 1959.

[113] O. Scott, M. Begley, U. Komaragiri, and T. Mackin, "Indentation of freestanding circular elastomer films using spherical indenters," *Acta Materialia*, vol. 52, no. 16, pp. 4877 – 4885, 2004.

[114] K. Johnson, *Contact Mechanics*. Cambridge University Press, 1987.

[115] V. Srikar and S. Spearing, "Materials selection in micromechanical design: An application of the Ashby approach," *Journal of Microelectromechanical Systems*, vol. 12, no. 1, pp. 3–10, 2003.

[116] M. Ashby, *Materials Selection in Mechanical Design*. Butterworth-Heinemann, 2005.

[117] U. Komaragiri, M. Begley, and J. Simmonds, "The mechanical response of freestanding circular elastic films under point and contact loads," *Journal of Applied Mechanics*, vol. 72, no. 2, pp. 203 – 212, 2005.

[118] M. Begley and T. Mackin, "Spherical indentation of freestanding circular thin films in the membrane regime," *Journal of the Mechanics and Physics of Solids*, vol. 52, no. 9, pp. 2005 – 2023, 2004.

[119] P. Lillehei, C. Park, J.-W. Kim, L. Gibbons, K. Wise, and E. Siochi, "Quantification of SWNT dispersion in polymer composites." 3rd NASA-NIST workshop on nanotube measurement, gaithersburg, MD, September 2007.

[120] M. Daener, R. De Fouw, B. Hamers, P. Janssen, K. Schouteden, and M. Veld, "The wondrous world of carbon nanotubes." Eindhoven University of Technology, 2003.

[121] M. Li, H. Tang, and M. Roukes, "Ultra-sensitive NEMS-based cantilevers for sensing, scanned probe and very high-frequency applications," *Nature Nanotechnology*, vol. 2, no. 2, pp. 114–120, 2007.

[122] P. Poncharal, Z. Wang, D. Ugarte, and W. de Heer, "Electrostatic deflections and electromechanical resonances of carbon nanotubes," *Science*, vol. 283, no. 5407, p. 1513, 1999.

[123] A. Suryavanshi, M. Yu, J. Wen, C. Tang, and Y. Bando, "Elastic modulus and resonance behavior of boron nitride nanotubes," *Applied Physics Letters*, vol. 84, p. 2527, 2004.

[124] X. Bai, P. Gao, Z. Wang, and E. Wang, "Dual-mode mechanical resonance of individual ZnO nanobelts," *Applied Physics Letters*, vol. 82, p. 4806, 2003.

[125] S. Perisanu, P. Vincent, A. Ayari, M. Choueib, S. Purcell, M. Bechelany, and D. Cornu, "High Q factor for mechanical resonances of batch-fabricated SiC nanowires," *Applied physics letters*, vol. 90, p. 043113, 2007.

[126] M. Belov, N. Quitoriano, S. Sharma, W. Hiebert, T. Kamins, and S. Evoy, "Mechanical resonance of clamped silicon nanowires measured by optical interferometry," *Journal of Applied Physics*, vol. 103, p. 074304, 2008.

[127] C. Guthy, R. Das, B. Drobot, and S. Evoy, "Resonant characteristics of ultra-narrow SiCN nanomechanical resonators," *Journal of Applied Physics*, vol. 108, p. 014306, 2010.

[128] K. Yum, Z. Wang, A. Suryavanshi, and M. Yu, "Experimental measurement and model analysis of damping effect in nanoscale mechanical beam resonators in air," *Journal of Applied Physics*, vol. 96, p. 3933, 2004.

[129] A. Pandey and R. Pratap, "Effect of flexural modes on squeeze film damping in MEMS cantilever resonators," *Journal of Micromechanics and Microengineering*, vol. 17, p. 2475, 2007.

[130] S. Rinaldi, S. Prabhakar, S. Vengallatore, and M. Païdoussis, "Dynamics of microscale pipes containing internal fluid flow: Damping, frequency shift, and stability," *Journal of Sound and Vibration*, vol. 329, no. 8, pp. 1081–1088, 2010.

[131] K. Yasumura, T. Stowe, E. Chow, T. Pfafman, T. Kenny, B. Stipe, and D. Rugar, "Quality factors in micron-and submicron-thick cantilevers," *Journal of Microelectromechanical Systems*, vol. 9, no. 1, pp. 117–125, 2000.

[132] H. Hosaka, K. Itao, and S. Kuroda, "Damping characteristics of beam-shaped micro-oscillators," *Sensors and Actuators A: Physical*, vol. 49, no. 1-2, pp. 87–95, 1995.

[133] Z. Hao, A. Erbil, and F. Ayazi, "An analytical model for support loss in micromachined beam resonators with in-plane flexural vibrations," *Sensors and Actuators A: Physical*, vol. 109, no. 1-2, pp. 156–164, 2003.

[134] J. Judge, D. Photiadis, J. Vignola, B. Houston, and J. Jarzynski, "Attachment loss of micromechanical and nanomechanical resonators in the limits of thick and thin support structures," *Journal of Applied Physics*, vol. 101, p. 013521, 2007.

[135] J. Baur and A. Kulik, "Optimal sample shape for internal friction measurements using a dual cantilevered beam," *Journal of applied physics*, vol. 58, no. 4, pp. 1489–1492, 1985.

[136] R. Schwarz and L. Funk, "Internal-friction study of solute segregation to dislocations," *Acta Metallurgica*, vol. 31, no. 2, pp. 299–315, 1983.

[137] S. Yang, R. Gibson, G. Crosbie, and R. Allor, "Measurement of dynamic mechanical properties of advanced ceramics and ceramic matrix composites at temperatures above 1000 °C," *Experimental Techniques*, vol. 20, no. 3, pp. 20–23, 1996.

[138] S. Reid, G. Cagnoli, D. Crooks, J. Hough, P. Murray, S. Rowan, M. Fejer, R. Route, and S. Zappe, "Mechanical dissipation in silicon flexures," *Physics Letters A*, vol. 351, no. 4-5, pp. 205–211, 2006.

[139] A. Nowick and B. Berry, *Anelastic Relaxation in Crystalline Solids*, vol. 1. Academic Press, 1972.

[140] M. Blanter and M. Blanter, *Internal Friction in Metallic Materials: A Handbook*, vol. 90. Springer Verlag, 2007.

[141] C. Zener, "Internal friction in solids," *Proceedings of the Physical Society*, vol. 52, p. 152, 1940.

[142] V. Kinra and K. Milligan, "A second-law analysis of thermoelastic damping," *Journal of Applied Mechanics*, vol. 61, p. 71, 1994.

[143] R. Lifshitz and M. Roukes, "Thermoelastic damping in micro-and nanomechanical systems," *Physical Review B*, vol. 61, no. 8, p. 5600, 2000.

[144] S. Prabhakar and S. Vengallatore, "Theory of thermoelastic damping in micromechanical resonators with two-dimensional heat conduction," *Microelectromechanical Systems, Journal of*, vol. 17, no. 2, pp. 494–502, 2008.

[145] G. Weiss and D. Smith, "Measurement of internal friction in thin films," *Review of Scientific Instruments*, vol. 34, p. 522, 1963.

[146] B. Berry and W. Pritchet, "Vibrating reed internal friction apparatus for films and foils," *IBM Journal of Research and Development*, vol. 19, no. 4, pp. 334–343, 1975.

[147] B. Berry and W. Pritchet, "Defect studies of thin layers by the vibrating-reed technique," *Le Journal de Physique Colloques*, vol. 42, no. C5, pp. 5–5, 1981.

[148] B. Berry and W. Pritchet, "Extended capabilities of a vibrating-reed internal friction apparatus," *Review of Scientific Instruments*, vol. 54, no. 2, pp. 254–256, 1983.

[149] R. Lacombe and B. Kellner, "Thermal-mechanical properties of a monomolecular film detected by a vibrating reed," *Nature*, vol. 289, pp. 661–662, 1981.

[150] H. Bohn and C. Su, "Characterization of thin films by internal friction measurements," in *Materials Research Society Proceedings*, vol. 239, Elsevier, December 1991.

[151] M. Prieler, H. Bohn, W. Schilling, and H. Trinkaus, "Grain boundary sliding in thin substrate-bonded Al films," *Journal of Alloys and Compounds*, vol. 211, pp. 424–427, 1994.

[152] D. Choi, H. Kim, and W. Nix, "Anelasticity and damping of thin aluminum films on silicon substrates," *Journal of Microelectromechanical Systems*, vol. 13, no. 2, pp. 230–237, 2004.

[153] D. Choi and W. Nix, "Anelastic behavior of copper thin films on silicon substrates: Damping associated with dislocations," *Acta materialia*, vol. 54, no. 3, pp. 679–687, 2006.

[154] G. Sosale, *A Microcantilever Platform for Measuring Internal Friction in Thin Films Using Thermoelastic Damping for Calibration*. PhD thesis, McGill University, 2011.

[155] S. Prabhakar and S. Vengallatore, "Thermoelastic damping in bilayered micromechanical beam resonators," *Journal of Micromechanics and Microengineering*, vol. 17, p. 532, 2007.

[156] S. Rao, *Mechanical Vibrations*. Addison-Wesley, 1995.

[157] G. Sosale, D. Almecija, K. Das, and S. Vengallatore, "Mechanical spectroscopy of nanocrystalline aluminum films: Effects of frequency and grain size on internal friction." submitted to Nanotechnology.

[158] C. E. Baddour, *Direct Growth of Carbon Nanotubes on Metal Surfaces without External Catalyst and Nanocomposite Production*. PhD thesis, McGill University, 2010.

[159] R. Janes, M. Aldissi, and R. Kaner, "Controlling surface area of titanium nitride using metathesis reactions," *Chemistry of Materials*, pp. 4431–4435, 2003.

[160] H. Pierson, *Handbook of Refractory Carbides and Nitrides: Properties, Characteristics, Processing, and Applications*. Noyes Publications, 1996.

[161] J. F. Shackelford and W. Alexander, *CRC Materials Science and Engineering Handbook, 3rd edition*. CRC Press, 2001.

[162] C. Baddour, F. Fadlallah, D. Nasuhoglu, R. Mitra, L. Vandsburger, and J. Meunier, "A simple thermal CVD method for carbon nanotube synthesis on stainless steel 304 without the addition of an external catalyst," *Carbon*, vol. 47, no. 1, pp. 313–318, 2009.

[163] W. Oliver and G. Pharr, "Improved technique for determining hardness and elastic modulus using load and displacement sensing indentation experiments," *Journal of Materials Research*, vol. 7, no. 6, pp. 1564–1583, 1992.

[164] W. Oliver and G. Pharr, "Measurement of hardness and elastic modulus by instrumented indentation: Advances in understanding and refinements to methodology," *Journal of Materials Research*, vol. 19, no. 01, pp. 3–20, 2004.

[165] I. Sneddon, "The relation between load and penetration in the axisymmetric boussinesq problem for a punch of arbitrary profile," *International Journal of Engineering Science*, vol. 3, no. 1, pp. 47–57, 1965.

[166] W. Yan and C. Pun, "Spherical indentation of metallic foams," *Materials Science and Engineering: A*, vol. 527, no. 13-14, pp. 3166–3175, 2010.

[167] S. Iijima, "Helical microtubules of graphitic carbon," *Nature*, vol. 354, no. 6348, pp. 56–58, 1991.

[168] J. Salvetat, J. Bonard, N. Thomson, A. Kulik, L. Forro, W. Benoit, and L. Zuppiroli, "Mechanical properties of carbon nanotubes," *Applied Physics A: Materials Science and Processing*, vol. 69, no. 3, pp. 255–260, 1999.

[169] R. Saito, G. Dresselhaus, M. Dresselhaus, *et al.*, *Physical properties of carbon nanotubes*, vol. 3. Imperial College Press London, 1998.

[170] H. Qi, K. Teo, K. Lau, M. Boyce, W. Milne, J. Robertson, and K. Gleason, "Determination of mechanical properties of carbon nanotubes and vertically aligned carbon nanotube forests using nanoindentation," *Journal of the Mechanics and Physics of Solids*, vol. 51, no. 11-12, pp. 2213–2237, 2003.

[171] S. Mesarovic, C. McCarter, D. Bahr, H. Radhakrishnan, R. Richards, C. Richards, D. McClain, and J. Jiao, "Mechanical behavior of a carbon nanotube turf," *Scripta Materialia*, vol. 56, no. 2, pp. 157–160, 2007.

[172] C. McCarter, R. Richards, S. Mesarovic, C. Richards, D. Bahr, D. McClain, and J. Jiao, "Mechanical compliance of photolithographically defined vertically aligned carbon nanotube turf," *Journal of Materials Science*, vol. 41, no. 23, pp. 7872–7878, 2006.

[173] A. Zbib, S. Mesarovic, D. Bahr, E. Lilleodden, J. Jiao, and D. McClain, "Indentation response of nanostructured turfs," *Materials Research Society Symposium Proceedings*, vol. 1049, pp. 15–20, 2008.

[174] A. Zbib, S. Mesarovic, E. Lilleodden, D. McClain, J. Jiao, and D. Bahr, "The coordinated buckling of carbon nanotube turfs under uniform compression," *Nanotechnology*, vol. 19, p. 175704, 2008.

[175] M. Liao and Y. Koide, "CMOS cantilever sensor systems: Atomic force microscopy and gas sensing applications," *Critical Reviews in Solid State and Materials Sciences*, vol. 36, no. 2, pp. 66–101, 2011.

[176] J. McBride, E. Yunus, and S. Spearing, "Gold coated multi-walled carbon nanotube surfaces as low force electrical contacts for MEMS devices: Part 1," *Proceedings of the 55th IEEE Holm Conference on Electrical Contacts*, pp. 281–287, 2009.

[177] J. McBride, "The wear processes of gold coated multi-walled carbon nanotube surfaces used as electrical contacts for micro-electro-mechanical switching," *Nanoscience and Nanotechnology Letters*, vol. 2, no. 4, pp. 357–361, 2010.